Scuola Internazionale Superiore di Studi Avanzati - Trieste

Condensed Matter Theory Sector

Electronic Properties of Gold Nanoclusters from GW Calculations

Thesis submitted for the degree of Doctor Philosophiæ
Academic Year 2011/2012

CANDIDATE
Jiawei Xian

SUPERVISORS
Prof. Stefano Baroni
Prof. Paolo Umari

December 2012

SISSA - Via Bonomea 265 - 34136 TRIESTE - ITALY

Contents

Introduction

Speaking of gold, what comes to one's mind first is that it's a shiny, yellow, soft, precious and chemically inert metal. Known as the first metal discovered by human beings, gold historically has been considered valuable by many cultures. Throughout the history of human civilization, gold metal has been widely used in many areas because of its unique properties [1]. As gold is shiny, tarnish free and precious, it has high artistic value and has been used in jewelry and decoration since ancient times. Gold is not only of aesthetic value, but has also been found of practical value for ages in monetary exchange and dentistry. Besides, colloidal gold nanoparticles have a long history of applications in glass staining and medicine [1, 2]. Nowadays, since gold metal is highly conductive and ductile, and resistant to corrosion and oxidization, it is also used in the industrial area of electronics [3].

Being regarded as the noblest of all the metals [4], gold was long considered not as important as the other group 11 elements, i.e., Cu and Ag, in areas such as catalysis and surface chemistry. However, despite that gold is a typical noble metal in the bulk form, it can be catalytically active in the cluster form. In 1987, Haruta et al. found that when supported on base metal oxides such as $\alpha - \mathrm{Fe_2O_3}$, $\mathrm{Co_2O_4}$ and NiO, gold nanoclusters can catalyze CO oxidization effectively at a temperature as low as 200 K [5]. This discovery of the unexpected novel catalytic property of gold nanoclusters has triggered a surge of interest in the theoretical and experimental investigations of the physical and chemical properties of gold nanoclusters in the past two decades. Today, a lot of research has been concentrated on the potential applications of gold nanoclusters in nanotechnology, catalysis, biology and medicine [6–17].

According to cluster science, metal nanoclusters, or metal clusters in short, refer to particles of metal atoms with a size ranging from as small as two atoms, to as large as a few hundreds of thousands of atoms [18]. Just like other metal clusters, the properties of small gold clusters such as geometry, electronic structure and chemical reactivity strongly depend on the cluster size and significantly differ from those of bulk gold. For example, the ionization potentials of small neutral gold clusters are strongly dependent on the cluster size and are much higher than the work function of bulk gold [19]. Small gold clusters are quite different from bulk gold because they have a large surface-to-volume ratio [20]. The lower coordination numbers of surface atoms compared with those

of body atoms put the surface atoms under different physical and chemical environments and lead them to possess different properties. As a matter of fact, in the cases of small gold clusters, even a unit change in the number of atoms or electrons could drastically change the physical and chemical properties.

Gold clusters have some interesting properties not found in other metal clusters. One of them is that small gold clusters favor two-dimensional structures at relatively large cluster sizes. By comparing the calculated collision cross sections from the density-functional theory (DFT) and those measured from ion mobility experiments, the cluster size up to which planar structures are favored for cationic or anionic gold clusters has been determined. Gilb et al. found that cationic gold clusters $\mathrm{Au_N}$ are planar up to $\mathrm{N} = 7$ [21], while Furche et al. found that anionic gold clusters $\mathrm{Au_N}$ can have planar structures up to $\mathrm{N} = 12$ [22]. Unfortunately, the cluster size up to which planar structures are favored for neutral gold clusters hasn't been determined yet [23]. However, a large amount of theoretical research exists and it is generally believed that neutral gold clusters $\mathrm{Au_N}$ are planar up to $\mathrm{N} = 11 - 13$ [24–31]. At variance with gold clusters, most of other metal clusters are planar up to only a size of $4 - 6$ atoms, depending on the charge state. An extension to the tendency of very small gold clusters to display planar structures is that larger gold clusters can have interesting quasi two-dimensional structures. A hollow tetrahedral structure was reported by Li et al. as the ground-state structure for the neutral and anionic $\mathrm{Au_{20}}$ clusters [32], and this finding was confirmed by combinations of theoretical and experimental studies [23, 32]. Based on DFT calculations, Johansson et al. and Gu et al. discovered a highly stable cagelike icosahedral structure for the neutral $\mathrm{Au_{32}}$ cluster which has the same symmetry as $\mathrm{C_{60}}$ fullerene and can incorporate up to 3 gold atoms inside its inner shell [33, 34]. Interesting cagelike structures have also been found for some anionic gold clusters [35, 36].

The tendency of small gold clusters to display planar structures has been attributed to the strong relativistic effects in gold [37, 38]. As a heavy element, gold has unusually large relativistic effects larger than any of its neighboring elements, including the other coinage metals Cu and Ag. The strong relativistic effects in gold lead to an orbital expansion and an energy increase of the 5d electrons, and an orbital contraction and an energy decrease of the 6s electrons. As a result, on the one hand, the energies of the 5d and 6s electrons are brought closer so that there is strong s-d hybridization in gold; on the other hand, in gold clusters the overlap between the 5d electrons of neighboring atoms is enhanced, resulting in a high directionality in bonding.

Even though the ground-state properties of gold clusters, especially the relative stabilities of different structures at different cluster sizes, have been extensively investigated using DFT [24–31, 35, 36], the excitation properties are relatively unexplored at the theoretical level. In the study of the excitation properties of these systems, it is particularly important to have a thorough understanding of the relation between the structure and the electron dynamics. This would be instrumental to the identification of spectroscopic fingerprints of specific structural features, to be used for charac-

terization purposes. However, DFT [39, 40] is not apt to this aim and such an understanding is still lacking. Hence, more sophisticated techniques based on many-body perturbation theory (MBPT) [41–43] are called for. The GW method [44] based on MBPT is deemed to be the state of the art for the simulation of the photoemission (quasiparticle) spectroscopy in molecular and extended systems, and is thus an ideal tool for the study of some of the excitation properties of gold clusters.

The main body of this thesis is devoted to the investigation of the quasiparticle spectra of neutral gold clusters by using the GW method. We focus on the study of small clusters $\mathrm{Au_N}$ ($\mathrm{N} = 1 - 8$) (including the Au atom), as well as two larger quasi two-dimensional clusters, the tetrahedral $\mathrm{Au_{20}}$ cluster and the cagelike $\mathrm{Au_{32}}$ cluster. The Quantum Espresso density-functional package [45] is employed to perform electronic structure calculations. In particular, the GWL module [46] of Quantum Espresso is used for the GW parts of the calculations. Our implementation of the GW method has incorporated recently introduced algorithms [47, 48] which address the main computational difficulties involved in traditional GW calculations and can significantly enhance the scope of GW calculations.

Two specific aspects are considered concerning the GW calculations of gold clusters: the Au semicore 5s and 5p states and the open-shell character of some symmetric molecular structures. We find that an explicit inclusion of the Au semicore 5s and 5p states in the valence manifold is essential to achieve a satisfactory accuracy in the calculated quasiparticle spectra. Based on this observation, we use a recently developed simplified approach [49] to account for the effects of the Au semicore 5s and 5p states without including them fully in the GW calculations. By doing so, a significant speed up of the calculations is obtained, while the accuracy of the computed spectra is not compromised. This simplified approach makes the GW method fit to the study of larger gold clusters, such as $\mathrm{Au_{20}}$ and $\mathrm{Au_{32}}$, which can not be tackled easily using more conventional approaches. The electronic structure of open-shell molecules is hardly addressed in traditional GW calculations. However, in the study of small clusters, one can frequently meet symmetric structures with open-shells. We show how the electronic excitation properties of open-shell molecules can be studied by making some compromise in the GW calculations of these molecules.

This thesis is organized as follows: In Chapter 1, we review the theoretical background relevant to the GW method. A general introduction is first given for DFT, which is the starting point for our GW calculations, then for MBPT, with emphasis on the GW approximation. In Chapter 2, our implementation of the GW method is explained in detail, and illustrated with a particular example of the application to the caffeine molecule. We present in the same chapter a few methodological details with specific relevance to our GW study of gold clusters, including the role of the Au semicore 5s and 5p states and the treatment of molecular open-shells. In Chapter 3, we report our results for the electronic properties of small neutral gold clusters $\mathrm{Au_N}$ ($\mathrm{N} = 1 - 8$), as well as of two larger neutral gold clusters, the tetrahedral $\mathrm{Au_{20}}$ cluster and the cagelike $\mathrm{Au_{32}}$ cluster. Finally, we conclude the work of this thesis and make an outlook for future research.

Chapter 1

Theoretical Background of Electronic Structure

In this chapter, we review the theoretical background underlying the work of this thesis. We first briefly describe the basics of the density-functional theory, the theory on which our implementation of the GW method in this work is based. After that, we present a short introduction to many-body perturbation theory, with particular emphasis on the GW approximation.

Hartree atomic units, with $\hbar = \mathrm{m} = \mathrm{e} = 4\pi/\epsilon_0 = 1$, are used throughout this thesis, unless otherwise explicitly stated.

1.1 Density-Functional Theory

In this section, we briefly review the very basics of the density-functional theory. The subjects discussed cover the foundation of the density-functional theory in terms of the two Hohenberg-Kohn theorems, the Kohn-Sham formalism for the density-functional theory, approximations for the exchange-correlation functional, and the plane-wave pseudopotential approach for the practical implementation of the density-functional theory.

1.1.1 Hohenberg-Kohn Theorems

In the Born-Oppenheimer approximation [50], the non-relativistic many-body $\mathrm{Schrödinger}$ equation for a system of N interacting electrons in the external potential from fixed nuclei reads:

$$\hat{H}(\{\mathbf{r}\};\{\mathbf{R}\})\Psi_m(\{\mathbf{r}\};\{\mathbf{R}\}) = E_m(\{\mathbf{R}\})\Psi_m(\{\mathbf{r}\};\{\mathbf{R}\}) \tag{1.1}$$

where

$$\hat{H}(\{\mathbf{r}\};\{\mathbf{R}\}) = \hat{K}(\{\mathbf{r}\}) + \hat{W}(\{\mathbf{r}\}) + \hat{V}(\{\mathbf{r}\};\{\mathbf{R}\}) \tag{1.2}$$

and

$$\hat{K}(\{\mathbf{r}\}) = -\frac{1}{2}\sum_i \frac{\partial^2}{\partial \mathbf{r}_i^2}, \tag{1.3}$$

$$\hat{W}(\{\mathbf{r}\}) = \frac{1}{2}\sum_{i\neq j} v(\mathbf{r}_i, \mathbf{r}_j) = \frac{1}{2}\sum_{i\neq j} \frac{1}{|\mathbf{r}_i - \mathbf{r}_j|}, \tag{1.4}$$

$$\hat{V}(\{\mathbf{r}\};\{\mathbf{R}\}) = \sum_i V_{ext}(\mathbf{r}_i;\{\mathbf{R}\}) = -\sum_{i,I} \frac{Z_I}{|\mathbf{r}_i - \mathbf{R}_I|}, \tag{1.5}$$

$\mathbf{r}_\mathrm{i}$ and $\mathbf{R}_\mathrm{I}$ being the coordinate of the i-th electron and that of the I-th nucleus respectively, $\{\mathbf{r}\}$ and $\{\mathbf{R}\}$ being the set of the electronic coordinates and that of the nuclear coordinates respectively, and $\mathrm{Z_I}$ being the atomic number of the I-th nucleus. In the above equations, $\hat{\mathrm{H}}(\{\mathbf{r}\};\{\mathbf{R}\})$ is the many-body Hamiltonian for the electronic degrees of freedom at a fixed configuration $\{\mathbf{R}_\mathrm{I}\}$ of the nuclei; $\hat{\mathrm{K}}(\{\mathbf{r}\})$ describes the electronic kinetic energy; $\hat{\mathrm{W}}(\{\mathbf{r}\})$ gives the electron-electron Coulomb interaction potential; $\mathrm{V}(\{\mathbf{r}\};\{\mathbf{R}\})$ represents the electron-nucleus Coulomb interaction energy, $\mathrm{V_{ext}}(\mathbf{r}_\mathrm{i};\{\mathbf{R}\})$ being the corresponding one-electron external potential from the nuclei for the i-th electron; $\Psi_\mathrm{m}(\{\mathbf{r}\};\{\mathbf{R}\})$ is the many-body wavefunction that depends parametrically on $\{\mathbf{R}\}$, and $\mathrm{E_m}(\{\mathbf{R}\})$ is the corresponding eigenvalue. We put a hat on top of a quantity to indicate explicitly that the quantity is a quantum mechanical operator. Here and in the rest of the thesis, unless otherwise explicitly specified, we neglect the spin dependence of electrons in order to simplify the notation and the discussion. For simplicity, in the following we also omit to explicitly indicate the parametric dependence of quantities on the configuration $\{\mathbf{R}\}$ of the nuclei. A direct solution to the problem described by Eqs. (1.1)-(1.5) is almost impossible, due to the 3N electronic degrees of freedom involved.

The above many-body problem at the ground-state level can be efficiently replaced by an effective one-body problem with the help of the density functional theory (DFT) developed since the 1960's [39, 40], which is a powerful first principles method for the simulation of the electronic properties of many-particle systems. DFT is based on two basic theorems known as the Hohenberg-Kohn theorems, which were first proposed by Hohenberg and Kohn in 1964 [39], and were later presented in a more general formulation by Levy and Lieb [51, 52].

First Hohenberg-Kohn theorem. *For any system of interacting particles in an external potential $V_{ext}(\mathbf{r})$, the ground-state particle density $n_0(\mathbf{r})$ determines uniquely $V_{ext}(\mathbf{r})$, except for a constant.*

It follows from the first Hohenberg-Kohn theorem that the ground-state particle density $\mathrm{n_0}(\mathbf{r})$ determines uniquely the full many-body Hamiltonian $\hat{\mathrm{H}}$, except for a constant shift in the external potential $\mathrm{V_{ext}}(\mathbf{r})$. As a result, in principle all the ground-state and excited-state properties of the system can be calculated from $\mathrm{n_0}(\mathbf{r})$, and $\mathrm{n_0}(\mathbf{r})$ can be used as the basic variable in solving the many-body problem.

Second Hohenberg-Kohn theorem. *A universal functional $F[n(\cdot)]$ of the particle density $n(\mathbf{r})$ can be defined for any system of interacting particles in an external potential $\mathrm{V_{ext}}(\mathbf{r})$, such that the*

particle density $n(\mathbf{r})$ that minimizes globally the functional $E[n(\cdot)] = F[n(\cdot)] + \int d\mathbf{r} n(\mathbf{r}) V_{ext}(\mathbf{r})$ gives the exact ground-state energy $E_0[n_0(\cdot)]$ of the system, and is the exact ground-state particle density $n_0(\mathbf{r})$.

$\mathrm{F}[\mathrm{n}(\cdot)]$ is the so-called Hohenberg-Kohn functional, where we have used a dot to indicate the dummy dependence of the argument of the functional on the particle coordinate $\mathbf{r}$. The second Hohenberg-Kohn theorem provides a variational method for the exact determination of the ground-state energy and the ground-state particle density of a many-body system of interacting particles.

For a system of N interacting electrons moving in an external potential, the problem is now simplified by the two Hohenberg-Kohn theorems, such that instead of dealing with the many-body wavefunction $\Psi_{\mathrm{m}}(\{\mathbf{r}\})$ which contains 3N degrees of freedom, we now consider the electronic charge-density $\mathrm{n}(\mathbf{r})$ which has only 3 degrees of freedom. The application of DFT based on the two Hohenberg-Kohn theorems to solve the many-body problem of interacting electrons would be straightforward, if a good approximated form of the Hohenberg-Kohn functional $\mathrm{F}[\mathrm{n}(\cdot)]$ was known. Unfortunately, this is usually not the case.

1.1.2 Kohn-Sham Equations

It is the approach proposed by Kohn and Sham in 1965 that makes the practical application of DFT to the numerical simulation of real systems possible [40]. The central idea of Kohn and Sham is to replace the complicated many-body problem of interacting electrons with an equivalent auxiliary independent-electron problem that is much easier to solve. To achieve this goal, following Kohn and Sham, we separate the Hohenberg-Kohn functional $\mathrm{F}[\mathrm{n}(\cdot)]$ into three components:

$$F[n(\cdot)] = T_0[n(\cdot)] + E_H[n(\cdot)] + E_{xc}[n(\cdot)], \tag{1.6}$$

where $\mathrm{T}_0[\mathrm{n}(\cdot)]$ is the kinetic energy of a system of non-interacting electrons in its ground state with the electronic charge-density $\mathrm{n}(\mathbf{r})$[1], the so-called Hartree energy $\mathrm{E}_{\mathrm{H}}[\mathrm{n}(\cdot)]$ is the electrostatic self-interaction energy for the charge-density $\mathrm{n}(\mathbf{r})$:

$$E_H[n(\cdot)] = \frac{1}{2} \int d\mathbf{r} d\mathbf{r}' \frac{n(\mathbf{r}) n(\mathbf{r}')}{|\mathbf{r} - \mathbf{r}'|}, \tag{1.7}$$

and the remaining term $\mathrm{E}_{\mathrm{xc}}[\mathrm{n}(\cdot)]$ referred to as the exchange-correlation functional defines all of our ignorance about the exact form of the Hohenberg-Kohn functional:

$$E_{xc}[n(\cdot)] = F[n(\cdot)] - T_0[n(\cdot)] - E_H[n(\cdot)]. \tag{1.8}$$

At the ground-state charge-density $\mathrm{n}_0(\mathbf{r})$, the exchange-correlation functional $\mathrm{E}_{\mathrm{xc}}[\mathrm{n}_0(\cdot)]$ is just the difference between the sum of the electronic kinetic energy $\mathrm{K}[\mathrm{n}_0(\cdot)]$ with the electron-electron

[1] According to the first Hohenberg-Kohn theorem, the electronic kinetic energy functional $\mathrm{T}_0[\mathrm{n}(\cdot)]$ is a well defined functional of $\mathrm{n}(\mathbf{r})$. For a system of non-interacting electrons, the Hohenberg-Kohn functional $\mathrm{F}_0[\mathrm{n}(\cdot)]$ is simply given by $\mathrm{T}_0[\mathrm{n}(\cdot)]$.

Coulomb interaction energy $\mathrm{W}[\mathrm{n}_0(\cdot)]$ for the fully interacting system, and that of the electronic kinetic energy $\mathrm{T}_0[\mathrm{n}_0(\cdot)]$ of the non-interacting system with the Hartree energy for the charge-density $\mathrm{n}_0(\mathbf{r})$. One hopes that the unknown term $\mathrm{E}_{\mathrm{xc}}[\mathrm{n}(\cdot)]$ is small enough so that it can be approximated easily with sufficient accuracy. Now, in terms of Eq. (1.6), the energy functional $\mathrm{E}[\mathrm{n}(\cdot)]$ can be written as:

$$E[n(\cdot)] = T_0[n(\cdot)] + E_H[n(\cdot)] + E_{xc}[n(\cdot)] + \int d\mathbf{r} n(\mathbf{r}) V_{ext}(\mathbf{r}). \tag{1.9}$$

In order to obtain the ground-state energy of the fully interacting system, we apply the second Hohenberg-Kohn theorem and minimize the energy functional $\mathrm{E}[\mathrm{n}(\cdot)]$ as given in Eq. (1.9) with respect to the charge-density $\mathrm{n}(\mathbf{r})$, under the constraint of a constant electron number N:

$$\int d\mathbf{r} n(\mathbf{r}) = N. \tag{1.10}$$

The resulting equation is:

$$\frac{\delta T_0[n(\cdot)]}{\delta n(\mathbf{r})} + V_H(\mathbf{r}) + V_{xc}(\mathbf{r}) + V_{ext}(\mathbf{r}) = \mu, \tag{1.11}$$

where the Hartree potential $\mathrm{V}_{\mathrm{H}}(\mathbf{r})$ is:

$$V_H(\mathbf{r}) = \int d\mathbf{r}' \frac{n(\mathbf{r}')}{|\mathbf{r} - \mathbf{r}'|}, \tag{1.12}$$

the unknown exchange-correlation potential $\mathrm{V}_{\mathrm{xc}}(\mathbf{r})$ is:

$$V_{xc}(\mathbf{r}) = \frac{\delta E_{xc}[n(\cdot)]}{\delta n(\mathbf{r})}, \tag{1.13}$$

and μ is a Lagrange multiplier associated with the constraint Eq. (1.10). If we apply the second Hohenberg-Kohn theorem to a system of N non-interacting electrons moving in an effective potential $\mathrm{V}_{\mathrm{eff}}(\mathbf{r})$ defined as:

$$V_{eff}(\mathbf{r}) = V_H(\mathbf{r}) + V_{xc}(\mathbf{r}) + V_{ext}(\mathbf{r}), \tag{1.14}$$

then the same equation as Eq. (1.11) will be obtained. In light of this observation, solving the fully interacting many-body problem is equivalent to solving the problem of N non-interacting electrons moving in an effective potential $\mathrm{V}_{\mathrm{eff}}(\mathbf{r})$ given by Eq. (1.14), as both problems will yield the same ground-state charge-density $\mathrm{n}(\mathbf{r})$.

The problem of N interacting electrons is now reduced to that of solving an equivalent one-body Schrödinger equation for N non-interacting electrons:

$$\Big\{ -\frac{1}{2}\frac{\partial^2}{\partial \mathbf{r}^2} + V_H(\mathbf{r}) + V_{xc}(\mathbf{r}) + V_{ext}(\mathbf{r}) \Big\} \psi_n(\mathbf{r}) = \epsilon_n \psi_n(\mathbf{r}), \tag{1.15}$$

where ϵ_{n} is the one-body Kohn-Sham energy and $\psi_{\mathrm{n}}(\mathbf{r})$ is the corresponding Kohn-Sham orbital. The ground-state charge-density $\mathrm{n}_0(\mathbf{r})$ is evaluated from the N lowest lying Kohn-Sham orbitals as:

$$n_0(\mathbf{r}) = \sum_{i=1}^{N} |\psi_n(\mathbf{r})|^2. \tag{1.16}$$

In the end, the ground-state energy of the original fully interacting system can be calculated as:

$$E_0[n_0(\cdot)] = \sum_n \epsilon_n - \int d\mathbf{r} n_0(\mathbf{r}) V_{xc}(\mathbf{r}) - E_H[n_0(\cdot)] + E_{xc}[n_0(\cdot)]. \tag{1.17}$$

Eqs. (1.15)-(1.17) are known as the famous set of Kohn-Sham equations, which in practice are usually solved self-consistently by using iterative approaches.

1.1.3 Approximations for the Exchange and Correlation

The Kohn-Sham formulation of DFT based on the two Hohenberg-Kohn theorems is exact in theory. However, in practice the exact form of the complicated exchange-correlation functional $\mathrm{E_{xc}[n(\cdot)]}$ is generally unknown and approximations must be made for it. The efficiency and the accuracy of the actual applications of DFT clearly depend on the quality of the approximation for $\mathrm{E_{xc}[n(\cdot)]}$.

Many approximations of different complexities have been developed for the exchange-correlation functional $\mathrm{E_{xc}[n(\cdot)]}$. Among all of them, the local density approximation (LDA) suggested by Kohn and Sham is the simplest one, and has been widely used in practical DFT calculations [40]. In LDA, the exchange-correlation functional $\mathrm{E_{xc}[n(\cdot)]}$ of an inhomogeneous system of interacting electrons is calculated as if at any position $\mathbf{r}$, the exchange-correlation energy per particle was the same as that of a homogeneous electron gas with the same charge-density $\mathrm{n}(\mathbf{r})$:

$$E_{xc}^{LDA}[n(\cdot)] = \int d\mathbf{r} n(\mathbf{r}) \epsilon_{xc}(n(\mathbf{r})), \tag{1.18}$$

where $\epsilon_{\mathrm{xc}}(\mathrm{n})$ indicates the exchange-correlation energy per particle of a homogeneous electron gas with a constant charge-density n. For a homogeneous electron gas, the exchange part of $\epsilon_{\mathrm{xc}}(\mathrm{n})$ can be given a simple analytical form as a function of n [53], while the correlation part can be calculated accurately by using quantum Monte-Carlo methods [54]. The functional derivative of Eq. (1.18) gives the LDA exchange-correlation potential $\mathrm{V_{xc}^{LDA}}(\mathbf{r})$:

$$V_{xc}^{LDA}(\mathbf{r}) = \epsilon_{xc}(n(\mathbf{r})) + n(\mathbf{r}) \frac{d\epsilon_{xc}(n)}{dn}\Big|_{n=n(\mathbf{r})}. \tag{1.19}$$

In principle, LDA becomes exact in the limit of slowly varying electronic charge-densities. Nevertheless, it works remarkably well even for very inhomogeneous systems, which can be understood to some extent by exploiting the properties of the exchange-correlation hole [55]. LDA has been shown to reproduce well the experimental results for the structural and vibrational properties of weakly correlated systems. However, the binding energies of molecules and the cohesive energies of solids are usually overestimated, and the bond lengths are correspondingly underestimated [56].

The generalized gradient approximation (GGA) first proposed by Perdew and Wang is a popular scheme for the improvement of LDA [57]. GGA is better than LDA in that it also takes into account the inhomogeneity of the charge-density as compared with the homogeneous electron gas. In GGA, the exchange-correlation energy per particle ϵ_{xc} does not only depend on the local charge-density

$\mathrm{n}(\mathbf{r})$, but also depends on its gradient $\nabla \mathrm{n}(\mathbf{r})$:

$$E_{xc}^{GGA}[n(\cdot)] = \int d\mathbf{r} n(\mathbf{r}) \epsilon_{xc}^{GGA}(n(\mathbf{r}), \nabla n(\mathbf{r})), \tag{1.20}$$

where $\epsilon_{\mathrm{xc}}^{\mathrm{GGA}}(\mathrm{n}(\mathbf{r}), \nabla \mathrm{n}(\mathbf{r}))$ is the GGA exchange-correlation energy per particle at position $\mathbf{r}$. GGA generally gives improved results for the binding and cohesive energies and the bond lengths, especially in the cases when the electronic charge-densities are more rapidly varying, though sometimes it could overcorrect the errors given by LDA [58].

LDA and GGA exchange-correlation functionals parametrized under different schemes usually work well for weakly correlated systems, but not for strongly correlated ones. Some other types of exchange-correlation functionals such as non-local functionals [59, 60], orbital-dependent functionals [61–64] and hybrid functionals [65, 66] have been developed, and for some systems can improve the results obtained with LDA and GGA. However, these functionals require more computational effort, and many of them are neither widely accepted, nor throughly tested. Note that spin dependence can be properly generalized to different types of approximated exchange-correlation functionals to account for the effects of spin polarization [67]. In this work, LDA is mainly used for the exchange-correlation functional in our study of gold clusters.

1.1.4 The Plane-Wave Pseudopotential Approach

The plane-wave pseudopotential approach is one of the most popular schemes in the practical application of DFT to the study of the ground-state properties of real materials. The heart of this method is to use a plane-wave basis set to represent Kohn-Sham orbitals, and to use pseudopotentials to account for the interactions between ionic cores and valence electrons.

The Plane-Wave Basis Sets

For computational convenience, periodic boundary conditions are often used in DFT calculations, not only for extended systems, but also for finite ones. In periodic boundary conditions, an isolated system is represented by a supercell periodically repeated so that Kohn-Sham orbitals can be expanded in terms of plane-waves:

$$\psi_n(\mathbf{r}) = \sum_{\mathbf{G}} c_{\mathbf{G}}^n e^{i\mathbf{G}\mathbf{r}}, \tag{1.21}$$

where $\mathbf{G}$ is the reciprocal lattice vector, and $\mathrm{c}_{\mathbf{G}}^{\mathrm{n}}$ is the component of the plane-wave representation of the orbital $\psi_{\mathrm{n}}(\mathbf{r})$ corresponding to the vector $\mathbf{G}$. In practice, the number of plane-waves is restricted such that the kinetic energies of the plane waves are smaller than a cutoff $\mathrm{E}_{\mathrm{cut}}$[2]:

$$\frac{1}{2}|\mathbf{G}|^2 < E_{cut}. \tag{1.22}$$

[2] As the charge-density is evaluated according to Eq. (1.16) as the sum of the square moduli of Kohn-Sham orbitals, it can also be represented by a plane-wave basis set, but the cutoff that restricts the number of plane-waves is four times as large as that for the Kohn-Sham orbitals as in Eq. (1.22).

Compared with other basis sets, plane-wave basis sets are advantageous in many aspects. As indicated in Eq. (1.21), they give a simple and straightforward representation of Kohn-Sham orbitals. In terms of plane-waves, the matrix elements of the Kohn-Sham Hamiltonian can be calculated efficiently, and the convergence of the calculated results from DFT calculations can be checked systematically by increasing the $\mathrm{E_{cut}}$ cutoff. Moreover, since plane-waves are independent of nuclear positions, atomic forces can be calculated directly without having to add any auxiliary term.

The Pseudopotential Method

Due to the strong oscillation of atomic orbitals in the vicinity of nuclei, a direct expansion of Kohn-Sham orbitals in a plane-wave basis requires a very large basis size to achieve a satisfactory accuracy, and is thus computationally expensive. It is possible to simply the problem if we consider the different properties of two groups of electrons, valence electrons and core electrons. Valence electrons are higher in energy, and are the ones that participate in chemical bonding. In fact, the smooth components of valence orbitals at distances far from the atomic nuclei determine most properties of the chemical bonding. In contrast to valence electrons, the energies of core electrons are much lower. Core electrons are strongly bound to the atomic nuclei and stay almost unchanged in different chemical environments. In an atom, the core electrons together with the nuclei can be considered as an ionic core.

In view of the above physical facts, the problem can be very much simplified by the pseudopotential method. In this method, so-called pseudopotentials are constructed so as to represent the interactions between valence electrons and ionic cores. All the degrees of freedom associated with core electrons are eliminated by assuming that their energies and orbitals remain unchanged when atoms form chemical bonds. Therefore, only valence electrons need to be considered explicitly. By solving the Kohn-Sham equations with pseudopotentials, the same energies as in the all-electron calculation should be obtained for the Kohn-Sham states. The resulting pseudo orbitals are smooth and nodeless in the core region, and identical to the corresponding all-electron ones beyond some distance $\mathrm{r_c}$ from the nucleus which is called the cutoff radius. Pseudopotentials are transferable, in the sense that they should give correct results in different chemical environments. Since pseudo orbitals are smooth, they can be efficiently represented by plane-waves, making the many advantages of the plane-wave basis possible. Relativistic effects can be incorporated into pseudopotentials without having to be considered explicitly for valence electrons in the Kohn-Sham equations [68].

In DFT calculations, one most commonly used type of pseudopotentials is the norm-conserving pseudopotential [69]. Norm-conserving pseudopotentials satisfy the condition that, for each pseudo orbital, there is a chosen core radius $\mathrm{r_c}$, within which the integrated charge-density agrees with the corresponding all-electron one. This condition guarantees that each pseudo orbital agrees with the corresponding all-electron one at distances beyond $\mathrm{r_c}$. Smaller values of $\mathrm{r_c}$ generally lead to better transferability of pseudopotentials, but in the meanwhile make the plane-wave representation

of pseudo orbitals more expensive.

Traditionally, norm-conserving pseudopotentials are formulated as:

$$\hat{V}^{PS} = V_{loc}^{PS}(r) + \sum_{l}(V_{l}^{PS}(r) - V_{loc}^{PS}(r))\hat{P}_{l}, \tag{1.23}$$

where $\mathrm{V}_{\mathrm{loc}}^{\mathrm{PS}}(\mathrm{r})$ is a long-range local term that behaves as $-\mathrm{Z_v}/\mathrm{r}$ for $\mathrm{r} \to \infty$, $\mathrm{Z_v}$ being the number of valence electrons, and the sums on the right hand side of the above equation represent short-range non-local terms. $\mathrm{V}_{\mathrm{l}}^{\mathrm{PS}}(\mathrm{r})$ is the pseudopotential channel constructed separately for each angular momentum l, which is selected for each l by the projection operator $\hat{\mathrm{P}}_{\mathrm{l}}$. The non-local terms vanish beyond the cutoff radius $\mathrm{r_c}$, due to the fact that all $\mathrm{V}_{\mathrm{l}}^{\mathrm{PS}}(\mathrm{r})$'s coincide outside $\mathrm{r_c}$. Since $\hat{\mathrm{P}}_{\mathrm{l}}$ does not act on the radial part of the position vector $\mathbf{r}$, $\hat{\mathrm{V}}^{\mathrm{PS}}$ is still an operator that depends locally on r. Therefore, the pseudopotential formulated in Eq. (1.23) is actually in a semi-local form. This semi-local form looks simple, but the difficulty involved in the plane-wave representation of the semi-local terms makes it computationally inconvenient.

Alternatively, the semi-local form as given in Eq. (1.23) can be recast into a computationally more efficient fully non-local form:

$$\hat{V}^{PS} = V_{loc}^{PS}(r) + \sum_{ij}|\beta_i\rangle B_{ij}\langle\beta_j|, \tag{1.24}$$

where $\beta_{\mathrm{i}}(\mathbf{r})$'s are a few projection functions that vanish for $\mathrm{r} > \mathrm{r_c}$. A practical scheme for the transformation of semi-local pseudopotentials into fully non-local ones was introduced by Kleinman and Bylander [70]. Vanderbilt showed that fully non-local pseudopotentials can also be constructed directly from all-electron calculations of atoms [71]. Fully non-local pseudopotentials usually work well, but may fail badly in the cases when ghost states with wrong number of nodes appear.

In the pseudopotential method, it is difficult to treat nodeless states that are present in the valence manifold, such as the 2p states of first-row elements and the 3d states of first-row transition metals. Due to the nodeless nature of these states, their pseudo orbitals are not much different from the corresponding all-electron ones and are strongly localized in the core region, thus require a large number of plane-waves for their representation. To overcome this difficulty, Vanderbilt introduced a scheme for constructing the so-called ultrasoft pseudopotentials [71, 72], such that the norm-conservation condition can be relaxed and the resulting pseudo orbitals can be much smoother. Ultrasoft pseudopotentials are softer than norm-conserving ones, since they produce pseudo orbitals that can be expanded with a much smaller plane-wave basis set. Although some complications are introduced in the representation of the Kohn-Sham equations, which can counteract the advantages of ultrasoft pseudopotential, considerable computational gain can be achieved in many cases.

In practice, pseudopotentials are generate from the results of all-electron calculations of isolated atoms. Many factors such as valence-core partition and the pseudization radius $\mathrm{r_c}$ can influence the quality of the generated pseudopotentials. One often needs to find a good compromise between the transferability and the softness. In this work, we generated two norm-conserving pseudopotentials

for the GW calculations of gold clusters. For the optimizations of the geometries, we employ an ultrasoft pseudopotential.

1.2 Many-Body Perturbation Theory

In this section, we briefly describe many-body perturbation theory, with emphasis on the GW approximation. We first discuss the motivation for many-body perturbation theory. Following this, we introduce the one-particle and two-particle Green's functions. Afterwards, we present the set of Hedin's equations and the GW approximation made on top of them.

1.2.1 Motivation

The accurate description of the electronic excitation properties of many-particle systems has been an important goal in first principles electronic structure calculations. This is particularly true if one considers the fact that it is the excitation properties that are measured in most spectroscopic experiments. Concerning electronic excitations, the most elementary type is the removal/addition of an electron from/to a system originally in its ground-state. These processes are accessible to direct/inverse photoemission experiments, which are schematically illustrated in Fig. [1.1]. In direct photoemission, a photon with energy $\mathrm{h}\nu$ impinges onto the system, and ejects an electron, whose kinetic energy $\mathrm{E_K}$ is measured at some distance. The conservation of energy gives:

$$\begin{aligned} \epsilon_i &= E_0^N - E_i^{N-1} \\ &= E_K - h\nu, \end{aligned} \tag{1.25}$$

where $\mathrm{E_0^N}$ is the ground-state energy of the original N-electron system, $\mathrm{E_i^{N-1}}$ is the energy of the resulting system in the i-th $(\mathrm{N}-1)$-electron state (the 0-th state being the ground-state), and $(-\epsilon_\mathrm{i})$ gives the energy cost of removing an electron. For a finite system, the (vertical) ionization potential (IP) is given by $(-\epsilon_0)$. Inverse photoemission is the opposite process in which an electron with energy $\mathrm{E_K}$ impinges onto the system and a photon with energy $\hbar\nu$ is emitted. The conservation of energy gives in this case:

$$\begin{aligned} \epsilon_i &= E_i^{N+1} - E_0^N \\ &= E_K - h\nu, \end{aligned} \tag{1.26}$$

where $\mathrm{E_i^{N+1}}$ is the energy of the resulting system in the i-th $(\mathrm{N}+1)$-electron state (the 0-th state being the ground-state), and $(-\epsilon_\mathrm{i})$ gives the energy gain of adding an electron to the system. For a finite system, the (vertical) electron affinity (EA) is given by $(-\epsilon_0)$. The difference between the lowest energy cost of removing an electron and the largest energy gain of adding an electron defines the fundamental quasiparticle band gap. The energies measured in a photoemission experiment give rise to a photoemission spectrum. If the photoemission experiment is angle-resolved, then by applying in addition the conservation of momentum, the obtained photoemission spectrum will give

directly the band structure of solids. The photoemission spectrum can in general be described in terms of quasiparticle excitations determined by the quasiparticle equation. For a system of non-interacting electrons, the quasiparticle equation is nothing but a one-body Schrödinger equation.

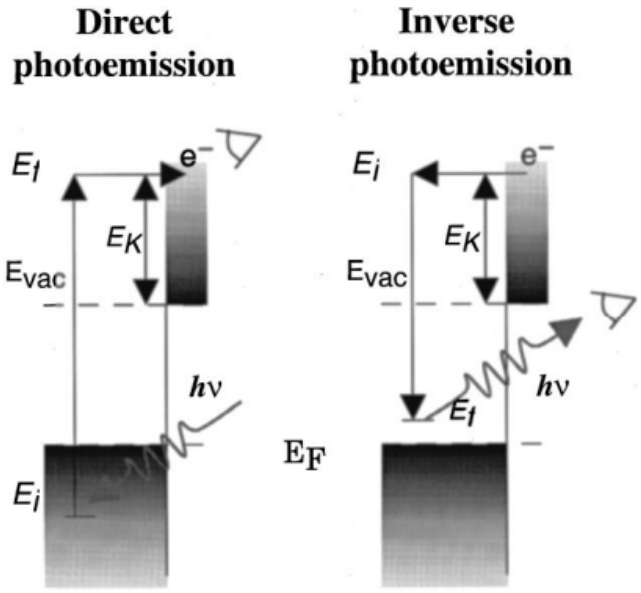

Figure 1.1: Schematic illustration of direct and inverse photoemission experiments. This figure is taken from Ref. [73].

Although DFT has been proved very successful for describing the ground-state properties, such as the cohesive, structural and vibrational properties, of a wide range of materials, it is usually not an appropriate method of choice for the investigation of electronic excitations. In DFT, since the Kohn-Sham equation Eq. (1.15) is a one-electron Schrödinger equation, one is often tempted to identify its eigenvalues as one-electron removal and addition energies. This has no theoretical foundation, as the Kohn-Sham equation Eq. (1.15) is only a mathematical tool for obtaining ground-state properties and its eigenvalues should not be interpreted as electron removal and addition energies, but has been a common practice for a long time. The only exception is the DFT highest occupied molecular orbital energy, which in principle for finite systems gives the exact (vetical) IP and for metals equals the exact chemical potential [75], but current approximations for the exchange-correlation functional mostly fail to do so. As a consequence, many problems arise due to such a way of interpreting Kohn-Sham energies [73, 76, 77]. Among all of them, one is that the band gaps of semiconductors and insulators are often severely underestimated by DFT eigeneneriges. In Fig. [1.2], the theoretical fundamental band gaps from DFT-LDA calculations are compared with the experimental values for some sp semiconductors. Clearly, the experimental band gaps are systematically underestimated by the DFT-LDA results. Another problem is that DFT electronic density of states (DOS) can not give the correct quasiparticle spectrum. In Fig. [1.3], the theoretical DFT-LDA DOS spectrum and the experimental direct photoemission spectrum are compared with each other for the free-base

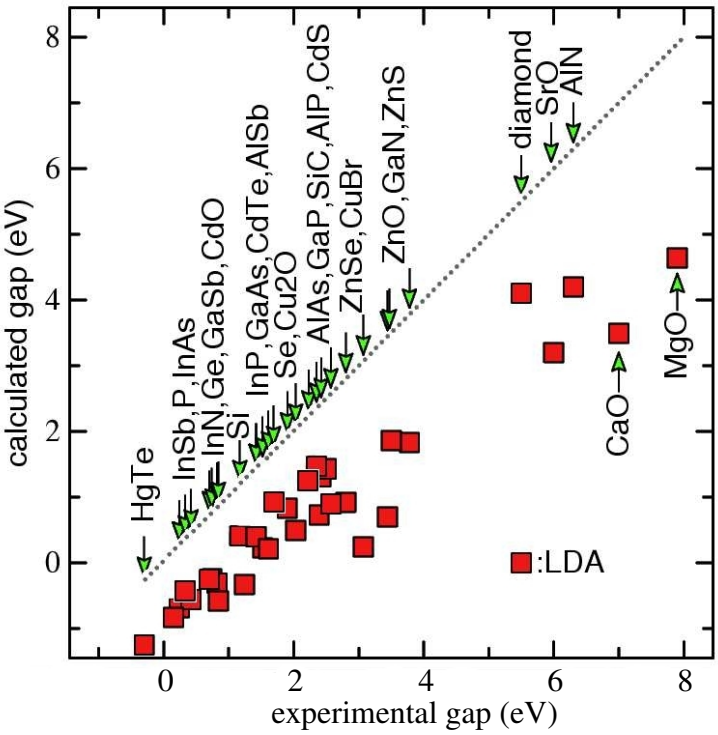

Figure 1.2: Comparison between the calculated DFT-LDA fundamental band gaps (left scale) and the experimental ones (bottom scale) for some sp semiconductors. This figure is adapted from Ref. [74]

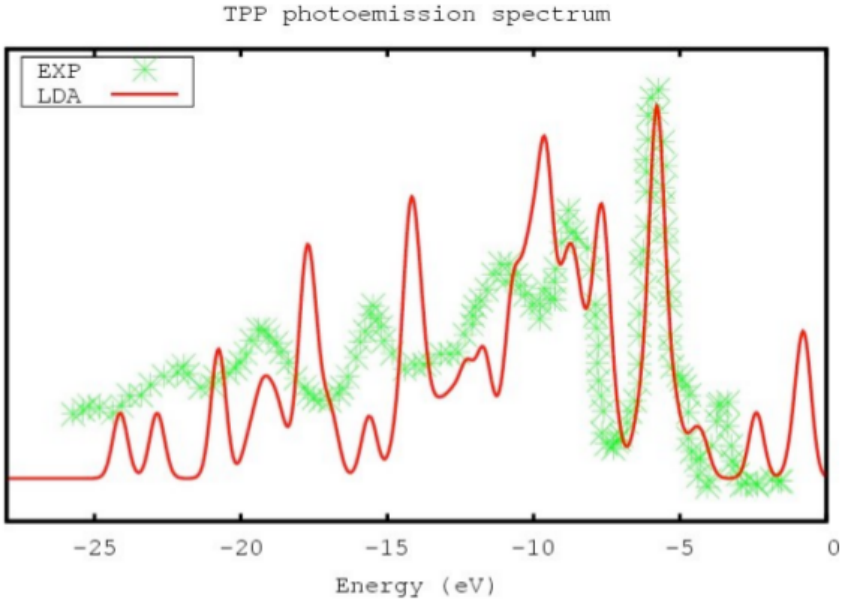

Figure 1.3: Comparison between the calculated DFT-LDA electronic density of states and the photoemission spectrum from a direct photoemission measurement for the free-base tetraphenylporphyrin molecule ($TPPH_2$) ($C_{44}H_{30}N_4$). A Gaussian broadening of 0.25 eV is for the theoretical curve. See Ref. [48] for more details.

tetraphenylporphyrin molecule ($TPPH_2$). A strong disagreement is found between the theoretical curve and the experimental one, especially concerning the positions of the peaks. For finite systems, there is the particular problem that (the minus of) the DFT highest occupied molecular orbital (HOMO) energy often severely underestimates the (vertical) IP, and (the minus of) the DFT lowest unoccupied molecular orbital (LUMO) energy often severely overestimates the (vertical) EA.

Despite all the failures, there is a case when DFT is good in describing electronic excitations, that is, when the IPs and the EAs of finite systems are calculated with the ΔSCF method. In the ΔSCF method, the total energies of the cationic (($\mathrm{N}-1$)-electron), the neutral (N-electron) and the anionic (($\mathrm{N}+1$)-electron) systems are calculated from DFT at the same atomic configuration as that of the neutral one. Then, the IP is obtained as the energy difference between the total energy of the cationic system and that of the neutral one, and the EA is evaluated as the energy difference between the total energy of the neutral system and that of the anionic one. Since DFT is usually pretty accurate in describing total energies, there is the hope that the IP and the EA calculated as such may agree well with experiment. Indeed, the IP and the EA calculated at the ΔSCF level usually compare quite well with experiment, provided that the theoretical structure of the neutral system used in the DFT calculations agrees with the experimental one [78]. In theoretical studies, the ΔSCF results can be used as a first reference for the IP and the EA, when the experimental values or more accurate quantum chemistry results for them are not available. Note that, as it goes to the thermodynamic limit when the size of the system are infinite and the charge-density of the HOMO state becomes zero, the IP calculated from ΔSCF would approach the minus of the DFT HOMO energy.

To study electronic excitations, especially those other than the IP and the EA, more sophisticated techniques based on many-body perturbation theory (MBPT) [41–43] are called for. The GW approximation [44] based on MBPT is the state of the art method which allows the accurate description of the quasiparticle spectra for both molecular and extended systems [73, 76, 77]. In addition to calculating excitation energies, the GW approximation can also be used to obtain the ground-state energy [73, 76, 77].

1.2.2 The Green's Functions

The fundamental formulation of MBPT is rooted in the theory of Green's functions. For a many-body system of interacting electrons, the one-particle Green's function G is defined as:

$$\begin{aligned} G(\mathbf{r}t,\mathbf{r}'t') &= -i\langle N,0|\hat{T}[\hat{\psi}(\mathbf{r},t)\hat{\psi}^{\dagger}(\mathbf{r}',t')]|N,0\rangle \\ &= \begin{cases} -i\langle N,0|\hat{\psi}(\mathbf{r},t)\hat{\psi}^{\dagger}(\mathbf{r}',t')|N,0\rangle, & \text{for } t>t', \\ i\langle N,0|\hat{\psi}^{\dagger}(\mathbf{r}',t')\hat{\psi}(\mathbf{r},t)|N,0\rangle, & \text{for } t<t', \end{cases} \end{aligned} \tag{1.27}$$

where $|\mathrm{N},0\rangle$ is the ground-state ($|\mathrm{N},\mathrm{i}\rangle$ being the i-th state with energy $\mathrm{E}_{\mathrm{i}}^{\mathrm{N}}$) of the N-electron system corresponding to a Hamiltonian operator $\hat{\mathrm{H}}$ such as defined by Eqs. (1.2)-(1.5), $\hat{\mathrm{T}}$ is the time-ordering operator which reorders a set of time-dependent operators such that operators with larger

time are on the left of those with smaller time, and $\hat{\psi}(\mathbf{r}, \mathrm{t})$ is the fermion annihilation operator in the Heisenberg representation which destroys an electron at position $\mathbf{r}$ and time t, defined as:

$$\hat{\psi}(\mathbf{r}, t) = e^{i\hat{H}t}\hat{\psi}(\mathbf{r})e^{-i\hat{H}t}, \tag{1.28}$$

$\hat{\psi}^{\dagger}(\mathbf{r}, \mathrm{t})$ being the corresponding fermion creation operator in the Heisenberg representation. In the Schrödinger representation, the fermion annihilation operator $\hat{\psi}(\mathbf{r})$ and the fermion creation operator $\hat{\psi}^{\dagger}(\mathbf{r})$ obey the following anticommutation rules:

$$\{\hat{\psi}(\mathbf{r}), \hat{\psi}^{\dagger}(\mathbf{r}')\} = \delta(\mathbf{r} - \mathbf{r}'), \tag{1.29}$$

$$\{\hat{\psi}(\mathbf{r}), \hat{\psi}(\mathbf{r}')\} = \{\hat{\psi}^{\dagger}(\mathbf{r}), \hat{\psi}^{\dagger}(\mathbf{r}')\} = 0. \tag{1.30}$$

For $\mathrm{t} > \mathrm{t}'$, the one-particle Green's function describes the probability amplitude that an electron created at position $\mathbf{r}'$ and time t' in the system propagates to position $\mathbf{r}$ at time t. And for time $\mathrm{t} < \mathrm{t}'$, the one-particle Green's function gives the probability amplitude that a hole created at position $\mathbf{r}$ and time t by removing an electron from the system propagates to position $\mathbf{r}'$ at time t'. For a time-independent Hamiltonian $\hat{\mathrm{H}}$, the one-particle Green's function $\mathrm{G}(\mathbf{r}\mathrm{t}; \mathbf{r}'\mathrm{t}')$ does not depend individually on t and t', but only on the time difference $\mathrm{t} - \mathrm{t}'$. Therefore, it can be written equivalently as $\mathrm{G}(\mathbf{r}, \mathbf{r}'; \mathrm{t} - \mathrm{t}')$.

Now we introduce the quasiparticle amplitude $\psi_{\mathrm{i}}^{\mathrm{N}\pm1}(\mathbf{r})$ and the corresponding quasiparticle energy $\epsilon_{\mathrm{i}}^{\mathrm{N}\pm1}$, defined as:

$$\begin{cases} \psi_i^{N-1}(\mathbf{r}) = \langle N-1, i|\hat{\psi}(\mathbf{r})|N, 0\rangle \text{ with } \epsilon_i^{N-1} = E_0^N - E_i^{N-1}, & \text{for } \epsilon_i^{N-1} < \mu, \\ \psi_i^{N+1}(\mathbf{r}) = \langle N, 0|\hat{\psi}(\mathbf{r})|N+1, i\rangle \text{ with } \epsilon_i^{N+1} = E_i^{N+1} - E_0^N, & \text{for } \epsilon_i^{N+1} \geq \mu, \end{cases} \tag{1.31}$$

where we use μ to represent (the minus of) the EA:

$$\mu = E_0^{N+1} - E_0^N. \tag{1.32}$$

The quasiparticle energies $\epsilon_{\mathrm{i}}^{\mathrm{N}-1}$ and $\epsilon_{\mathrm{i}}^{\mathrm{N}+1}$ correspond simply to the electron removal and addition energies respectively. If it is a system of non-interacting electrons that is under consideration, then $\epsilon_{\mathrm{i}}^{\mathrm{N}-1}$ and $\epsilon_{\mathrm{i}}^{\mathrm{N}+1}$ would be the occupied and the empty non-interacting one-electron energies, and $\psi_{\mathrm{i}}^{\mathrm{N}-1}$ and $\psi_{\mathrm{i}}^{\mathrm{N}+1}$ would be the corresponding orbitals. For Eq. (1.31) to be valid, we must have:

$$E_0^{N+1} - E_0^N \geq E_0^N - E_0^{N-1}. \tag{1.33}$$

This is guaranteed by the convexity of the total energy at fixed atomic configuration as a function of the electron number N. Inserting the closure relation:

$$\sum_i |N \pm 1, i\rangle\langle N \pm 1, i| = \hat{1}_{N\pm1} \tag{1.34}$$

into Eq. (1.27) between the annihilation and the creation operators, and Fourier transforming the resulting expression, we obtain the Lehmann's representation of the one-particle Green's function:

$$G(\mathbf{r}, \mathbf{r}'; \omega) = \sum_i \frac{\psi_i^{N-1}(\mathbf{r})\psi_i^{N-1^*}(\mathbf{r}')}{\omega - \epsilon_i^{N-1} - i\eta} + \sum_i \frac{\psi_i^{N+1}(\mathbf{r})\psi_i^{N+1^*}(\mathbf{r}')}{\omega - \epsilon_i^{N+1} + i\eta}, \tag{1.35}$$

where η is a positive infinitesimal number used to converge the Fourier transform. In the frequency domain, the one-particle Green's function has poles corresponding to $\epsilon_{\mathrm{i}}^{\mathrm{N}-1} + \mathrm{i}\eta$ on the positive complex plane for $\omega < \mu$, and poles corresponding to $\epsilon_{\mathrm{i}}^{\mathrm{N}+1} - \mathrm{i}\eta$ on the negative complex plane for $\omega \geq \mu$. The small imaginary part $\pm\mathrm{i}\eta$ reveals that the quasiparticle has an infinite lifetime. In the case of an infinite system, the quasiparticle energy $\epsilon_{\mathrm{i}}^{\mathrm{N}\pm1}$ becomes complex, corresponding to a finite lifetime of the quasiparticle.

From the one-particle Green's function, we can obtain many fundamental properties of the system, such as the expectation value of any one-particle operator in the ground-state, the ground-state energy, and most relevant to this work, the electron removal/addition energies measured in direct/inverse photoemission experiments [42, 43]. Compared with the full many-body wavefunctions, the one-particle Green's function contains much less information and is much less complicated, nevertheless, in principle many properties of the system, such as those mentioned above, can be calculated exactly from it. It is worth noticing that the ground-state charge-density $\mathrm{n}_0(\mathbf{r})$ can be calculated as:

$$n_0(\mathbf{r}) = -i \lim_{\eta \to 0} G(\mathbf{r}t, \mathbf{r}t + \eta). \tag{1.36}$$

Although the one-particle Green's function is powerful in describing one-particle excitation processes, it does not provide any direct knowledge of two-particle excitations, such as optical absorptions. In the optical absorption process, an electron is excited from an occupied state to an empty state by absorbing a photon, resulting in a hole originally occupied by the excited electron. Since the electron is not completely removed from the system, the description of this transition process requires the consideration of the interaction between both the electron and the hole. Therefore, the optical absorption is a two-particle process and can not be properly described by one-particle Green's functions. To investigate two-particle excitations, one often employs the two-particle Green's function, which is defined as:

$$G_2(1,2;1',2') = (-i)^2 \langle N,0|\hat{T}[\hat{\psi}(1)\hat{\psi}(2)\hat{\psi}^\dagger(2')\hat{\psi}^\dagger(1')]|N,0\rangle, \tag{1.37}$$

where we have used numbers to represent space and time coordinates, such as, 1 for ($\mathbf{r}_1$,t_1). The optical absorption process can be described by enforcing the time order $\mathrm{t}_1, \mathrm{t}_1' > \mathrm{t}_2, \mathrm{t}_2'$ or $\mathrm{t}_1, \mathrm{t}_1' < \mathrm{t}_2, \mathrm{t}_2'$. We won't dig more into the two-particle Green's function, as it is the investigation of one-particle electronic excitations that is the main concern of this work.

1.2.3 Hedin's Equations and the GW Approximation

The behavior of quasiparticles obeys the quasiparticle equation, which can be obtained from the equation of motion for the one-particle Green's function and the Lehmann's representation Eq. (1.35). In second quantization, the Hamiltonian operator defined by Eqs. (1.2)-(1.5) for a system of

interacting electrons can be equivalently written as:

$$\hat{H} = \int d\mathbf{r}\hat{\psi}^{\dagger}(\mathbf{r})\hat{h}(\mathbf{r})\hat{\psi}(\mathbf{r}) + \frac{1}{2}\iint d\mathbf{r}d\mathbf{r}'\hat{\psi}^{\dagger}(\mathbf{r})\hat{\psi}^{\dagger}(\mathbf{r}')v(\mathbf{r},\mathbf{r}')\hat{\psi}(\mathbf{r}')\hat{\psi}(\mathbf{r}), \tag{1.38}$$

where $\hat{\mathrm{h}}(\mathbf{r})$ is a one-body operator:

$$\hat{h}(\mathbf{r}) = -\frac{1}{2}\frac{\partial^2}{\partial\mathbf{r}^2} + V_{ext}(\mathbf{r}). \tag{1.39}$$

From the Heisenberg equation of motion for the fermion annihilation operator $\hat{\psi}(\mathbf{r},\mathrm{t})$:

$$\begin{aligned} i\frac{\partial\hat{\psi}(\mathbf{r},t)}{\partial t} &= [\hat{\psi}(\mathbf{r},t),\hat{H}] \\ &= \hat{h}(\mathbf{r})\hat{\psi}(\mathbf{r},t) + \int d\mathbf{r}'v(\mathbf{r},\mathbf{r}')\hat{\psi}^{\dagger}(\mathbf{r}',t)\hat{\psi}(\mathbf{r}',t)\hat{\psi}(\mathbf{r},t), \end{aligned} \tag{1.40}$$

we find that the equation of motion for the one-particle Green's function $\mathrm{G}(\mathbf{r}\mathrm{t};\mathbf{r}'\mathrm{t}')$ is:

$$\begin{aligned} i\frac{\partial}{\partial t}G(\mathbf{r}t;\mathbf{r}'t') = \delta(\mathbf{r}-\mathbf{r}')\delta(t-t') + \hat{h}(\mathbf{r})G(\mathbf{r}t;\mathbf{r}'t') \\ - i\int d\mathbf{r}''v(\mathbf{r},\mathbf{r}'')\langle N,0|\hat{T}[\hat{\psi}^{\dagger}(\mathbf{r}'',t)\hat{\psi}(\mathbf{r}'',t)\hat{\psi}(\mathbf{r},t)\psi^{\dagger}(\mathbf{r}',t')]|N,0\rangle. \end{aligned} \tag{1.41}$$

For simplicity, we use numbers to represent space and time coordinates, and define in addition:

$$1^{+} = (\mathbf{r}_1, t_1+\eta), \tag{1.42}$$

$$\begin{aligned} v(1,2) &= v(\mathbf{r}_1-\mathbf{r}_2)\delta(t_1-t_2) \\ &= \frac{1}{|\mathbf{r}_1-\mathbf{r}_2|}\delta(t_1-t_2), \end{aligned} \tag{1.43}$$

$$\delta(1,2) = \delta(\mathbf{r}_1-\mathbf{r}_2)\delta(t_1-t_2), \tag{1.44}$$

where η is a positive infinitesimal number used to enforce the correct time order. Now Eq. (1.41) becomes:

$$i\frac{\partial}{\partial t_1}G(1,2) = \delta(1,2) + \hat{h}(1)G(1,2) + i\int d(3)v(1^{+},3)\langle N,0|\hat{T}[\hat{\psi}(1)\hat{\psi}(3)\hat{\psi}^{\dagger}(3^{+})\hat{\psi}^{\dagger}(2)]|N,0\rangle. \tag{1.45}$$

By employing the definition of the two-particle Green's function G_2 in Eq. (1.37), the equation of motion for the one-particle Green's function can be written in a simpler way as:

$$i\frac{\partial}{\partial t_1}G(1,2) = \delta(1,2) + \hat{h}(1)G(1,2) - i\int d(3)v(1^{+},3)G_2(1,3;2,3^{+}). \tag{1.46}$$

Later in this subsection, we show that it is possible to eliminate the two-particle Green's function $\mathrm{G}_2(1,3;2,3^{+})$ in the above equation by introducing a self-energy operator Σ which satisfies:

$$-i\int d(3)v(1^{+},3)G_2(1,3;2,3^{+}) = V_H(1)G(1,2) + \int d(3)\Sigma(1,3)G(3,2), \tag{1.47}$$

where $\mathrm{V_H}(1)$ is the Hartree potential defined by Eq. (1.12) for the ground-state charge-density $\mathrm{n}_0(\mathbf{r})$. Considering Eq. (1.47), Eq. (1.46) becomes:

$$\Big\{i\frac{\partial}{\partial t_1} - \hat{h}(1) - V_H(1)\Big\}G(1,2) - \int d(3)\Sigma(1,3)G(3,2) = \delta(1,2). \tag{1.48}$$

For a non-interacting system where the self-energy Σ vanishes, we have:

$$\Big\{ i\frac{\partial}{\partial t_1} - \hat{h}(1) - V_H(1) \Big\} G_0(1,2) = \delta(1,2), \tag{1.49}$$

where G_0 is the corresponding non-interacting one-particle Green's function. Combining Eq. (1.48) with Eq. (1.49), we obtain the Dyson equation for the one-particle Green's function:

$$G(1,2) = G_0(1,2) + \iint d(3)d(4) G_0(1,3)\Sigma(3,4)G(4,2) \tag{1.50}$$

Fourier transforming Eq. (1.48), we get the equation of motion for the fully-interacting one-particle Green's function in the frequency domain:

$$\{\omega - \hat{h}(\mathbf{r}) - V_H(\mathbf{r})\}G(\mathbf{r},\mathbf{r}';\omega) - \int d\mathbf{r}''\Sigma(\mathbf{r},\mathbf{r}'';\omega)G(\mathbf{r}'',\mathbf{r};\omega) = \delta(\mathbf{r}-\mathbf{r}'). \tag{1.51}$$

Substituting the Lehmann's representation Eq. (1.35) into Eq. (1.51), multiplying with $(\omega - \epsilon_{\mathrm{i}})$ on both sides of the resulting equation and taking the limit $\omega \to \epsilon_{\mathrm{i}}$, we obtain the quasiparticle equation:

$$\Big\{ -\frac{1}{2}\frac{\partial^2}{\partial \mathbf{r}^2} + V_H(\mathbf{r}) + V_{ext}(\mathbf{r}) \Big\}\psi_i(\mathbf{r}) + \int d\mathbf{r}'\Sigma(\mathbf{r},\mathbf{r}';\epsilon_i)\psi_i(\mathbf{r}') = \epsilon_i\psi_i(\mathbf{r}), \tag{1.52}$$

where ψ_{i} and ϵ_{i} are the quasiparticle amplitude and the quasiparticle energy respectively, which are defined in Eq. (1.31). The real part of ϵ_{i} gives the single-electron excitation energy and the imaginary part gives the excitation lifetime through its inverse. The quasiparticle equation Eq. (1.52) has the form of a one-body $\mathrm{Schrödinger}$ equation, which is similar to that of the Kohn-Sham equation Eq. (1.15). However, in contrast to the exchange-correlation potential $\mathrm{V_{xc}}(\mathbf{r})$, the self-energy $\Sigma(\mathbf{r},\mathbf{r}';\omega)$ is a non-local, energy-dependent, and non-hermitian operator. Therefore, although the quasiparticle amplitudes satisfy the closure relation:

$$\sum_i |\psi_i\rangle\langle\psi_i| = \hat{1}, \tag{1.53}$$

nothing makes it necessary for them to be orthonormal. In principle, the self-energy Σ contains all the complicated many-body exchange and correlation effects beyond the Hartree potential. Its presence makes Eq. (1.52) difficult to solve.

In 1965, Hedin proposed a set of self-consistent equations for the exact evaluation of the self-energy Σ, which are usually referred to as Hedin's equations [44]. Hedin's equations can be derived by employing Schwinger's functional derivative method [79, 80]. In order to do so, we introduce an additional auxiliary time-varying external potential $\mathrm{U}(1)$ which is set to zero in the end. The fully-interacting Green's functions now depend on $\mathrm{U}(1)$, but the equation of motion Eq. (1.46) remains valid, provided that $\hat{\mathrm{h}}(1)$ is replaced with $\hat{\mathrm{h}}(1) + \mathrm{U}(1)$. At this point, we introduce several related quantities. The reducible polarizability operator Π describes the response of the charge-density with respect to the changes in the external potential, and is defined as:

$$\Pi(1,2) = \frac{\delta n(1)}{\delta U(2)}\Big|_{U=0}. \tag{1.54}$$

The effective potential $\mathrm{U_{eff}}$ due to the changes in the external potential can be calculated as:

$$U_{eff}(1) = U(1) + \iint d(2)d(3)v(1,3)\Pi(3,2)U(2), \tag{1.55}$$

where the second term on the right hand side gives the induced potential due to the induced charge-density. In terms of $\mathrm{U_{eff}}$, the irreducible polarizability operator P is defined as:

$$P(1,2) = \frac{\delta n(1)}{\delta U_{eff}(1)}\Big|_{U=0}. \tag{1.56}$$

From Eq. (1.55), by using the chain rule for the functional derivative, we can obtain the relation between the two polarizability operators:

$$\begin{aligned}\Pi(1,2) &= \int d(3)\frac{\delta n(1)}{\delta U_{eff}(3)}\frac{\delta U_{eff}(3)}{\delta U(2)} \\ &= P(1,2) + \iint d(3)d(4)P(1,3)v(3,4)\Pi(4,2).\end{aligned} \tag{1.57}$$

The inverse of the dielectric matrix is:

$$\epsilon^{-1}(1,2) = \frac{\delta U_{eff}(1)}{\delta U(2)}\Big|_{U=0}. \tag{1.58}$$

From Eq. (1.55) and Eq. (1.57), we have:

$$\begin{aligned}\epsilon^{-1}(1,2) &= \delta(1,2) + \int d(3)v(1,3)\Pi(3,2) \\ &= \delta(1,2) + \int d(3)v(1,3)P(3,2) + \iiint d(3)d(4)d(5)v(1,3)P(3,4)v(4,5)\Pi(5,2) \\ &= \delta(1,2) + \int d(3)v(1,3)P(3,2) + \iiint d(3)d(4)d(5)v(1,3)P(3,4)v(4,5)P(5,2) \\ &\quad + \cdots .\end{aligned} \tag{1.59}$$

Inverting Eq. (1.59), we have the dielectric matrix as:

$$\epsilon(1,2) = \delta(1,2) - \int d(3)v(1,3)P(3,2). \tag{1.60}$$

Now we introduce the screened Coulomb interaction $\mathrm{W}(1,2)$, which describes the effective potential at point 2, due to the addition of a small unit test charge at point 1:

$$W(1,2) = \int d(3)\epsilon^{-1}(1,3)v(3,2). \tag{1.61}$$

By using Eq. (1.59), we can obtain the relation between the screened Coulomb interaction W and the polarizability operators P and Π:

$$\begin{aligned}W(1,2) &= v(1,2) + \iint d(3)d(4)v(1,3)\Pi(3,4)v(4,2) \\ &= v(1,2) + \iiint d(3)d(4)d(5)v(1,3)\frac{\delta n(3)}{\delta U_e f f(5)}\frac{\delta U_{eff}(5)}{\delta U(4)}v(4,2) \\ &= v(1,2) + \iiint d(3)d(4)d(5)v(1,3)P(3,5)\epsilon^{-1}(5,4)v(4,2) \\ &= v(1,2) + \iint d(3)d(4)v(1,3)P(3,4)W(4,2).\end{aligned} \tag{1.62}$$

In order to proceed further, we have to consider the two-particle Green's function G_2 involved in Eq. (1.47). By taking the functional derivative of the fully-interacting one-particle Green's function G with respect to the external potential U, it can be found that [44]:

$$\frac{\delta G(1,2)}{\delta U(3)}\Big|_{U=0} = G(1,2)G(3,3^+) - G_2(1,3;2,3^+). \tag{1.63}$$

Substituting Eq. (1.63) into Eq. (1.47), and taking use of Eq. (1.36), we have:

$$\int d(3)\Sigma(1,3)G(3,2) = i\int d(3)v(1^+,3)\frac{\delta G(1,2)}{\delta U(3)}. \tag{1.64}$$

From the definition of the inverse of the one-particle Green's function:

$$\int d(2)G(1,3)G^{-1}(3,2) = \delta(1,2), \tag{1.65}$$

it follows that:

$$\frac{\delta G(1,2)}{\delta U(3)} = -\int d(4)d(5)G(1,4)\frac{\delta G^{-1}(4,5)}{\delta U(3)}G(5,2), \tag{1.66}$$

which, if substituted into Eq. (1.64), yields:

$$\Sigma(1,2) = -i\iint d(3)d(4)v(1^+,3)G(1,4)\frac{\delta G^{-1}(4,2)}{\delta U(3)}. \tag{1.67}$$

We see that indeed the two-particle Green's function $\mathrm{G}_2(1,3;2,3^+)$ involved in the equation of motion Eq. (1.46) for the one-particle Green's function can be eliminated with the help of the self-energy operator Σ which can be formally defined as in Eq. (1.67). From Eq. (1.67), we can further have:

$$\begin{aligned}
\Sigma(1,2) &= -i\iiint d(3)d(4)d(5)v(1^+,3)G(1,4)\frac{\delta G^{-1}(4,2)}{\delta U_{eff}(5)}\frac{\delta U_{eff}(5)}{\delta U(3)} \\
&= -i\iiint d(3)d(4)d(5)v(1^+,3)G(1,4)\frac{\delta G^{-1}(4,2)}{\delta U_{eff}(5)}\epsilon^{-1}(5,3) \\
&= i\iint d(3)d(4)G(1,4)\Gamma(4,2;3)W(3,1^+),
\end{aligned} \tag{1.68}$$

where the vertex function Γ is defined as:

$$\Gamma(1,2;3) = -\frac{\delta G^{-1}(1,2)}{\delta U_{eff}(3)}\Big|_{U=0}. \tag{1.69}$$

Using Eq. (1.48), we have:

$$\begin{aligned}
\Gamma(1,2;3) &= \delta(1,2)\delta(1,3) + \frac{\delta\Sigma(1,2)}{\delta U_{eff}(3)} \\
&= \delta(1,2)\delta(1,3) + \iint d(4)d(5)\frac{\delta\Sigma(1,2)}{\delta G(4,5)}\frac{\delta G(4,5)}{\delta U_{eff}(3)} \\
&= \delta(1,2)\delta(1,3) + \iiiint d(4)d(5)d(6)d(7)\frac{\delta\Sigma(1,2)}{\delta G(4,5)}G(4,6)\frac{\delta G^{-1}(6,7)}{\delta U_{eff}(3)}G(7,5) \\
&= \delta(1,2)\delta(1,3) + \iiiint d(4)d(5)d(6)d(7)\frac{\delta\Sigma(1,2)}{\delta G(4,5)}G(4,6)\Gamma(6,7;3)G(7,5),
\end{aligned} \tag{1.70}$$

where we have used the identity in Eq. (1.66), with U replaced by $\mathrm{U_{eff}}$. Similarly, for the irreducible polarizability P:

$$\begin{aligned} P(1,2) &= -i\frac{\delta G(1,1^+)}{\delta U_{eff}(2)} \\ &= i\iint d(3)d(4)G(1,3)\frac{\delta G^{-1}(3,4)}{\delta U_{eff}(2)}G(4,1^+) \\ &= -i\iint d(3)d(4)G(1,3)\Gamma(3,4;2)G(4,1^+). \end{aligned} \tag{1.71}$$

Summarizing the above results, we obtain the set of self-consistent Hedin's equations:

$$\Sigma(1,2) = i\int d(3)d(4)G(1,4)\Gamma(4,2;3)W(3,1^+), \tag{1.72}$$

$$G(1,2) = G_0(1,2) + \iint d(3)d(4)G_0(1,3)\Sigma(3,4)G(4,2), \tag{1.73}$$

$$W(1,2) = v(1,2) + \iint d(3)d(4)v(1,3)P(3,4)W(4,2), \tag{1.74}$$

$$P(1,2) = -i\iint d(3)d(4)G(1,3)\Gamma(3,4;2)G(4,1^+), \tag{1.75}$$

$$\Gamma(1,2;3) = \delta(1,2)\delta(1,3) + \iiiint d(4)d(5)d(6)d(7)\frac{\delta\Sigma(1,2)}{\delta G(4,5)}G(4,6)\Gamma(6,7;3)G(7,5), \tag{1.76}$$

In Hedin's equations, the self-energy Σ is related to the quantities $\mathrm{G_0}$, G, P, W and Γ through a set of complicated coupled integral-differential equations. In principle, if Hedin's equations could be solved exactly in a self-consistent way, then the exact one-particle excitation properties would be obtained. However, this is generally not possible in practice, so that one has to resort to approximations.

From Hedin's equations, Hedin further proved that the vertex function Γ, thus also the irreducible polarizability P and the self-energy Σ, can be expanded as an infinite series in terms of two fundamental quantities only, the one-particle Green's function G and the screened Coulomb interaction W [44]. In evaluating the self-energy, the usage of W rather than the bare Coulomb interaction v is well motivated: on the one hand, in traditional MBPT where v is used as a fundamental quantity, there are various convergence problems in the density range of normal metals and semiconductors [41, 44, 81, 82]; on the other hand, Coulomb interactions in a real many-body system are largely screened, therefore W is much smaller than v and should behave consequently much better. For the self-energy Σ, the lowest order in W gives rise to one of its most popular approximations, known as the GW approximation. The GW approximation is obtained by approximating the vertex function Γ in its zeroth-order form as:

$$\Gamma(1,2;3) = \delta(1,2)\delta(1,3). \tag{1.77}$$

Substituting the above equation into Hedin's equations, we get the following set of self-consistent equations for the GW approximation:

$$\Sigma(1,2) = iG(1,2)W(1^+,2), \tag{1.78}$$

$$G(1,2) = G_0(1,2) + \iint d(3)d(4)G_0(1,3)\Sigma(3,4)G(4,2), \tag{1.79}$$

$$P(1,2) = -iG(1,2)G(2,1). \tag{1.80}$$

$$W(1,2) = v(1,2) + \iint d(3)d(4)v(1,3)P(3,4)W(4,2), \tag{1.81}$$

Within the GW approximation, the self-energy Σ assumes a very simple form as the product of the Green's function G and the screened Coulomb interaction W. According to Eq. (1.62), the screened interaction W can alternatively be expressed in terms of the reducible polarizability operator Π:

$$W(1,2) = v(1,2) + \iint d(3)d(4)v(1,3)\Pi(3,4)v(4,2), \tag{1.82}$$

From Eq. (1.57), the reducible polarizability Π is related to the irreducible one as:

$$\Pi(1,2) = \int d(3)P(1,3)(\hat{1} - vP)^{-1}(3,2). \tag{1.83}$$

The screened Coulomb interaction W can be separated as the sum of the bare Coulomb potential v and a correlation part $\mathrm{W_c}$ defined as:

$$W_c(1,2) = \iint d(3)d(4)v(1,3)\Pi(3,4)v(4,2). \tag{1.84}$$

Consequently, within the GW approximation, the exchange part of the self-energy Σ_x reads:

$$\Sigma_x(1,2) = iG(1,2)v(1^+,2), \tag{1.85}$$

and the correlation part Σ_c reads:

$$\Sigma_c(1,2) = iG(1,2)W_c(1^+,2) \tag{1.86}$$

The exchange part of the self-energy Σ_c in the frequency domain is energy-independent and has the form of the Hartree-Fock exchange operator:

$$\Sigma_x(\mathbf{r},\mathbf{r}') = -\sum_i^{occ} \frac{\psi_i(\mathbf{r})\psi_i^*(\mathbf{r}')}{|\mathbf{r}-\mathbf{r}'|}, \tag{1.87}$$

where the summation is over the quasiparticle amplitudes of occupied hole states. The evaluation of the correlation part Σ_c is the most computationally expensive part in GW calculations.

1.2.4 The $\mathrm{G^0W^0}$ Approximation and Beyond

The GW approximation provides a simple approximate form for the self-energy Σ. However, the set of equations Eqs. (1.78)-(1.81) for the GW approximation are numerically difficult to solve in a fully self-consistent manner. In practical GW calculations, a next level approximation that is commonly used is the $\mathrm{G^0W^0}$ approximation [83]. Within the $\mathrm{G^0W^0}$ approximation, the starting point is the evaluation of the non-interacting one-particle Green's function $\mathrm{G^0}$ by using the eigenenergies and the orbitals of a model system with a real one-particle Hamiltonian (which is energy-independent).

Here we consider the most popular model Hamiltonian of choice, the Kohn-Sham Hamiltonian. The self-energy in the frequency domain $\Sigma(\mathbf{r}, \mathbf{r}'; \omega)$ is hence calculated in a single iteration by the following equations:

$$G^0(\mathbf{r}, \mathbf{r}'; \omega) = \sum_v \frac{\psi_v^{KS}(\mathbf{r})\psi_v^{KS*}(\mathbf{r}')}{\omega - \epsilon_v^{KS} - i\eta} + \sum_c \frac{\psi_c^{KS}(\mathbf{r})\psi_c^{KS*}(\mathbf{r}')}{\omega - \epsilon_c^{KS} + i\eta}, \tag{1.88}$$

$$P^0(\mathbf{r}, \mathbf{r}'; \omega) = -\frac{i}{2\pi} \int d\omega' G^0(\mathbf{r}, \mathbf{r}'; \omega') G^0(\mathbf{r}, \mathbf{r}'; \omega - \omega'), \tag{1.89}$$

$$\Pi^0(\mathbf{r}, \mathbf{r}'; \omega) = \int d\mathbf{r}'' P^0(\mathbf{r}, \mathbf{r}''; \omega)(\hat{1} - vP^0)^{-1}(\mathbf{r}'', \mathbf{r}'; \omega), \tag{1.90}$$

$$W^0(\mathbf{r}, \mathbf{r}'; \omega) = v(\mathbf{r} - \mathbf{r}') + \iint d\mathbf{r}'' d\mathbf{r}''' v(\mathbf{r} - \mathbf{r}'')\Pi^0(\mathbf{r}'', \mathbf{r}'''; \omega)v(\mathbf{r}''', \mathbf{r}'; \omega), \tag{1.91}$$

$$\Sigma_{G^0W^0}(\mathbf{r}, \mathbf{r}'; \omega) = \frac{i}{2\pi} \int d\omega' G^0(\mathbf{r}, \mathbf{r}'; \omega + \omega') W^0(\mathbf{r}, \mathbf{r}'; \omega') e^{i\omega'\eta}, \tag{1.92}$$

where we have indicated explicitly Kohn-Sham energies and orbitals with "KS" in the superscript, and have used "v" and "c" in the subscript to represent the quantities corresponding to Kohn-Sham occupied (valence) and empty (conduction) states respectively. In Eq. (1.89), the irreducible polarizability P^0 is calculated in the random-phase approximation (RPA).

The quasiparticle energy ϵ_{i} is obtained from a first-order perturbation correction to the Kohn-Sham energy $\epsilon_{\mathrm{i}}^{\mathrm{KS}}$:

$$\epsilon_i \simeq \epsilon_i^{KS} + \langle \psi_i^{KS} | \Sigma_{G^0W^0}(\epsilon_i) \psi_i^{KS} \rangle - \langle \psi_i^{KS} | V_{xc} | \psi_i^{KS} \rangle, \tag{1.93}$$

where $\mathrm{V_{xc}}$ is the Kohn-Sham exchange-correlation potential used as a zeroth-order approximation to the self-energy $\Sigma_{\mathrm{G^0W^0}}$. Eq. (1.93) is a non-linear equation that can be solved iteratively, since the value of ϵ_{i} depends on itself through the energy-dependent self-energy on the right hand side of the equation. The perturbative evaluation of quasiparticle energies is based on two observations: on the one hand, the form of the quasiparticle equation Eq. (1.52) is similar to that of the Kohn-Sham equation Eq. (1.15), with the only difference that in Eq. (1.15) the self-energy Σ is replaced with the exchange-correlation potential $\mathrm{V_{xc}}$; on the other hand, for systems where they are known, quasiparticle amplitudes are found to be close to Kohn-Sham orbitals [84]. The approximation used in Eq. (1.93) is actually a diagonal approximation, since only the diagonal matrix elements of the self-energy are considered. One can also calculate the off-diagonal matrix elements of the self-energy with respect to the Kohn-Sham states. However, since this usually involves the evaluation of a large number of matrix elements resulting from the consideration of a not-so-small number of Kohn-Sham empty states, performing such calculations could be expensive, especially for large systems.

Even at the very first iteration, the $\mathrm{G^0W^0}$ approximation has been shown to be very successful in many cases for describing electronic excitations [73, 76, 77]. One success is that the calculated fundamental band gaps of semiconductors and insulators are often in good agreement with experiment. In Fig. [1.4], the calculated fundamental band gaps of the same sp semiconductors as in Fig.

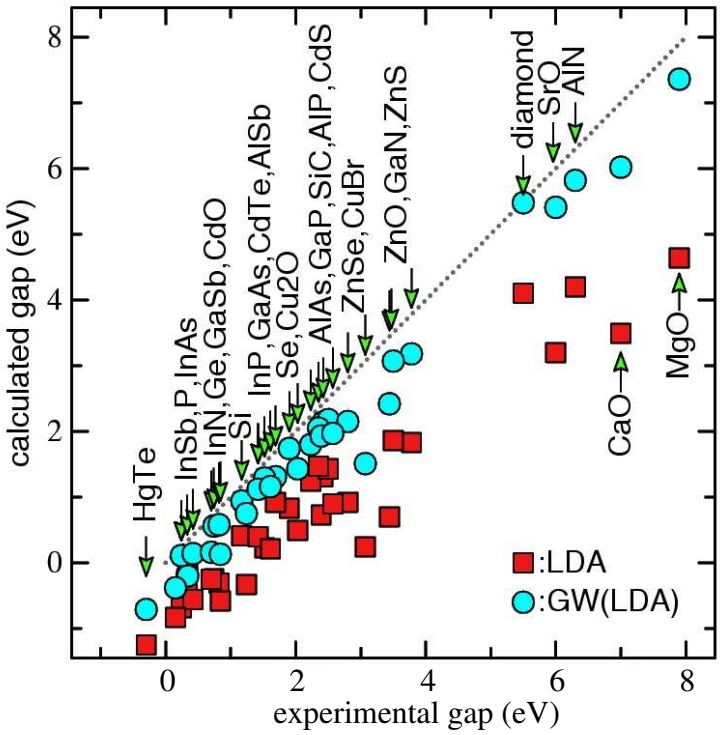

Figure 1.4: Comparison between the fundamental band gaps calculated from DFT-LDA (squares, left scale), calculated from GW at the G^0W^0 level (circles, left scale), and from experiment (bottom scale) for some sp semiconductors. This figure is taken from Ref. [74]

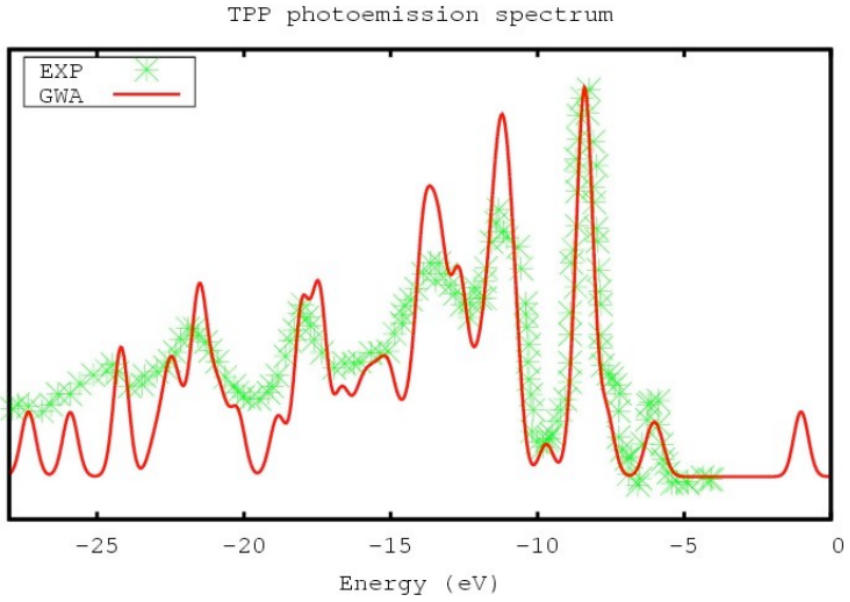

Figure 1.5: Comparison between the calculated GW electronic density of states at the G^0W^0 level and the photoemission spectrum from a direct photoemission measurement for the free-base tetraphenylporphyrin molecule ($TPPH_2$) ($C_{44}H_{30}N_4$). A Gaussian broadening of 0.25 eV is for the theoretical curve. See Ref. [48] for more details.

[1.2] are compared again with experiments, including the results of G^0W^0 calculations. Clearly the G^0W^0 results improve systematically the DFT-LDA ones and mostly agree well with experiments. Another success is that the G^0W^0 approximation can predict accurately also the quasiparticle energies away from the ionization edges. In Fig. [1.5], the theoretical DOS calculated from G^0W^0 is compared with the experimental photoemission spectrum from direct photoemission measurement for the free-base tetraphenylporphyrin molecule ($TPPH_2$). At variance with the DFT-LDA DOS spectrum displayed in Fig. [1.3], the G^0W^0 one is in good agreement with the direct photoemission spectrum concerning the positions of the peaks. Since oscillator strength effects are not considered in the G^0W^0 calculation, the relative intensities of the peaks need not to be compared with experiment.

One important drawback of the G^0W^0 approximation is that due to its non self-consistent nature, the calculated quasiparticle energies depend on the starting model Hamiltonian, such that some ambiguities are involved in them. To go beyond the G^0W^0 approximation, one may first consider the issue of self-consistency within the GW approximation [73, 76, 77]. For instance, if the screened Coulomb interaction W_0 is fixed at the RPA level, while the Green's function G is updated at each iteration, thus achieving partial self-consistency in G, the GW^0 approximation would be obtained. In a similar way, one may obtain other partially self-consistent levels of theory by keeping certain quantities fixed while updating others. If all related quantities are updated at each iteration, full self-consistency of the GW calculation can be obtained, the results of which would not depend on the starting point of the calculation. Although partially and fully self-consistent GW calculations are more expensive than G^0W^0 ones, sometimes they yield worse results and it is not clear how good they are in general [85, 86]. For example, fully self-consistent GW calculations are found to be systematically worse than G^0W^0 ones in describing quasiparticles and plasmon satellites [87–90]. However, in the meanwhile, some successes do exist. A main outcome is that the total energy of the homogeneous electron gas given by fully self-consistent GW calculations is in strikingly close agreement with quantum Monte-Carlo results [91–93]. Moreover, GW^0 calculations are found to improve the positions of plasmon satellites [94].

To proceed even further to go beyond the GW approximation, one has to resort to corrections to the approximate vertex function given in Eq. (1.77) [73, 76, 77]. Vertex corrections are often found to cancel the effects of the deterioration in the description of electronic excitations in fully self-consistent GW calculations compared with that in G^0W^0 calculations. Vertex corrections may be used to describe the multipole plasmon satellites observed in the alkali metals, for which only a one-plasmon picture can be described in the GW approximation [95].

In this work, we employ the diagonal G^0W^0 scheme within the GW approximation to study the electronic excitation properties of neutral gold clusters. Our implementation of the GW method is described in the next chapter.

Chapter 2

Methodological Details of GW

In this chapter, we present the methodological details of our implementation of the GW method used within this work. We consider not only some general aspects in the implementation of GW, but also two specific aspects relevant to our study of gold clusters.

2.1 Numerical Implementation of GW

In this section, we discuss our numerical implementation of the GW method, which is based on the G^0W^0 approximation. First we present a brief overview of current schemes for the implementation of GW. After that, we describe in detail our schemes for solving two main computational challenges involved in traditional GW calculations. To illustrate the efficiency and the correctness of our schemes, we give an example of the electronic structure of the caffeine molecule.

2.1.1 Overview of Current Implementation

There are various schemes currently available for the implementation of the GW method based on the G^0W^0 approximation. We review them briefly considering three aspects: the calculation of the screened Coulomb interaction W, the basis for representing molecular orbitals, charge-density, and the polarizability operators P and Π, and the sums over empty states in the calculation of the irreducible polarizability P and the self-energy Σ.

Calculation of the Screened Coulomb Interaction W

Due to the pole structures on the frequency axis of the irreducible polarizability P involved in the calculation of the screened Coulomb interaction W (see Eq. (1.88) and Eq. (1.89)), in GW calculations, W has to be calculated on very fine energy grids in order to converge the calculated self-energies. This makes the calculation of W very expensive.

Among the several schemes available for the treatment of W, the most direct one has been to calculate all related quantities on the real frequency axis, without making any further approximation for W. However, this is computationally very expensive and can not be applied conveniently to the study of large molecular systems.

One popular approximated scheme is to use a plasmon-pole model for the energy dependence of W [96–98]. This is based on the observation that, on the one hand, the evaluation of the self-energy Σ within the GW approximation depends on the convolution of the Green's function G and the screened Coulomb interaction W over the energy (see Eq. (1.92)), thus should not be sensitive to the fine details of the energy dependence of W, and on the other hand, it is known that the imaginary part of W is dominated by a strong peak which corresponds to a plasmon excitation. The usage of a plasmon-pole approximation can reduce a lot the computational effort, but there are some drawbacks. One is that it has limited accuracy if applied to systems other than sp bonded ones. And another is that the quasiparticle lifetime can not be calculated by using it.

Enlightened by the GW space-time method [99, 100], instead of working on the real axis, one can express and calculate all the quantities, including W, on the imaginary axis. This makes the calculated quantities smooth in the imaginary frequency domain, or exponentially decaying in the imaginary time domain, resulting in a much reduced computational effort. After the expectation value of the correlation part of the self-energy is obtained on the imaginary frequency axis, it can be fitted to a multipole form:

$$\langle\psi_n|\Sigma_c(i\omega)|\psi_n\rangle = a_n^0 + \sum_i \frac{a_n^i}{i\omega - b_n^i}, \tag{2.1}$$

and analytically continued to the real frequency axis. Here $|\psi_{\rm n}\rangle$ represents a one-particle state such as a Kohn-Sham state, and $\rm a_n^i$ and $\rm b_n^i$ are complex fitting parameters. The parameter $\rm a_n^0$ should be zero in principle, but it has been proved helpful if a finite value for it is allowed. While very little accuracy may be lost in the analytic continuation procedure, the computational cost is much reduced and it is no longer necessary to use a plasmon-pole approximation in the calculation of W. Instead of using a multipole form, one can use a Páde approximant form [101] for the fitting of $\langle\Sigma_{\rm c}({\rm i}\omega)\rangle_{\rm n}$, with which one can also find good accuracy and stability in the calculated quasiparticle energies. Optionally, one may choose to form the correlation part of the self-energy directly on the real frequency axis by using a contour integration technique, which takes use of the value of W on both the real and the imaginary frequency axis [102]. By doing so, one can obtain even more accurate and stable results for the calculated quasiparticle energies, but at the cost of being computationally more expensive. In this work, we perform all the GW calculations by using the analytic continuation of the self-energy based on the multipole form Eq. (2.1).

Basis for molecular orbitals, charge-density, and the polarizability operators

In conjunction with pseudopotentials, plane-wave basis sets are widely used for representing molecular orbitals and electronic charge-density in DFT-based first principles electronic structure calculations. Naturally, the plane-wave basis is a most common choice used in GW calculations. The usage of plane-waves has several advantages. For instance, the product of molecular orbitals can be evaluated straightforwardly, and the convergence of the calculated results with respect to the basis size can be controlled easily.

One main computational challenge in GW calculations is the representation of the polarizability operators P and Π. In RPA, by assuming time-reversal invariance of the Kohn-Sham Hamiltonian and work with real Kohn-Sham orbitals, the irreducible polarizability P^0 in imaginary frequency is calculated as:

$$P^0(\mathbf{r}, \mathbf{r}'; i\omega) = -4\Re \sum_{vc} \frac{\psi_v(\mathbf{r})\psi_c(\mathbf{r})\psi_v(\mathbf{r}')\psi_c(\mathbf{r}')}{\epsilon_c - \epsilon_v + i\omega}. \tag{2.2}$$

As indicated in the above equation, P^0 is a non-local operator that depends on the product of the Kohn-Shan valence (occupied) and conduction (empty) orbitals. To represent P^0, essentially what one needs to do is simply to represent the pairs of the product of valence and conduction orbitals. As a result, in the traditional implementation of the GW method, plane-waves are usually used, not only for representing molecular orbitals, also for representing P^0. Since the calculation of P^0 in principle involves an infinite number of pairs of valence and conduction states resulting from the infinite summation over conduction states, a large number of basis functions are usually needed and it is computationally prohibitive for large systems.

Furthermore, since according to Eq. (1.82), the reducible polarizability Π^0 has a simple relation with the irreducible one as:

$$\Pi^0(\mathbf{r}, \mathbf{r}'; i\omega) = P^0 + P^0 \cdot v \cdot P^0 + P^0 \cdot v \cdot P^0 \cdot v \cdot P^0 + \cdots, \tag{2.3}$$

where a single dot indicates the product of two quantities, such as:

$$(P^0 \cdot v)(\mathbf{r}, \mathbf{r}'; \omega) = \int d\mathbf{r}'' P^0(\mathbf{r}, \mathbf{r}''; \omega) v(\mathbf{r}'', \mathbf{r}'), \tag{2.4}$$

the same basis for representing P^0 can also be used for representing Π^0, and the plane-wave representation of Π^0 is also very expensive.

According to recent work, it is possible to construct an optimal basis set which is small yet with controllable accuracy for the representation of the polarizability operators [48, 103]. The usage of the optimal basis set results in small polarizability matrices that are much easier to operate numerically. A scheme for constructing such an optimal basis set is applied in the study of this work, and is described in detail in the next subsection.

Sums Over Empty States

The difficulty in the treatment of the sums over empty states in the calculation of the irreducible polarizability P and the self-energy Σ is another main computational challenge in GW calculations. The need to consider the summation over empty states for P is evident as indicated in Eq. (2.2), and this need for Σ within the GW approximation comes partly from the evaluation of the Green's function G (see Eq. (1.88)), and partly from the evaluation of the screened Coulomb interaction W, which depends on P through Eq. (1.91) and Eq. (1.90).

A direct approach to deal with the sums over empty states is to include a finite number of empty states in the calculation of P and Σ [47]. The problem with this treatment is that the convergence of the calculated quasiparticle energies with respect to the number of empty states used can be extremely slow. In fact, well converged results may be obtained only for very small systems.

Approximated schemes have been developed to solve the slow convergence problem. In one scheme, those empty states not explicitly considered in the calculation of the irreducible polarizability and the correlation part of the self-energy are taken into account by using an effective energy, which is determined by imposing a sum rule for the first moment of the dielectric function. As a consequence, there is a large reduction of the number of empty states needed to reach good convergence in the calculated results [104]. In another scheme, an effective energy is used in the calculation of the correlation part of the self-energy to account for the contribution from all the empty states. This effective energy can be expanded exactly in an infinite perturbative series, but it is truncated in practice. In such a way, no empty states have to be considered at all [105]. These two schemes are efficient, but they both have the problem that some accuracy may be lost due to the approximations used.

Recently, it has been proposed that it is possible to avoid the explicit consideration of any empty state without making compromise on the accuracy of the calculated results. In one scheme, an iterative solver is used in the calculation of P and Σ based on the Sternheimer approach [48]. In another scheme, the screened Coulomb interaction W is obtained by solving a self-consistent Sternheimer equation, and the Green's function G is evaluated by using an approach similar to the Sternheimer approach for W [101]. These two schemes are both accurate and efficient. The previous scheme is applied in the study of this work, and is presented in detail in the next subsection.

2.1.2 Solutions to the Computational Challenges

As mentioned previously, two main computational challenges exist in traditional GW calculations, especially in those calculations for large systems. One is that one needs to calculate and manipulate large matrices for representing the polarizability operators P and Π. Another is that in the calculation of the irreducible polarizability P and the self-energy Σ, the sums over empty states are usually very slowly convergent. Because of these two challenges, the routine application of the GW method in the

past has been limited to the scope of a few handfuls of inequivalent atoms, at most. In this subsection, we focus on the solutions for solving these two challenges, which are used in our implementation of the GW method in this work.

In the following, we briefly describe the above-mentioned two computational challenges, and demonstrate that, indeed they can be solved by employing recently introduced algorithms, which are the construction of the optimal basis for representing the polarizability operators P and Π [47, 48], and the Lanczos chain technique for the calculation of the irreducible polarizability P and the self-energy Σ [48].

The Optimal Polarizability Basis

The difficulty in representing the polarizability operators can be solved by constructing and employing an optimally small set of basis functions for the representation of the polarizability operators [47, 48].

Suppose an optimally small and energy independent basis set $\{\Phi_\mu(\mathbf{r})\}$ can be found for representing P^0:

$$P^0(\mathbf{r},\mathbf{r}';i\omega) \simeq \sum_{\mu\nu} \Phi_\mu(\mathbf{r}) P^0_{\mu\nu}(i\omega) \Phi_\nu(\mathbf{r}'), \tag{2.5}$$

where $\mathrm{P}^0_{\mu\nu}(\mathrm{i}\omega)$ is the matrix representation of P^0. Then, according to Eq. (2.3):

$$\Pi^0(\mathbf{r},\mathbf{r}';i\omega) \simeq \sum_{\mu\nu} \Phi_\mu(\mathbf{r}) \Pi^0_{\mu\nu}(i\omega) \Phi_\nu(\mathbf{r}'), \tag{2.6}$$

where $\Pi^0_{\mu\nu}(\mathrm{i}\omega)$ is the matrix representation of Π^0. Furthermore, since the correlation part of the screened Coulomb interaction W^0_c reads:

$$W^0_c(\mathbf{r},\mathbf{r}';i\omega) = v \cdot \Pi^0 \cdot v, \tag{2.7}$$

by using the same basis set, it can also be expressed in a simple form as:

$$W^0_c(\mathbf{r},\mathbf{r}';i\omega) \simeq \sum_{\mu\nu} (v\cdot\Phi_\mu)(\mathbf{r}) \Pi^0_{\mu\nu}(i\omega) (v\cdot\Phi_\nu)(\mathbf{r}'). \tag{2.8}$$

From Eq. (2.5), (2.6), (2.8), we see that if an optimally small and accurate basis set for the representation of the polarizability operators is found, then a high computational speed up can be achieved. We call such a basis set the optimal polarizability basis.

To build the optimal polarizability basis, without losing generality, we consider the irreducible polarizability at zero time:

$$\tilde{P^0}(\mathbf{r},\mathbf{r}';\tau=0) = \sum_{vc} \psi_v(\mathbf{r})\psi_c(\mathbf{r})\psi_v(\mathbf{r}')\psi_c(\mathbf{r}'). \tag{2.9}$$

Several possibilities are explored in the following.

By introducing the projector operator over the valence (hole) states $\hat{\mathrm{Q}}_\mathrm{h}$ and the one over the conduction (electron) states $\hat{\mathrm{Q}}_\mathrm{e}$, and noting that

$$\hat{Q}_e = \hat{1} - \hat{Q}_h, \tag{2.10}$$

Eq. (2.9) can be written as:

$$\begin{aligned}\tilde{P^0}(\mathbf{r},\mathbf{r}';\tau=0) &= Q_h(\mathbf{r},\mathbf{r}')Q_e(\mathbf{r},\mathbf{r}') \\ &= Q_h(\mathbf{r},\mathbf{r}')[\delta(\mathbf{r},\mathbf{r}')-Q_e(\mathbf{r},\mathbf{r}')].\end{aligned} \tag{2.11}$$

Taking use of the above equation and solve the eigenvalue problem:

$$\tilde{P^0}(\tau=0)|\Phi_\mu\rangle = q_\mu|\Phi_\mu\rangle, \tag{2.12}$$

we can obtain a polarizability basis by taking the eigenvectors that correspond to the most important eigenvalues. Here the explicit consideration of the conduction states is avoided. However, since one has to use a not-so-small number of basis functions in order to achieve a satisfactory accuracy in the calculated quasiparticle energies, the calculations by using this kind of basis set may be expensive.

A better way would be to consider a modified polarizability operator $\tilde{\mathrm{P}^0}'$, for which the number of conduction states in Eq. (2.9) is defined by states with energy ϵ_c smaller than a given cutoff $\mathrm{E_C}$. By solving a similar eigenvalue problem as in Eq. (2.12) for $\tilde{\mathrm{P}^0}'$, an optimal polarizability basis can be constructed [47]. However, this involves the explicit calculation of a possibly large number of conduction states, and is thus not computationally favorable.

To avoid the consideration of conduction states, we replace the $\hat{\mathrm{Q}}_\mathrm{e}$ operator in Eq. (2.11) with a projector operator over the space spanned by plane-waves which have a kinetic energy smaller than an E^* cutoff, are first orthogonalized to all the valence states and then orthonormalized:

$$\hat{Q}_e^* = \sum_{\frac{1}{2}|\mathbf{G}|^2,\frac{1}{2}|\mathbf{G}'|^2\leq E^*} |\bar{\mathbf{G}}\rangle\langle\bar{\mathbf{G}}'|, \tag{2.13}$$

To be more specific, the orthogonalized plane-waves in $\{|\bar{\mathbf{G}}\rangle\}$ is first calculated from a set of plane-waves $\{|\mathbf{G}\rangle\}$ defined by E^*:

$$|\bar{\mathbf{G}}\rangle = \hat{Q}_e|\mathbf{G}\rangle, \tag{2.14}$$

and are then orthonormalized. An optimal polarizability basis can be constructed by solving:

$$\sum_v \psi_v(\mathbf{r})\langle\mathbf{r}|\hat{Q}_e^*|\psi_v\Phi_\mu\rangle = q_\mu|\Phi_\mu(\mathbf{r})\rangle, \tag{2.15}$$

and taking the eigenvectors with eigenvalues larger than a given threshold q^* [48]. Here the space representation of the vector $|\psi_\mathrm{v}\Phi_\mu\rangle$ reads:

$$\langle\mathbf{r}|\psi_v\Phi_\mu\rangle = \psi_v(\mathbf{r})\Phi_\mu(\mathbf{r}). \tag{2.16}$$

In this way, good accuracy can be achieved with only a relatively small number of basis functions used. Note that the accuracy of this scheme can be systematically improved by adjusting the values of the E^* and q^* parameters.

This scheme has been implemented for norm-conserving pseudopotentials in the GWL module [46] of the plane-waves and pseudopotentials based Quantum Espresso (QE) density-functional package [45], and has been used in our study of gold clusters.

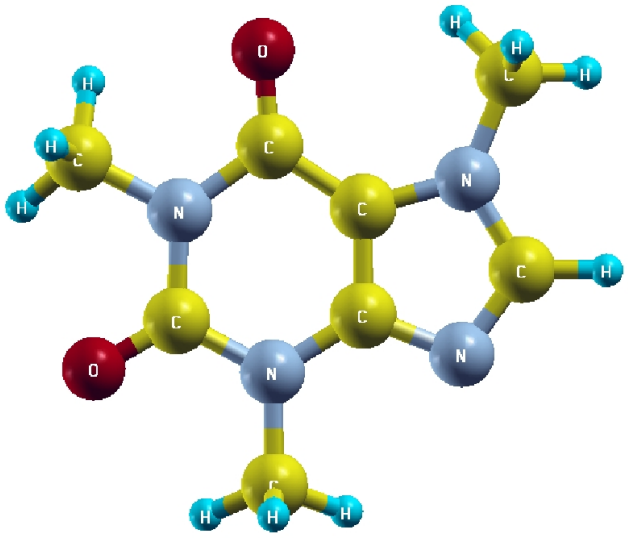

Figure 2.1: Structure of the caffeine molecule $C_8N_4O_2H_{10}$.

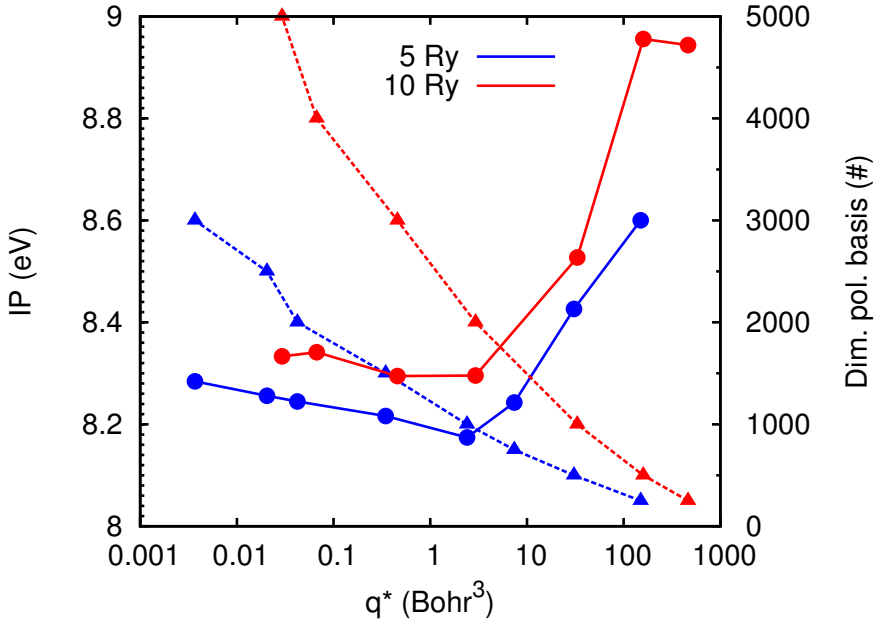

Figure 2.2: Calculated vertical ionization potential of the caffeine molecule (discs, left scale) and dimension of the polarizability basis (triangles, right scale) as a function of the q^* threshold. The polarizability basis has been constructed with $E^* = 5$ Ry (blue) and $E^* = 10$ Ry (red). The lines are a guide to the eye.

To illustrate this scheme, we consider an example of the isolated caffeine molecule [106], whose structure is drawn in Fig. [2.1]. The caffeine molecule under investigation is at the theoretically optimized geometry with bond lengths that have an average deviation of $< \%1$ and a maximum deviation of $< \%3$ from experiment. All the GW calculations of the caffeine molecule in this chapter were performed in a cubic supercell that has an edge of 25 Bohr, by using the H.pz-vbc.UPF, C.pz-vbc.UPF, N.pz-vbc.UPF and O.pz-mt.UPF pseudopotentials from the QE distribution, and a kinetic energy cutoff of 60 Ry and 240 Ry respectively for plane-waves representing molecular orbitals and charge-density. The (vertical) IPs in Fig. [2.2] were calculated by using the optimal polarizability basis constructed under the current scheme, with a dimension controlled by the E^* and q^* parameters, and also by using the Lanczos chain technique that is described later, with a number of 20 Lanczos steps for the calculation of the irreducible polarizability P and the self-energy Σ. As it can been seen, the two set of calculations with $\mathrm{E}^* = 5\ \mathrm{Ry}$ and $\mathrm{E}^* = 10\ \mathrm{Ry}$ both reach the same value of IP within a few tens of eV, which is close to the experimental value of 8.25 eV [107]. For both values of E^*, good convergence within $\sim 0.15\ \mathrm{eV}$ can be achieved with a value of $\mathrm{q}^* \sim 10\ \mathrm{Bohr}^3$, corresponding to a small polarizability basis with only ~ 500 and ~ 1000 basis functions respectively. Note that 0.15 eV is just our estimated accuracy due to the analytic continuation procedure. Indeed this scheme is accurate on the one hand, and computationally efficient on the other hand.

The Lanczos Chains

Another difficulty involved in traditional GW calculations is the slow convergence of the calculated quasiparticle energies with respect to the sums over empty states in the calculation of the irreducible polarizability P and the self-energy Σ.

To have an idea of how slow the convergence can be, we consider again the example of the caffeine molecule [106]. In Fig. [2.3], we report with dots the GW (vertical) IPs of the caffeine molecule calculated by using the method of Ref. [47], with inclusion a finite number of empty states in the calculation of P and Σ. It is obvious that the convergence of the sums over empty states is extremely slow and well converged result seems impossible to reach. In order to obtain the converged result, we fit the data displayed as diamonds to a simple formula $\mathrm{IP}(\mathrm{E_C}) = \mathrm{IP}_\infty - \beta/\mathrm{E_C}$. By doing this, an extrapolated IP of 8.02 eV is obtained, and is in good agreement with the experimental value of 8.25 eV [107]. Such an extrapolation method based on experience works, but is very inconvenient. Since this method requires the performance of several sets of GW calculations with inclusion of different number of empty states, it can be computationally very expensive especially for large systems. By employing the Lanczos chain technique that is described later, the slow convergence problem can be successfully solved, in that it is no longer necessary to consider the sums over empty states [48].

Now suppose an optimal polarizability basis $\{\Phi_\mu(\mathbf{r})\}$ has already been constructed. In terms of

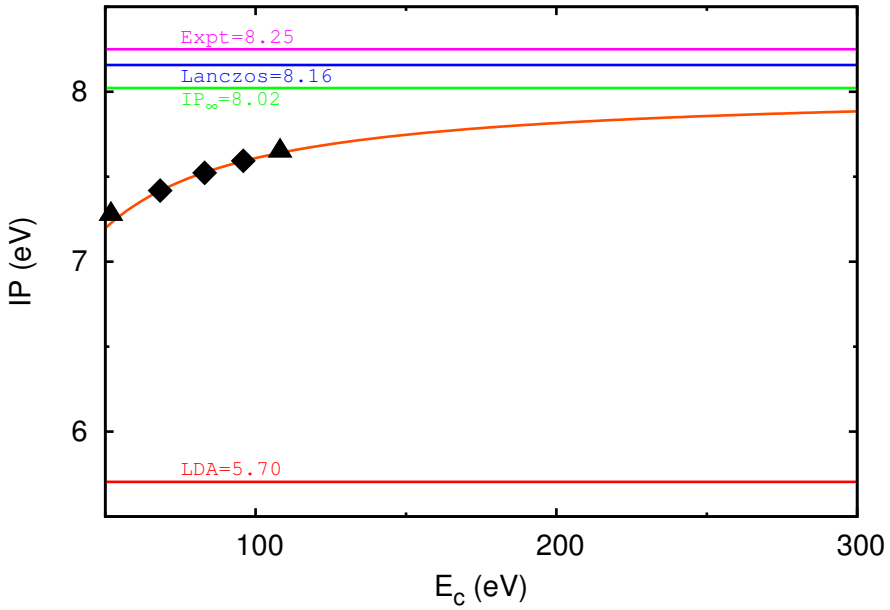

Figure 2.3: Calculated vertical ionization potential of the caffeine molecule and comparison with experiment (magenta line) [107]. The black dots correspond to GW results obtained by including 2000, 3000, 4000, 5000 and 6000 empty states respectively in the calculation of the irreducible polarizability P and the self-energy Σ, where the number of empty states included is controlled by the E_C cutoff. The data indicated by diamonds have been fitted accurately to a simple formula $IP(E_C) = IP_\infty - \beta/E_C$, resulting in a fit given by the orange line and an extrapolated IP given by the green line. The red line is the calculated IP from the DFT-LDA HOMO energy level. The blue line represents the GW IP calculated by using the Lanczos chain technique with 20 Lanczos steps for P and Σ, and an optimal polarizability basis of 750 functions constructed by using the previously described algorithm with $q^* = 7.38$ Bohr^3 and $E^* = 5$ Ry.

$\{\Phi_\mu(\mathbf{r})\}$ and taking use of Eq. (2.3) and Eq. (2.5), the polarizability matrix $\mathrm{P}^0_{\mu\nu}(\mathrm{i}\omega)$ reads:

$$P^0_{\mu\nu}(i\omega) = -4\Re\sum_{vc}\frac{\int d\mathbf{r}d\mathbf{r}'\Phi_\mu(\mathbf{r})\psi_v(\mathbf{r})\psi_c(\mathbf{r})\psi_v(\mathbf{r}')\psi_c(\mathbf{r}')\Phi_\nu(\mathbf{r}')}{\epsilon_c-\epsilon_v+i\omega}. \tag{2.17}$$

Using the projector operator over the empty (electron) states $\hat{\mathrm{Q}}_\mathrm{e}$, the above equation can be written as:

$$P^0_{\mu\nu}(i\omega) = -4\Re\sum_v\langle\psi_v\Phi_\mu|\hat{Q}_e(H^0-\epsilon_v+i\omega)^{-1}\hat{Q}_e|\psi_v\Phi_\nu\rangle, \tag{2.18}$$

where H^0 is the Kohn-Sham Hamiltonian. Here the summation over empty states can be eliminated with the help of Eq. (2.10). However, a direct approach to the above equation requires the application of $(\mathrm{H}^0-\epsilon_\mathrm{v}+\mathrm{i}\omega)^{-1}$ to a large number of $\mathrm{N_v}\times\mathrm{N_P}$ vectors at every imaginary frequency $\mathrm{i}\omega$, where $\mathrm{N_v}$ is the number of valences states and $\mathrm{N_P}$ is the dimension of the optimal polarizability basis, and is thus computationally inconvenient.

The computational cost can be substantially reduced by proceeding in the following steps [48]:

First, we build an optimal basis set $\{\mathrm{t}^0_\alpha(\mathbf{r})\}$ for representing the $\mathrm{N_v}\times\mathrm{N_P}$ vectors $\{\hat{\mathrm{Q}}_\mathrm{e}|\psi_\mathrm{v}\Phi_\mu\rangle\}$:

$$\langle\mathbf{r}|\hat{Q}_e|\psi_v\Phi_\mu\rangle \simeq \sum_{\alpha=1}^{N_T} t^0_\alpha(\mathbf{r})T_{\alpha,v\mu}, \tag{2.19}$$

where

$$T_{\alpha,v\mu} = \langle t^0_\alpha|\hat{Q}_e|\psi_v\Phi_\mu\rangle, \tag{2.20}$$

and $\mathrm{N_T}$ is the number of basis functions in $\{\mathrm{t}^0_\alpha(\mathbf{r})\}$. By using Eq. (2.19), Eq. (2.18) reads:

$$P^0_{\mu\nu}(i\omega) \simeq -4\Re\sum_{v,\alpha\beta}\langle t^0_\alpha|(H^0-\epsilon_v+i\omega)^{-1}|t^0_\beta\rangle\times T_{\alpha,v\mu}T_{\beta,v\nu}. \tag{2.21}$$

Since the value of $\mathrm{N_T}$ can be made much smaller than that of $\mathrm{N_v}\times\mathrm{N_P}$, the number of basis functions to which the inverse shifted Hamiltonian has to be applied in Eq. (2.18) can be significantly reduced.

Instead of calculating the matrix elements in Eq. (2.18), the problem is now that of solving $\langle\mathrm{t}^0_\alpha|(\mathrm{H}^0-\epsilon_\mathrm{v}+\mathrm{i}\omega)^{-1}|\mathrm{t}^0_\beta\rangle$. To do this, we generate through a Lanczos chain algorithm [108] a set of orthonormal vectors $\{\mathrm{t}^\mathrm{i}_\alpha\}$ for each t^0_α, with which we have:

$$\langle t^0_\alpha|(H^0-\epsilon_v+i\omega)^{-1}|t^0_\beta\rangle = \sum_i\langle t^0_\alpha|t^i_\alpha\rangle\langle t^i_\alpha|(H^0-\epsilon_v+i\omega)^{-1}|t^0_\beta\rangle. \tag{2.22}$$

In the $\{\mathrm{t}^\mathrm{i}_\alpha\}$ basis, the Hamiltonian H^0 is tridiagonal and can be easily and rapidly inverted at every ϵ_v and at every $\mathrm{i}\omega$.

The above-described algorithm can be also used in the calculation of the self-energy Σ. Considering Eq. (2.6), by using the same basis set for the reducible polarizability Π as for the irreducible one P, we arrive at this equation for the expectation value of the correlation part of the self-energy:

$$\langle\Sigma_c(i\omega)\rangle_n = \frac{1}{2\pi}\sum_{\mu\nu}\int d\omega'\Pi_{\mu\nu}(i\omega')\times\langle\psi_n(v\Phi_\mu)|(H^0-i(\omega-\omega'))^{-1}|\psi_n(v\Phi_\nu)\rangle, \tag{2.23}$$

where the space representation of the vector $|\psi_{\rm n}({\rm v}\Phi_\mu)\rangle$ reads:

$$\langle \mathbf{r}|\psi_n(v\Phi_\mu)\rangle = \psi_n(\mathbf{r}) \int d\mathbf{r}' v(\mathbf{r},\mathbf{r}')\Phi_\mu(\mathbf{r}'). \tag{2.24}$$

Similarly as in the calculation of the irreducible polarizability matrix $\mathrm{P}^0_{\mu\nu}(\mathrm{i}\omega)$, an optimally small basis set $\{\mathrm{s}_\alpha(\mathbf{r})\}$ can be constructed for the representation of the $\{|\psi_{\rm n}({\rm v}\Phi_\mu)\rangle\}$ vectors:

$$\langle \mathbf{r}|\psi_n(v\Phi_\mu)\rangle \simeq \sum_{\alpha=1}^{N_s} s_\alpha(\mathbf{r}) S_{\alpha,n\mu}, \tag{2.25}$$

where

$$S_{\alpha,n\mu} = \langle s_\alpha|\psi_n(v\Phi_\mu)\rangle. \tag{2.26}$$

Then an equivalent Lanczos chain algorithm can be applied to each s_α and the matrix elements on the right hand side of Eq. (2.23) can be easily calculated.

This Lanczos chain technique for the evaluation of P and Σ has also been implemented in the GWL module [46] of the QE package [45], and is used in our study of gold clusters.

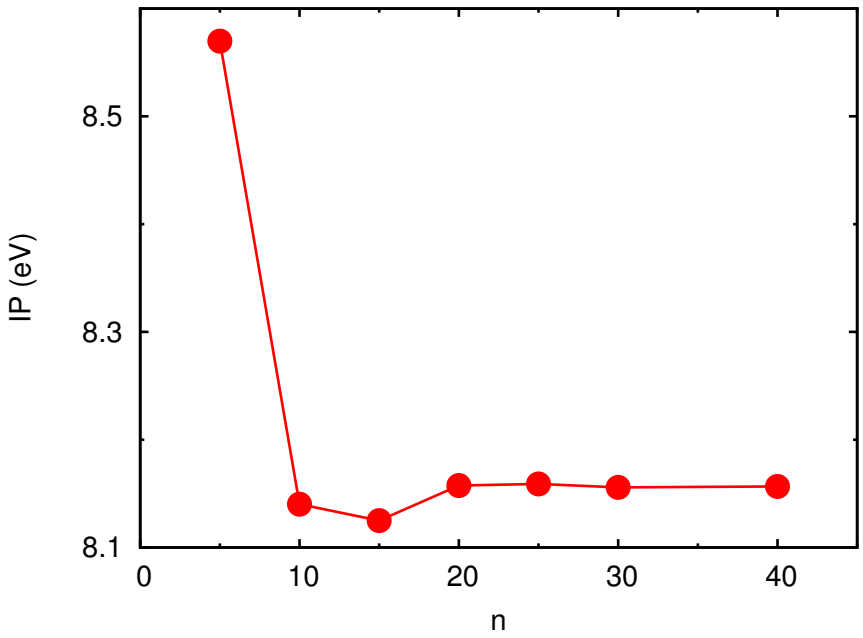

Figure 2.4: Convergence of the calculated vertical ionization potential of the caffeine molecule with respect to the number of Lanczos steps used in the Lanczos calculation of the irreducible polarizability P and the self-energy Σ. The optimal polarizability basis used here is the same as that is used in the Lanczos calculation reported in Fig. [2.3].

To illustrate this Lanczos chain technique, we come back to the example of the caffeine molecule. In Fig. [2.3], we compare the calculated (vertical) IPs of the caffeine molecule with experiment. The Lanczos result presented there was obtained by using 20 Lanczos steps respectively for P and Σ, and an optimal polarizability basis of 750 functions constructed by using the previously described

algorithm with $q^* = 7.38\ \mathrm{Bohr}^3$ and $E^* = 5\ \mathrm{Ry}$. As it can be seen, with a single calculation, which is more computationally efficient compared with the extrapolation method reported in the same figure, the Lanczos chain technique gives a calculated IP of 8.16 eV, in very good agreement with the experimental value of 8.25 eV. In Fig. [2.4], the dependence of the calculated GW IP as a function of the number of Lanczos steps used in the Lanczos calculation of P and Σ is displayed. The same optimal polarizability basis as used to obtain the Lanczos result reported in Fig. [2.3] was used to obtain those reported in Fig. [2.4]. The convergence of IP with respect to the number of Lanczos steps is obviously very fast. As a result, only a small number of Lanczos steps is needed in order to reach well converged results.

2.1.3 Example of the Electronic Density of States for Caffeine

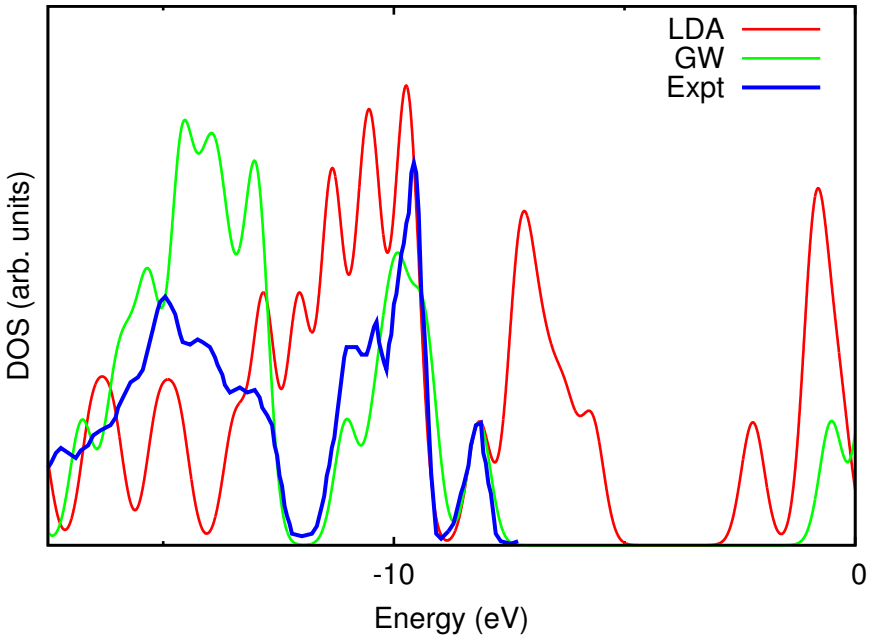

Figure 2.5: Calculated DFT-LDA and GW electronic densities of states for the caffeine molecule and comparison with the photoemission spectrum from direct photoemission measurement [107]. The GW results are from the same Lanczos calculation as reported in Fig. [2.4]. A Gaussian broadening of 0.25 eV has been used.

As a demonstration of the correctness of our schemes for solving the main computational challenges involved in traditional GW calculations in this work, we present in Fig. [2.5] for the caffeine molecule the comparison between the calculated electronic density of states (DOS) from DFT-LDA and GW calculations, and the photoemission spectrum from experiment [107]. As the experimental spectrum is from a direct photoemission measurement, only the part of the spectrum that corresponds to the valence states is available. While the positions of the peaks of the experimental spectrum can not be reproduced by LDA, they are very well predicted by GW. In addition, GW opens the quasi-

particle gap for the caffeine molecule, which is severely underestimated by LDA. Note also that as we do not consider any oscillator strength effects, the intensities of the peaks from theoretical calculations are not compared with experiment. In summary, we have justified here the correctness of our implementation of the GW method for solving the main computational challenges involved in traditional GW calculations.

2.2 Specific Considerations for Gold Clusters

In this section, we focus on two specific aspects concerning the GW calculations of gold clusters: the Au semicore 5s and 5p states and the open-shell character of some symmetric molecular structures. Their relevance to our study is discussed and our treatment for them is given.

2.2.1 Semicore States

The role that semicore states plays in GW calculations of systems containing metal elements was first reported by Rohlfing et al. for bulk CdS [109]. It was found that the problem of the bad quality of the calculated energy levels for states with Cd 4d feature comes mainly from the evaluation of the exchange term of the self-energy, and can be solved by including also the Cd semicore 4s and 4p states in addition to the Cd 4d and 5s states in the valence manifold of the Cd pseudopotential. Similar semicore effects have also been observed in the study of bulk GaN and Zn-based bulk systems such as ZnS and ZnO [110–113]. The semicore states are important in the GW calculations, not only of metal-based bulk systems, but also of finite systems containing metal elements [49], such as gold clusters.

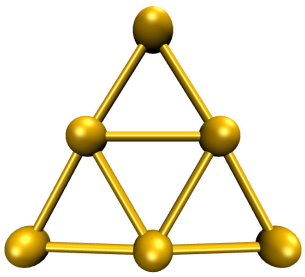

Figure 2.6: Lowest energy structure of the Au_6 cluster.

In order to illustrate the semicore effects, as a paradigmatic example of gold clusters, we consider a Au_6 structure depicted in Fig. [2.6] which possesses D_{3h} symmetry and is generally believed as the lowest energy structure of the neutral Au_6 cluster [24–31]. This structure was optimized with DFT-LDA forces by using the pseudopotential Au.pz-d-rrkjus.UPF which includes 5d and 6s as valence electrons from the QE distribution [45]. Two pseudopotentials for the gold atom were generated

and were the only ones used in the study of the quasiparticle spectra of gold clusters in this work. In the first pseudopotential, the Au 5d and 6s states are treated as the valence ones. We call this pseudopotential the no semicore pseudopotential. In the second pseudopotential, in addition to the Au 5d and 6s states, the Au semicore 5s and 5p states are also kept in the valence manifold. We refer to this pseudopotential as the semicore pseudopotential. The no semicore pseudopotential requires a plane-wave cutoff of 60 Ry to converge the calculated results, while in the case when the semicore pseudopotential is used, a cutoff as large as 120 Ry is needed. More details of the pseudopotentials used is presented in Chapter 3.

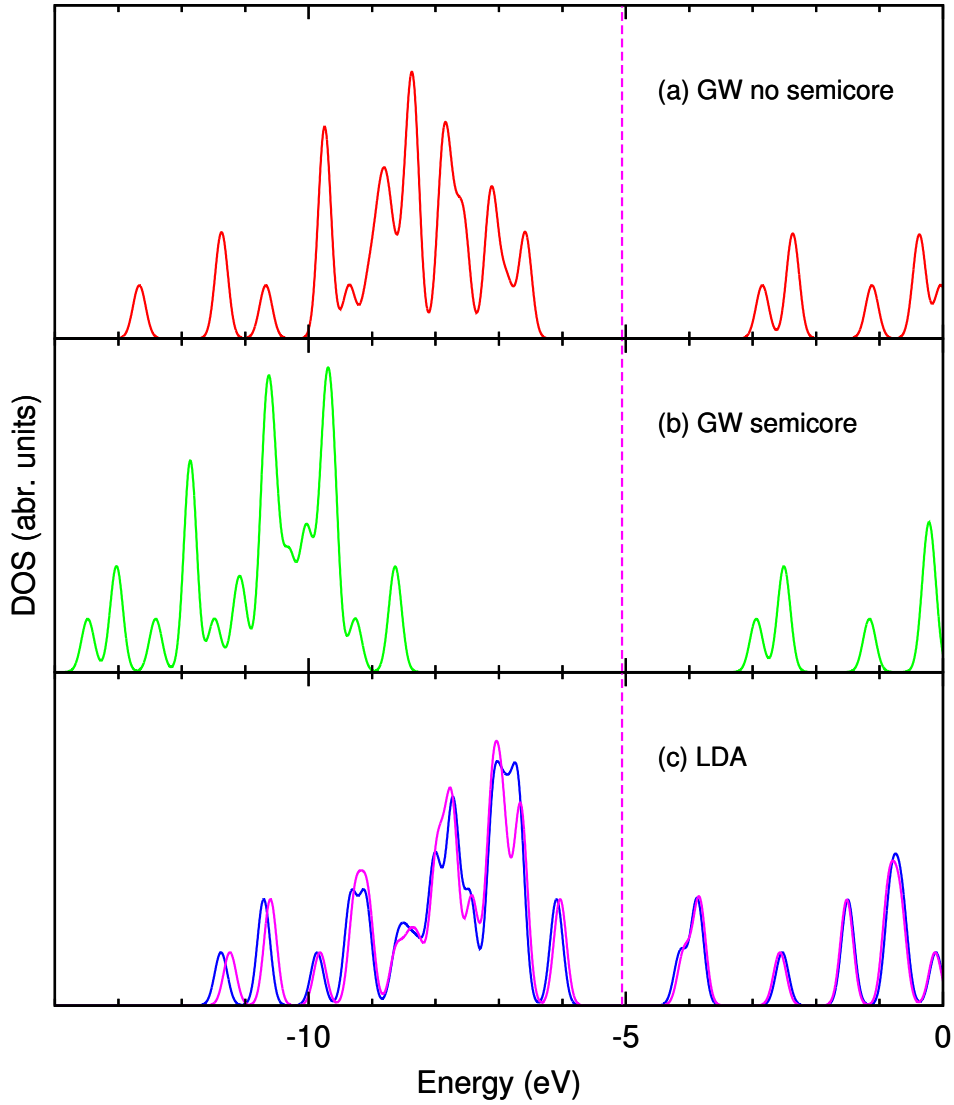

Figure 2.7: Electronic densities of states for the Au_6 cluster, calculated from: (a) GW without Au semicore 5s and 5p states in valence (red), (b) GW with Au semicore 5s and 5p states in valence (green), (c) DFT-LDA without (blue) and with (magenta) Au semicore 5s and 5p states in valence. The dashed magenta line is the Fermi level (the average of HOMO and LUMO energies) for the DFT-LDA calculation with Au semicore 5s and 5p states in valence. A Gaussian broadening of 0.1 eV has been used.

In Fig. [2.7], we report the DOS for the Au_6 cluster obtained from GW (with DFT-LDA as the starting point) and DFT-LDA calculations by using the Au no semicore or semicore pseudopotential. We note that although the two LDA spectra calculated using different pseudopotentials closely resemble each other, the two GW spectra look quite different. In particular, with the no semicore pseudopotential, the GW calculation predicts an (vertical) IP of 6.59 eV, which severely underestimates the experimental value of 8.80 eV [19]. However, by using the semicore pseudopotential, an IP of 8.64 eV is obtained from the GW calculation and is in good agreement with experiment. Combining with the results for some other gold clusters (see Chapter 3 for more details), we conclude that the consideration of the Au semicore 5s and 5p states in valence is necessary for the accurate calculation of the quasiparticle spectra of gold clusters by using the GW method.

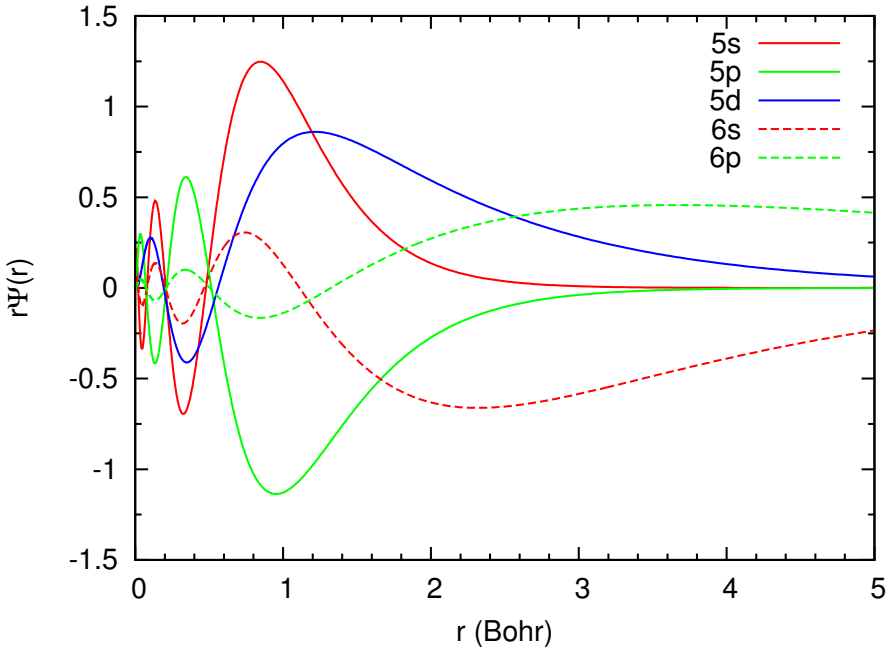

Figure 2.8: Radial parts of all-electron LDA orbitals for the Au 5s, 5p, 5d, 6s and 6p states.

Table 2.1: All-electron LDA energies for the Au 5s, 5p, 5d, 6s and 6p states.

State	5s	5p	5d	6s	6p
Energy (eV)	-108.37	-59.78	-6.88	-5.76	-0.77

To find out the origin of the semicore effects, we performed an all-electron calculation for the gold atom with LDA for the exchange-correlation potential. We plot in Fig. [2.8] the radial parts of some all-electron orbitals, and list in Table. [2.1] their corresponding energies. From the results of the all-electron calculation, we see that the energies of the semicore 5s and 5p states are much lower than that of the 5d, 6s and 6p states. As a result, according to perturbation theory, the semicore 5s and

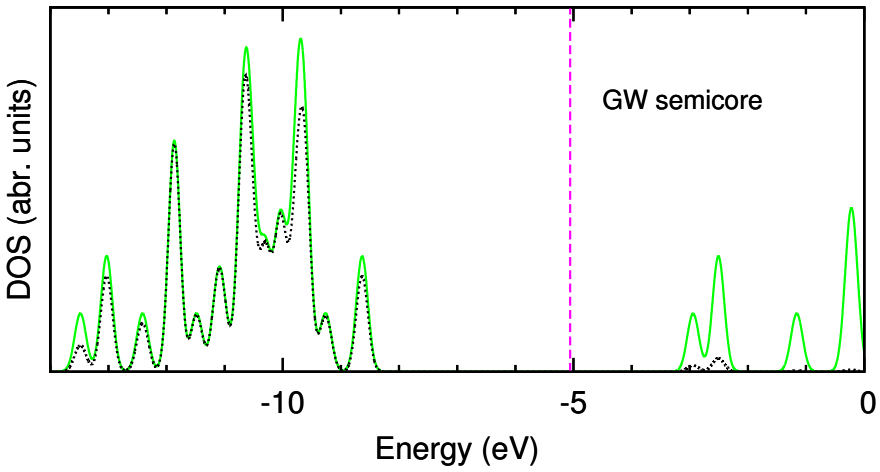

Figure 2.9: Electronic densities of states for the Au_6 cluster, calculated from GW with the Au semicore 5s and 5p states in valence (solid, green) and its projection over the Au 5d states (dotted, black). The dashed magenta line gives the Fermi level for the DFT-LDA calculation with the Au semicore 5s and 5p states in valence.

5p states should participate very little in chemical bonding. This point is reflected by the existence of the small difference between the LDA spectra of the Au_6 cluster calculated with and without the Au semicore 5s and 5p states in valence. However, although the semicore 5s and 5p states are much lower in energy, they have spatial extension comparable to that of the 5d states. Within the G^0W^0 approximation, the expectation value of the exchange term of the self-energy $\langle \Sigma_x \rangle_i$ reads:

$$\langle \psi_i | \Sigma_x | \psi_i \rangle = \sum_v \int d\mathbf{r} d\mathbf{r}' \frac{\psi_i(\mathbf{r}) \psi_v^\star(\mathbf{r}) \psi_v(\mathbf{r}') \psi_i^\star(\mathbf{r}')}{|\mathbf{r} - \mathbf{r}'|}, \tag{2.27}$$

where ψ indicates the Kohn-Sham orbital. It is clear that the above term does not depend on the energies of the orbitals, but only on their localization. Since the semicore 5s and 5p states do have large spatial overlap with the 5d states, the calculated GW energies of those states with strong 5d feature sensitively depend on the presence of the semicore 5s and 5p states in valence. In Fig. [2.9], we highlight the contribution of the Au 5d states to the GW quasiparticle spectrum of the Au_6 cluster calculated with the semicore pseudopotential. While the 5d states contribute very little to the conduction part of the spectrum, it has large contribution all over the valence part. Consequently, with or without the Au semicore 5s and 5p states in valence, the conduction part of the spectrum remains almost the same, but the valence part differs a lot. Similar results are also found for the DOS spectra of other gold clusters calculated at the LDA or GW levels (see Chapter 3).

The explicit inclusion of the Au semicore 5s and 5p states in valence is necessary in order to make sure that the qausiparticle spectra of gold clusters are accurately described. However, such a treatment requires the explicit consideration of more states in the valence manifold, i.e., the Au semicore 5s and 5p states, and requires a much larger cutoff for plane-waves representing molecular orbitals to converge the calculated results, in the case of our Au semicore pseudopotential as large

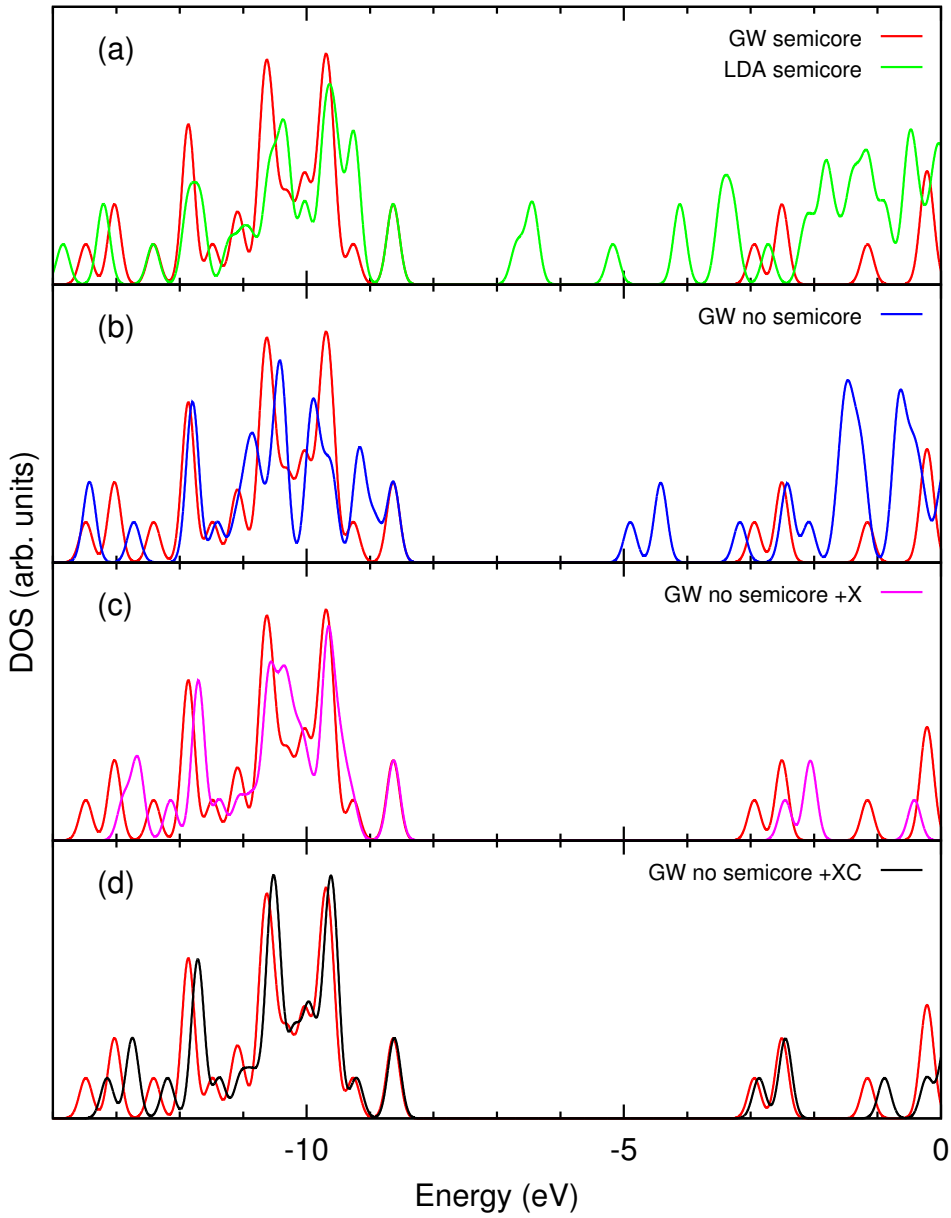

Figure 2.10: Electronic densities of states for the Au_6 cluster, calculated from: GW with Au semicore states in valence, DFT-LDA with Au semicore states in valence, GW without Au semicore states in valence, GW without Au semicore states in valence and with the exchange correction, GW without Au semicore states in valence and with both the exchange and the correlation corrections. The GW semicore spectrum is put in each subfigure to facilitate comparison. The other spectra have been shifted to match their HOMO levels with that of the GW semicore spectrum. A Gaussian broadening of 0.1 eV has been used.

as 120 Ry. This indeed can be computationally very expensive. In order to reduce the computational cost, a simplified approach has been proposed to take account of the effects of the semicore states without including them fully in the GW calculations [49].

As a first correction, the exchange term of the GW quasiparticle energy obtained without the semicore states in valence is replaced by that calculated with the semicore states in valence:

$$E_i' = \epsilon_i + \langle \psi_i^{wo} | \Sigma_c^{wo}(E_i') | \psi_i^{wo} \rangle - \langle \psi_i^{w} | V_{xc}^{w} | \psi_i^{w} \rangle + \langle \psi_i^{w} | \Sigma_x^{w} | \psi_i^{w} \rangle, \tag{2.28}$$

resulting in a corrected quasiparticle energy $\mathrm{E_i'}$. Here "w" and "wo" indicate quantities calculated with and without semicore states in valence respectively, and ϵ_i and $|\psi_\mathrm{i}\rangle$ represent the Kohn-Sham energy and state respectively. In particular, the correlation part of the self-energy $\Sigma_\mathrm{c}^\mathrm{wo}$ is calculated without the semicore states in valence, and the exchange-correlation potential $\mathrm{V_{xc}^w}$ and the exchange part of the self-energy $\Sigma_\mathrm{x}^\mathrm{w}$ are calculated with the semicore states in valence. In Fig. [2.10], we compare the DOS for the $\mathrm{Au_6}$ cluster calculated at some other levels of theory with that calculated from GW with Au semicore 5s and 5p states in valance. The LDA calculation with semicore states and the GW one without semicore states obviously fail to reproduce the quasiparticle spectrum calculated from GW with semicore states. Notably, with the exchange correction only, there is already a large improvement towards the GW results calculated without semicore states.

A second correction is upon the correlation term of the self-energy calculated without semicore states. In addition to the exchange correction, we add in the correlation part of the self-energy a term $\langle \psi_\mathrm{i}^\mathrm{w} | \Sigma_\mathrm{c}'(\mathrm{E_i''}) | \psi_\mathrm{i}^\mathrm{w} \rangle$ due to the contribution of the semicore states to the Green's function G. Now the quasiparticle energy $\mathrm{E_i''}$ is calculated as:

$$\begin{aligned} E_i'' =& \epsilon_i + \langle \psi_i^{wo} | \Sigma_c^{wo}(E_i'') | \psi_i^{wo} \rangle - \langle \psi_i^{w} | V_{xc}^{w} | \psi_i^{w} \rangle + \langle \psi_i^{w} | \Sigma_x^{w} | \psi_i^{w} \rangle \\ &+ \langle \psi_i^{w} | \Sigma_c'(E_i'') | \psi_i^{w} \rangle, \end{aligned} \tag{2.29}$$

where,

$$\Sigma_c'(\omega) = \frac{1}{2\pi} \int d\omega' \sum_{v'=1, N_\mathrm{semicore}} \frac{\psi_{v'}^{w\,*}(\mathbf{r}) \psi_{v'}^{w}(\mathbf{r}')}{\omega - \omega' - \epsilon_{v'}^{w}} W_c^{wo}(\mathbf{r}, \mathbf{r}'; \omega'). \tag{2.30}$$

Here $\mathrm{N_{semicore}}$ is the number of the semicore valence states, with $\epsilon_{\mathrm{v'}}^\mathrm{w}$ indicating their energies, and $\mathrm{W_c^{wo}}$ is the screened Coulomb interaction calculated without semicore states in valence. The screened Coulomb interaction W itself is not corrected, as it is related to the bonding properties of the system through the charge response and we do not expect it to change much with or without including the semicore states in valence. With this additional correction, the shape of the spectrum is further improved and is in excellent agreement with that calculated from GW with semicore states, as can be seen from the comparison presented in Fig. [2.10]. Although the agreement is not perfect, due to the fact that we only correct the Green's function G, but not the screened Coulomb interaction W, the accuracy should be good enough for the purpose of theoretical investigation.

We emphasize that, while the above-described approach can reproduce well the quasiparticle spectrum of GW calculated with semicore states in valence, the computational cost corresponding to

the additional corrections is negligible compared with that of GW calculated without semicore states in valence. This makes it fit to the study of larger gold clusters, such as the "magic" tetrahedral Au_{20} cluster [32] and the cagelike icosahedral Au_{32} cluster [33, 34], which are investigated in Chapter 3.

This approach has been implemented in the GWL module [46] of the QE package [45]. It was first proposed for the simulation of the quasiparticle spectra of metal phthalocyanine molecules [49], and is used for the first time in the study of pure metal clusters (i.e., gold clusters) in this work.

2.2.2 Molecular Open-Shells

The energy levels of highly symmetric molecules may be degenerate. When this is the case for the HOMO, and the number of electrons is not sufficient to fill all the degenerate HOMOs, the HOMO states are said to constitute an *open-shell* of the molecule. In open-shell molecules, it may happen that the DFT electronic charge-density distribution has a lower symmetry than the structural one. As a consequence, on the one hand the symmetry of the SCF potential is lowered, leading to numerical instabilities of the SCF cycle, and on the other hand the molecular orbitals unphysically lack the symmetry of the structure. In order to avoid the occurrence of such a situation, it is common practice to assume that all the degenerate partners of the molecular HOMOs have the same fractional occupancy, fixed so as to enforce the proper normalization of the charge-density distribution.

In the study of small molecules, such as small gold clusters, one can frequently meet symmetric structures with open-shells. One typical example for gold clusters is the equilateral triangular structure of the neutral Au_3 cluster. According to group theory, it is a structure which has the $\mathrm{D}_{3\mathrm{h}}$ symmetry. From DFT-LDA structural optimizations using the Au.pz-d-rrkjus.UPF pseudopotential from the QE package [45], we find that this structure is one of the lowest energy structures of the neutral Au_3 cluster (see Chapter 3), and has a bond length of 2.585 $\mathrm{\AA}$. A DFT-LDA calculation using the same semicore pseudopotential as in our GW study of gold clusters exhibits that, the neutral equilateral Au_3 cluster with the same geometry has an open-shell consisting of two-fold degenerate HOMO states which are occupied by one electron only, as indicated in Fig. [2.11]. Due to the appearance of the open-shell, the LDA LUMO energy is actually the same as the LDA HOMO energy, resulting in a zero LDA HOMO-LUMO gap. The two-fold degenerate HOMOs belong to the E' irreducible representation, and are displayed in Fig. [2.12]. Once one electron is removed from/added to this neutral molecule, the resulting positive/negative molecular ion will be a closed-shell ion.

In Table. [2.2], we compare for the neutral equilateral Au_3 cluster the (vertical) IP, the (vertical) EA and their difference (IP-EA) calculated at difference levels of theory. The IP and the EA are the same at the LDA level, both being 4.91 eV. In contract to LDA, $\Delta\mathrm{SCF}$ calculations based on the Martyna-Tuckerman approach [114] give an IP of 7.36 eV and an EA of 2.36 eV, resulting in a finite difference between the IP and the EA as large as 5.00 eV. In the same table, we report also the IP and the EA calculated from GW with the open-shell treated using fractional occupancies, such that the RPA irreducible polarizability used to compute the screened Coulomb interaction has the same

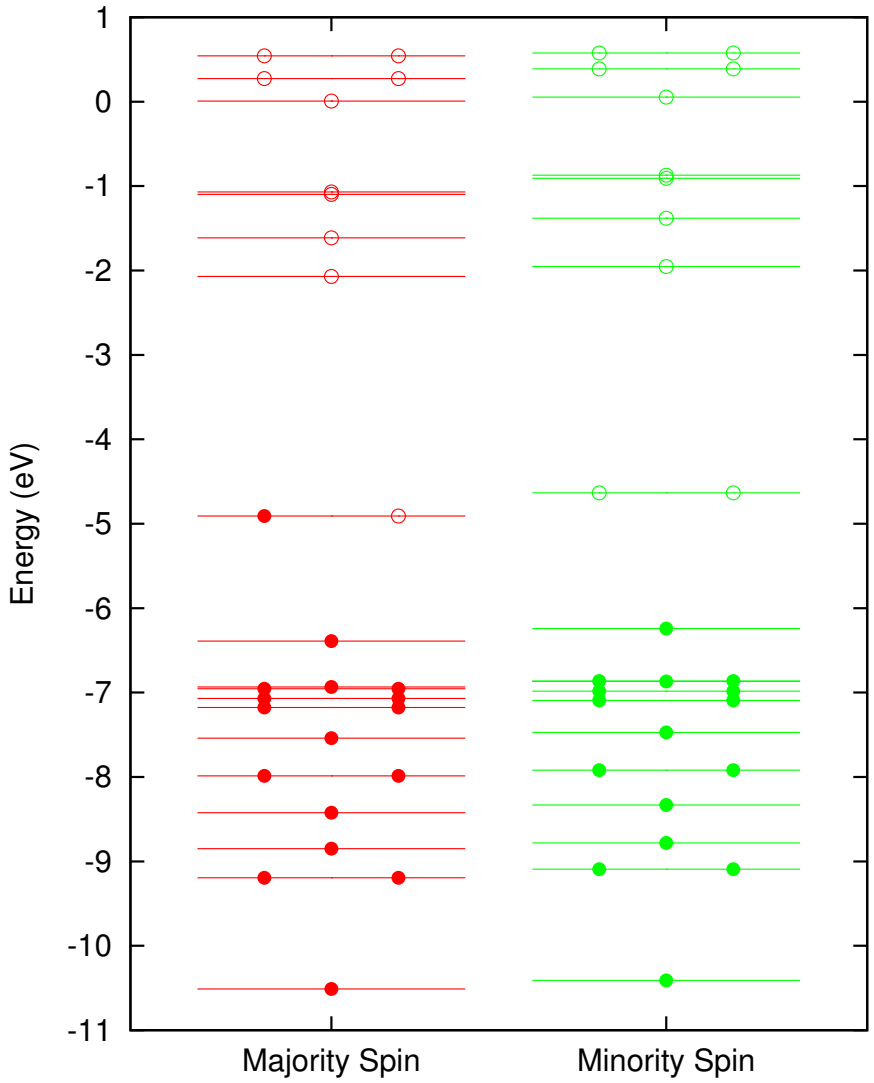

Figure 2.11: Position of the energy levels for the majority spin channel and the minority spin channel of the neutral equilateral Au_3 cluster, calculated from DFT-LDA with the Au semicore 5s and 5p states in valence. Full circles represent occupied states, and empty circles represent unoccupied states. There are only non degenerate and two-fold degenerate energy levels. A non degenerate energy level has one circle in the middle of the energy line, and a two-fold degenerate energy level has two circles on the two sides of the energy line.

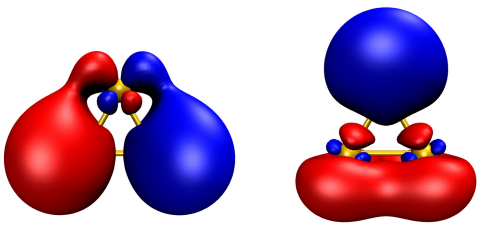

Figure 2.12: Two-fold degenerate HOMOs in the open-shell of the neutral equilateral Au_3 cluster. The HOMOs belong to the E' irreducible representation.

Table 2.2: Vertical ionization potential, vertical electron affinity and their difference for the equilateral triangular structure of the neutral Au_3 cluster, calculated from: DFT-LDA, GW with the open-shell treated using fractional occupancies (GW_f), and ΔSCF, using the pseudopotential with the Au semicore 5s and 5p states in valence. The structure was optimized with DFT-LDA, and the corresponding structural parameters are presented in Table. [2.4]. All energies are in eV.

Theory	IP	EA	IP-EA
LDA	4.91	4.91	0
GW_f	4.46	4.46	0
ΔSCF	7.36	2.36	5.00

form as that would be used in metallic extended systems:

$$P^0(\mathbf{r},\mathbf{r}';\omega) = \sum_{ij}(f_i - f_j)\frac{\psi_i(\mathbf{r})\psi_j^*(\mathbf{r})\psi_j(\mathbf{r}')\psi_i^*(\mathbf{r}')}{\omega + \epsilon_i - \epsilon_j + i\eta}, \tag{2.31}$$

where the f's represent the occupation numbers of Kohn-Sham states. Using this formula, a GW value of 4.46 eV is obtained for both the IP and the EA, leading to a zero GW HOMO-LUMO gap. As we have mentioned, the IP and the EA calculated at the ΔSCF level are usually pretty accurate, and can be used as a first reference in theoretical calculations when experimental values or more accurate quantum chemistry results are not available [78]. Therefore, a correct GW calculation of the open-shell molecule should produce similar results as the ΔSCF ones for the IP and the EA, and produce a non-zero HOMO-LUMO gap[1]. This is clearly not the case here where the open-shell is treated using fractional occupancies in the GW calculation: the calculated IP and EA are far from the ΔSCF ones, thus are qualitatively wrong, and the predicted GW HOMO-LUMO gap is zero. For open-shell molecules, it is appropriate to use fractional occupancies to calculate the charge-density in the DFT calculation, but not physically correct to do so for the evaluation of the self-energy based on Eq. (2.31) in the GW calculation.

In the following, we show how the problem of molecular open-shells in GW calculations can be addressed by making some compromise following several steps: As a first step, a DFT calculation is performed for the open-shell molecule, which would result into an open-shell consisting of degenerate HOMO states with the same fractional occupancy. Then, we perform a GW calculation using a new electronic configuration to evaluate the self-energy, with integer occupancies for the open-shell, such that some of degenerate HOMO states in the open-shell are treated as fully occupied, while the others are assumed to be fully unoccupied. In the meanwhile, the total number of valence electrons is enforced to be the same as that in the DFT calculation. Sine the electronic charge-densities are different between the new electronic configuration and the old one, to obtain the correct GW quasiparticle energies, we must consider the correction to the Hartree energy due to the change in the

[1]For finite systems, in principle there should always be a non-zero difference between the IP and the EA.

charge-density. In the end, the GW quasiparticle energies are calculated as:

$$E_i = \epsilon_i + \langle\psi_i|\Sigma(E_i)|\psi_i\rangle - \langle\psi_i|V_{xc}|\psi_i\rangle + \langle\psi_i|\Delta V_H|\psi_i\rangle, \tag{2.32}$$

where the correction to the Hartree energy is given by the last term on the right hand side of the equation. $\Delta\mathrm{V_H}$ is the correction to the Hartree potential, which reads:

$$\Delta V_H(\mathbf{r}) = \int d\mathbf{r}' \frac{\Delta\rho(\mathbf{r}')}{|\mathbf{r}-\mathbf{r}'|}, \tag{2.33}$$

where $\Delta\rho(\mathbf{r})$ is the difference between the charge-density $\rho_{\mathrm{GW}}(\mathbf{r})$ in the GW calculation and the one $\rho_{\mathrm{DFT}}(\mathbf{r})$ in the DFT calculation. $\Delta\rho(\mathbf{r})$ is calculated as:

$$\begin{aligned}\Delta\rho(\mathbf{r}) &= \rho_{GW}(\mathbf{r}) - \rho_{DFT}(\mathbf{r}) \\ &= \sum_j f_{j,GW}|\psi_j(\mathbf{r})|^2 - \sum_j f_{j,DFT}|\psi_j(\mathbf{r})|^2,\end{aligned} \tag{2.34}$$

where $\mathrm{f_{j,GW}}$ and $\mathrm{f_{j,DFT}}$ are the occupation number in the GW calculation and that in the DFT calculation respectively, for the Kohn-Sham sate j. The difference $(\mathrm{f_{j,GW}} - \mathrm{f_{j,DFT}})$ between the two occupation numbers is non-zero only for the states in the open-shell.

Table 2.3: Vertical ionization potential, vertical electron affinity and their difference for the equilateral triangular structure of the neutral $\mathrm{Au_3}$ cluster, calculated from: DFT-LDA, GW with the open-shell treated using fractional occupancies ($\mathrm{GW_f}$), our GW scheme with the open-shell treated using integer occupancies ($\mathrm{GW_i}$), and $\Delta\mathrm{SCF}$, using the pseudopotential with the Au semicore 5s and 5p states in valence. The structure was optimized with DFT-LDA, and the corresponding structural parameters are presented in Table. [2.4]. All energies are in eV.

Theory	IP	EA	IP-EA
LDA	4.91	4.91	0
$\mathrm{GW_f}$	4.46	4.46	0
$\mathrm{GW_i}$	7.26	3.21	4.05
$\Delta\mathrm{SCF}$	7.36	2.36	5.00

In the specific case of the GW calculation of the neutral equilateral $\mathrm{Au_3}$ cluster, we treat the HOMO state that corresponds to the first orbital displayed in Fig. [2.12] as fully occupied, and the other HOMO state as fully unoccupied. In Table. [2.3], we compare various schemes for the calculation of the IP and the EA of this molecule. By using our GW scheme for open-shell molecules, a value of 7.26 eV is obtained for the IP, which is in close agreement with the $\Delta\mathrm{SCF}$ value 7.36 eV, and much better than the LDA value 4.91 eV and the value 4.26 eV calculated from GW with the open-shell treated using fractional occupancies. In contrast to LDA and GW with fractional occupancies, a non-zero HOMO-LUMO gap is obtained by using our GW scheme. The agreement between our GW scheme and $\Delta\mathrm{SCF}$ for the EA is not as good as that for the IP. This may be because the DFT-LDA calculation in this case is not a good starting point for the GW calculation

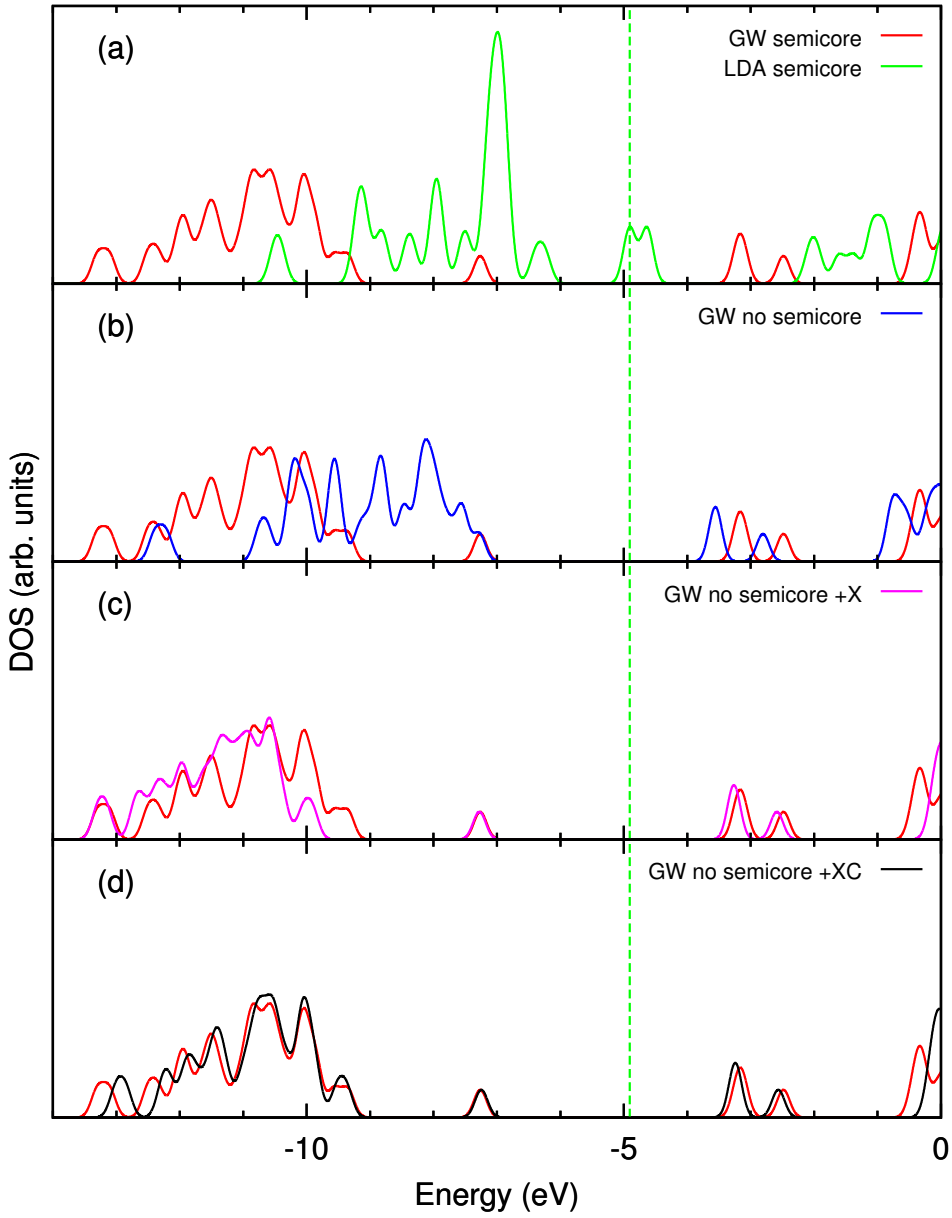

Figure 2.13: Electronic densities of states for the neutral equilateral Au_3 cluster, calculated from: GW with Au semicore states in valence (GW semicore), DFT-LDA with Au semicore states in valence (LDA semicore), GW without Au semicore states in valence (GW no semicore), GW without Au semicore states in valence and with the exchange correction to the self-energy (GW no semicore +X), GW without Au semicore states in valence and with both the exchange and the correlation corrections to the self-energy (GW no semicore +XC). The GW semicore spectrum is put in each subfigure to facilitate the comparison. The other GW spectra have been shifted to match their HOMO levels with that of the GW semicore spectrum. All the GW calculations were performed by using our scheme for open-shell molecules. A Gaussian broadening of 0.1 eV has been used.

of the empty (conduction) part of the quasiparticle spectrum. We think that the agreement may be improved if some degree of self-consistency is added in the GW calculation. GW calculations were also performed to test how good the simplified scheme for the treatment of semicore states is, in conjunction with our scheme for open-shell molecules. In Fig. [2.13], we compare for the neutral equilateral $\mathrm{Au_3}$ cluster the electronic densities of states calculated from various schemes. As expected, the simplified scheme works well for this molecule in conjunction with our scheme for open-shell molecules.

Table 2.4: The symmetry, the angle θ_e (in degree) between two bonds with equal length $\mathrm{r_e}$ (in Å), and the relative energy (in eV) for different structures of the neutral $\mathrm{Au_3}$ cluster. All the structures were optimized with either DFT-LDA by using the Au.pz-d-rrkjus.UPF pseudopotential or DFT-PBE by using the Au.pbe-nd-rrkjus.UPF pseudopotential. The two pseudopotentials are from the QE package [45].

Pseudopotential	Symmetry	θ_e	$\mathrm{r_e}$	ΔE
Au.pz-d-rrkjus.UPF	$\mathrm{C_{2v}}$	64.1	2.543	0
	$\mathrm{D_{3h}}$	60.0	2.585	0.01
Au.pbe-nd-rrkjus.UPF	$\mathrm{C_{2v}}$	66.0	2.623	0
	$\mathrm{C_{2v}}$	56.7	2.730	0.02
	$\mathrm{D_{3h}}$	60.0	2.677	0.03

One interesting property of open-shell molecules results from the Jahn-Teller theorem [115], which states that: *Any electronically degenerate molecular system is intrinsically unstable, and will undergo structural distortion to a structure with lower symmetry and energy, such that the electronic degeneracy is removed, unless the system has a linear structure or the degeneracy is Kramers twofold degeneracy.* According to the Jahn-Teller theorem, the equilateral triangular structure of the neutral $\mathrm{Au_3}$ cluster is intrinsically unstable. To illustrate the point, we display in Table. [2.4] for the $\mathrm{Au_3}$ cluster the structural parameters of the equilateral triangular structure, as well as of the distorted triangular structures. Indeed with both DFT-LDA and DFT-PBE structural optimizations, we find structure(s) with symmetry and energy lower than those for the equilateral triangular structure. With DFT-LDA, we find one slightly distorted structure, an obtuse-angle triangular structure 0.01 eV lower in energy. With DFT-PBE, we find two slightly distorted structures, an acute-angle triangular structure 0.01 eV lower in energy, and an obtuse-angle triangular structure 0.03 eV lower in energy. All the distorted structures possess the $\mathrm{C_{2v}}$ symmetry, which is lower than the $\mathrm{D_{3h}}$ symmetry of the equilateral triangular structure. Due to the lower symmetry, the electronic degeneracy associated with the equilateral triangular structure has been removed for the distorted structures.

As for the equilateral $\mathrm{Au_3}$ cluster, Jahn-Teller distortions are small, we expect that the electronic properties corresponding to the undistorted and the distorted structures are similar. In Table. [2.5], we report the (vertical) IP, the (vertical) EA, and their difference (IP-EA) calculated at different levels

Table 2.5: Vertical ionization potential, vertical electron affinity and their difference for the equilateral triangular structure and the obtuse-angle triangular structure of the neutral Au_3 cluster, calculated from: DFT-LDA, GW and ΔSCF, using the pseudopotential with the Au semicore 5s and 5p states in valence. For the equilateral triangular structure, the GW calculation was performed by using our scheme with the open-shell treated using integer occupancies. The two structures were optimized with DFT-LDA, and the corresponding structural parameters are presented in Table. [2.4]. All energies are in eV.

Structure	Theory	IP	EA	IP-EA
Equilateral triangle	LDA	4.91	4.91	0
	GW_i	7.26	3.21	4.05
	ΔSCF	7.36	2.36	5.00
Obtuse-angle triangle	LDA	4.92	4.88	0.04
	GW	7.50	2.95	4.55
	ΔSCF	7.42	2.34	5.08

of theory for the equilateral triangular structure and the distorted obtuse-angle triangular structure. For the obtuse-angle triangular structure, the IP and the EA calculated from DFT-LDA are different by 0.04 eV, meaning that there is no open-shell for this structure. In fact, because of the lower symmetry compared with that of the equilateral triangular structure, the state that corresponds to the first orbital drawn in Fig. [2.12] becomes a completely occupied valence state, while the state that corresponds to the other orbital drawn in Fig. [2.12] becomes a completely unoccupied conduction state. At a same level of theory, the calculated IPs/EAs for the two structures are close to each other, indicating that indeed the two structures correspond to similar electronic properties. Between the two structures, the difference in the calculated IPs/EAs at the GW level is larger than that at the ΔSCF level. This comes mainly from the slightly poorer quality of the compromised GW calculation for the equilateral triangular structure: since we have changed by hand the electronic configuration, the quality of this calculation is not expected to be as good as that of the standard GW calculation for the obtuse-angle triangular structure and those of the ΔSCF calculations for both structures. Nevertheless, for the equilateral triangular structure, the agreement between the GW results and the ΔSCF ones are at a level of quality comparable to that for the obtuse-angle triangular structure. This demonstrates that the GW scheme that we use for open-shell molecules does make sense, and is capable of providing useful information of the quasiparticle spectra. This is also illustrated in our study of the open-shell neutral hexagonal Au_7 cluster. Note that, for the equilateral triangular structure, the overestimation in the EA at the GW level as compared with the ΔSCF result is not due to the problem of the compromised GW scheme, as similar overestimation is also found for the obtuse-angle triangular structure.

Our scheme for molecular open-shells has been implemented in the GWL module [46] of the

QE package [45]. It is used in our study of two neutral open-shell molecules, the equilateral Au_3 cluster and the hexagonal Au_7 cluster, as well as in our study of the neutral linear Au_3 cluster, for which the HOMO state and the LUMO state are almost degenerate and the smearing technique used to converge the DFT calculation results in fractional occupancies for them (see Chapter 3).

Chapter 3

Results for Gold Clusters

In this chapter, we use the implementation of the GW method described in the previous chapter to investigate the electronic properties of neutral gold clusters. We first give the computational details. After that, we present the results for small clusters $\mathrm{Au_N}$ ($\mathrm{N} = 1 - 8$) (including the Au atom), as well as for two larger clusters, the tetrahedral $\mathrm{Au_{20}}$ cluster and the cagelike $\mathrm{Au_{32}}$ cluster. Several aspects concerning equilibrium geometries, molecular orbitals, ionization potentials, electron affinities, and electronic densities of states are discussed.

3.1 Computational Details

In this work, we use the Quantum Espresso (QE) density-functional package [45] to perform first principles electronic structure calculations. The QE package is based on plane-waves and pseudopotentials, and takes advantage of periodic boundary conditions. The GWL (GW + Wannier + Lanczos) module [46] of QE is employed to perform all the GW calculations.

Our implementation of the GW method in the GWL module is described in detail in the previous chapter. It is based on the $\mathrm{G^0W^0}$ approximation, with the DFT calculation as the starting point for the GW calculation, and has incorporated recently introduced algorithms which can significantly reduce the computational cost of GW calculations, i.e., the construction of the optimal polarizability basis [48] and the Lanczos chain technique for the evaluation of the irreducible polarizability and the self-energy [48]. A simplified scheme is used to account for the effects of the Au semicore 5s and 5p states without including them fully in the GW calculations [49]. Since this scheme can significantly speed up the calculations without compromising much the accuracy of the calculated quasiparticle spectra, it is suitable for the study of larger gold clusters and is thus used to investigate the electronic properties of the neutral tetrahedral $\mathrm{Au_{20}}$ cluster and the neutral cagelike $\mathrm{Au_{32}}$ cluster. By making some compromise, we have also treated properly molecular open-shells in our implementation of the GW method. In the following, some numerical details of our calculations are presented.

We perform spin-polarized calculations for gold clusters with an odd number of electrons, and non spin-polarized ones for those with an even number of electrons. LDA is used for the exchange-correlation potential. Only valence electrons are considered explicitly, and their interactions with ionic cores are described by pseudopotentials including scalar-relativistic effects. Molecular orbitals and electronic charge-density are expanded in terms of plane-waves. Since we are only interested in finite systems, i.e., isolated gold clusters, all the calculations were performed in supercells that are large enough such that the spurious Coulomb interactions between the system and its images in neighboring cells do not influence much the calculated results. To converge the DFT calculations, whenever necessary, we use either the Fermi-Dirac smearing technique with a smearing parameter not larger than 0.0001 Ry, or a fixed electronic configuration in which an equal fractional occupancy is enforced for each of the degenerate HOMOs in the open-shell. The evaluation of the IP and the EA at the $\Delta\mathrm{SCF}$ level involves the calculation of the total energy of charged clusters. In order to obtain a well-converged value for the total energy of a charged cluster, the Martyna-Tuckerman approach [114] is used to subtract the contribution due to the spurious Coulomb interactions between the system and its images.

Table 3.1: Lattice constant $\mathrm{a_0}$ (in $\mathrm{\AA}$) and bulk modulus $\mathrm{B_0}$ (in GPa) of bulk gold, calculated with the three pseudopotentials that we use to study gold clusters, and comparison with those calculated with the scalar-relativistic all-electron full-potential linearized-augmented-plane-wave method and with the experimental values.

	$\mathrm{a_0}$	$\mathrm{B_0}$
Au.pz-d-rrkjus.UPF	7.65	192
No semicore pseudopotential	7.65	196
Semicore pseudopotential	7.62	196
All-electron FPLAPW [116]	7.66	198
Experiment [116]	7.67	172

In the study reported in this chapter, we use three LDA pseudopotentials for the Au atom whose electronic configuration is $[\mathrm{Xe}]4\mathrm{f}^{14}5\mathrm{d}^{10}6\mathrm{s}^{1}$. The ultrasoft pseudopotential Au.pz-d-rrkjus.UPF from the QE distribution is used for DFT-LDA structural optimizations, with a kinetic energy cutoff of 40 Ry and 600 Ry for plane-waves representing molecular orbitals and charge-density, respectively. In this pseudopotential, the Au 5d and 6s electrons are treated as the valence ones. Since our GW schemes have only been implemented for norm-conserving pseudopotentials and we do not have at hand any available LDA one for the Au atom, we generated two norm-conserving pseudopotentials with Perdew-Zunger LDA exchange-correlation potential [117] ourselves, by using the ld1.x code of the QE package. The first norm-conserving pseudopotential was generated in a semi-local form with the Rabe-Rappe-Kaxiras-Joannopoulos method [118]. In common with most other pseudopotentials for the Au atom used in DFT calculations, this pseudopotential treats the Au 5d and 6s electrons

as the valence ones, resulting in a total number of 11 valence electrons. In addition, the empty 6p electrons are also considered. A pseudization radius of 1.8 Bohr, 2.8 Bohr and 3.3 Bohr is used for the 5d, 6s and 6p electrons, respectively. We call this pseudopotential the no semicore pseudopotential. The second norm-conserving pseudopotential was generated in a fully non-local form with the Troullier-Martins method [119]. In this pseudopotential, in addition to the Au 5d and 6s electrons, the Au semicore 5s and 5p electrons are also included in the valence manifold, resulting in a total number of 19 valence electrons. Similarly to the first norm-conserving pseudopotential, the empty 6p electrons are also considered. A pseudization radius of 0.95 Bohr, 1.0 Bohr and 1.1 Bohr is used for the s (5s and 6s), p (5p and 6p) and d (5d) electrons, respectively. We call this pseudopotential the semicore pseudopotential. In the calculations performed with the no semicore pseudopotential, we use a kinetic energy cutoff of 60 Ry for representing molecular orbitals, while in the cases where the semicore pseudopotential is used, a cutoff as large as 120 Ry is required to converge the calculated results. To test these three pseudopotentials, in Table. [3.1] we compare the calculated lattice constant and bulk modulus of bulk gold with those calculated by using the scalar-relativistic all-electron full-potential linearized-augmented-plane-wave (FPLAPW) method and also with the experimental values. All the three pseudopotentials are good in quality, since they produce results that are very close to the all-electron ones on the one hand, and agree well with the experimental values on the other hand.

For neutral gold clusters, we use a large cubic supercell with an edge of 50 Bohr to perform structural optimizations and $\Delta\mathrm{SCF}$ calculations. Supercells of different sizes are used in GW calculations of neutral gold clusters containing a different number of atoms. In particular, we use a cubic supercell with an edge of 20 Bohr for Au and $\mathrm{Au_2}$, an orthorhombic supercell of $25 \times 25 \times 20\ \mathrm{Bohr}^3$ for $\mathrm{Au_3}$, $\mathrm{Au_4}$, $\mathrm{Au_5}$ and $\mathrm{Au_6}$, an orthorhombic supercell of $30 \times 30 \times 24\ \mathrm{Bohr}^3$ for $\mathrm{Au_7}$ and $\mathrm{Au_8}$, and a cubic supercell with an edge of 35 Bohr for $\mathrm{Au_{20}}$ and $\mathrm{Au_{32}}$. We use orthorhombic supercells for $\mathrm{Au_N}$ ($\mathrm{N} = 3 - 8$) since only planar structures are considered for them, with the plane of the structure lying parallel to the supercell face with the largest area. For each cluster, in the evaluation of both the exchange and the correlation terms of the self-energy, we truncate the spurious Coulomb interactions by using a truncation radius as large as half of the length of the longest edge of the supercell. The sizes of the supercells chosen for the GW calculations ensure that, for frontier molecular orbitals, the convergence in the DFT-LDA energy levels is within $\sim 0.02\ \mathrm{eV}$ and that in the corresponding perturbative Hartree-Fock energies[1] is within $\sim 0.05\ \mathrm{eV}$.

An optimal polarizability basis is constructed for each neutral gold cluster by using a cutoff $\mathrm{E}^\star = 5\ \mathrm{Ry}$ and a threshold $\mathrm{q}^\star < 10\ \mathrm{Bohr}^3$ (see Eq. (2.13) and Eq. (2.15)), which guarantees that the constructed basis is small, and the convergence in the calculated quasiparticle energies of frontier molecular orbitals is within $\sim 0.1\ \mathrm{eV}$. 30 and 200 Lanczos steps are used for the evaluation of the

[1] The perturbative Hartree-Fock energy is calculated as the sum of the DFT-LDA energy and the exchange contribution to the self-energy.

irreducible polarizability and the self-energy, respectively, and have been checked to make sure that the convergence in the calculated quasiparticle energies of frontier molecular orbitals is within $\sim 0.02\,\mathrm{eV}$.

Overall, the convergence in $\Delta\mathrm{SCF}$ results for the IP and the EA is well within 0.01 eV. A final convergence of $\sim 0.15\,\mathrm{eV}$ is estimated for the calculated GW quasiparticle energies around frontier molecular orbitals, with convergence in the corresponding DFT energy levels within $\sim 0.02\,\mathrm{eV}$.

3.2 Electronic Properties of Small Gold Clusters $\mathrm{Au_N}$ ($\mathrm{N} = 1 - 8$)

In this section, we present the results for small neutral gold clusters $\mathrm{Au_N}$ ($\mathrm{N} = 1 - 8$). Several aspects concerning equilibrium geometries, molecular orbitals, ionization potentials, electron affinities, and electronic densities of states are discussed.

3.2.1 Equilibrium Geometries

As mentioned, the geometries of neutral gold clusters were optimized with DFT-LDA by using the Au.pz-d-rrkjus.UPF pseudopotential from the QE distribution. In Fig. [3.1], we display the equilibrium geometries for low energy structures of $\mathrm{Au_N}$ ($\mathrm{N} = 2 - 8$). At each cluster size, only structures corresponding to a calculated total energy within $\sim 0.2\,\mathrm{eV}$ from the lowest energy one are considered. This is because 0.2 eV is the typical accuracy of DFT calculations for the total energy of these systems [21, 22]. Candidate low energy structures are taken from the literature [24–31].

In the size range $\mathrm{N} = 4 - 8$, all the low energy structures are found to be planar. The tendency of small gold clusters to favor planar structures has been attributed to the strong relativistic effects in gold [37, 38]. We find that there are several energetically competing structures for $\mathrm{Au_3}$, $\mathrm{Au_4}$ and $\mathrm{Au_7}$, respectively. In particular, for $\mathrm{Au_3}$, the lowest energy structure is the obtuse-angle triangular structure 3a, which is actually a Jahn-Teller distorted structure of the equilateral triangular structure 3b. Only one low energy structure is found for $\mathrm{Au_5}$, $\mathrm{Au_6}$ and $\mathrm{Au_8}$, respectively. When there are several energetically competing low energy structures at the same cluster size, due to the intrinsic limitation of the accuracy of DFT calculations, we can not determine which structure is actually the ground-state one by only looking at the calculated total energies.

Different studies may have found different total energy orderings for the various structures at different cluster sizes, but most of them found the same set of low energy structures [24–31]. To the best of our knowledge, the lowest energy structure at each cluster size of neutral $\mathrm{Au_N}$ ($\mathrm{N} = 3 - 8$) hasn't been determined experimentally yet, expect for $\mathrm{Au_7}$, for which the 7a structure has been determined as the lowest energy one by a combined study of the vibrational spectroscopy from DFT calculations and experiment [23].

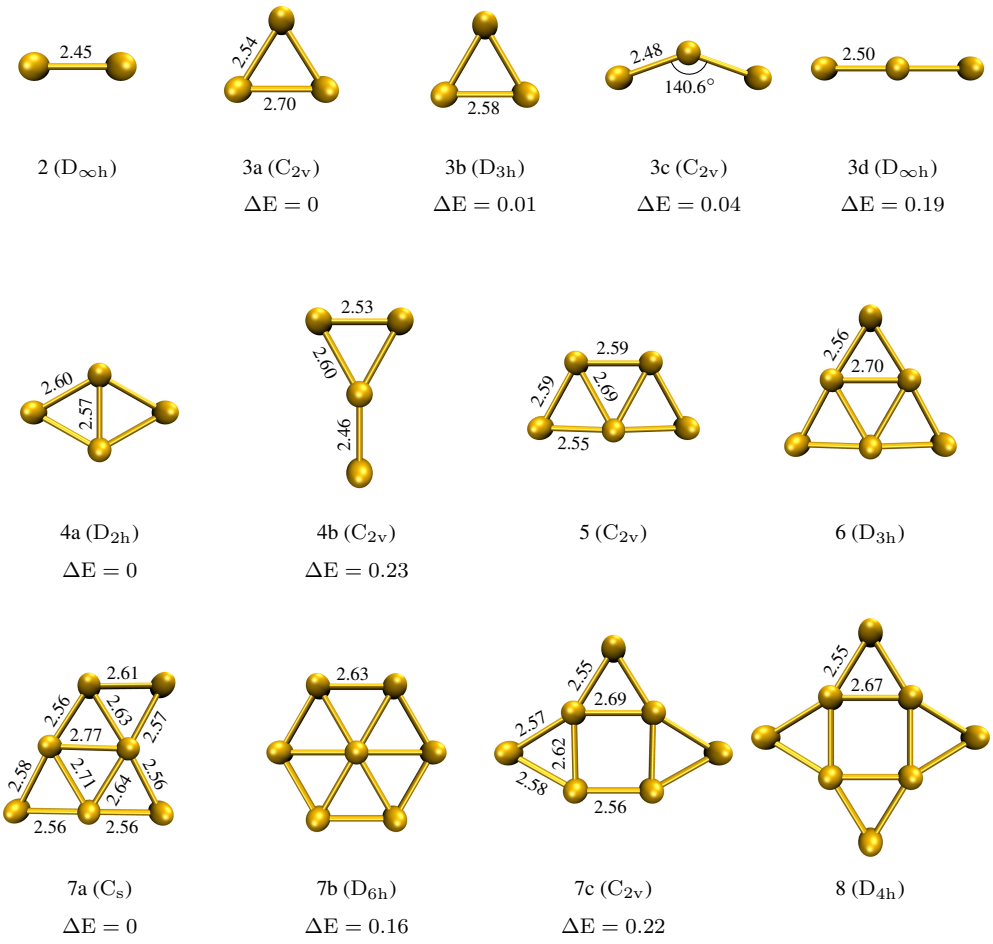

Figure 3.1: Equilibrium geometries for low energy structures at each cluster size of Au_N ($N = 2 - 8$). Structural parameters are given along with each structure, with bond lengths given in Å, and the structural symmetry is listed inside the parenthesis beside the structural label. For some structures, the relative energy ΔE (in eV) from the lowest energy structure at the same cluster size is also presented. The structural labels here are used throughout the rest of this thesis.

3.2.2 Molecular Orbitals

In Fig. [3.2], we display (the moduli square of) the HOMO(s) and the LUMO calculated from DFT-LDA, for different structures of $\mathrm{Au_N}$ ($\mathrm{N} = 2 - 8$). For the structures 3b and 7b, with which neutral gold clusters become open-shell molecules, we plot the half-occupied two-fold degenerate HOMOs in the open-shell. The HOMOs of the $\mathrm{Au_6}$ cluster are also two-fold degenerate, but they are fully occupied instead of being half occupied. For the $\mathrm{Au_3}$ cluster with the 3d structure, the HOMO and the LUMO are almost degenerate, and the Fermi-Dirac smearing technique used to converge the DFT calculation results in fractional occupancies for them[2]. Here the fact that the HOMO is almost degenerate with the LUMO is not due to the structural symmetry, since the degeneracy can be broke by changing the bond length while keeping the $\mathrm{D_{\infty h}}$ symmetry of the structure.

For the Au atom, the $\mathrm{Au_3}$ cluster with the 3c structure, the $\mathrm{Au_5}$ cluster, and the $\mathrm{Au_7}$ cluster with the 7a or 7c structure, the HOMO belongs to the majority spin channel while the LUMO belongs to the minority spin channel. For the $\mathrm{Au_3}$ cluster with the 3b structure and the $\mathrm{Au_7}$ cluster with the 7b structure, the half-occupied two-fold degenerate HOMOs in the open-shell both belong to the majority spin channel. For the $\mathrm{Au_3}$ cluster with the 3d structure, the HOMO and the LUMO both belong to the minority spin channel.

The shapes of molecular orbitals reflect the symmetry of the structure. When a state is non-degenerate with any other state, its charge-density must have the same symmetry as the structure. An example is for the non-degenerate LUMO of the $\mathrm{Au_6}$ cluster, which is displayed in Fig. [3.2]. In constrast, when a state is degenerate with any other state due to the structural symmetry, its charge-density does not necessarily possess the same symmetry as the structure, but the equally weighted linear combination of the charge-densities of the degenerate states must. For example, as displayed in Fig. [3.2], the charge-density of each of the two-fold degenerate HOMOs of the $\mathrm{Au_6}$ cluster does not possess the same $\mathrm{D_{3h}}$ symmetry as the structure, but it can be shown that the equally weighted linear combination of them has exactly the $\mathrm{D_{3h}}$ symmetry. Moreover, in any case, a molecular orbital should belong to an irreducible representation associated with the structural symmetry.

3.2.3 Ionization Potentials

In Table. [3.2], we report the (vertical) IPs of $\mathrm{Au_N}$ ($\mathrm{N} = 1 - 8$) calculated at different levels of theory, and compare them with experiment. For the GW calculations of two open-shell molecules, the $\mathrm{Au_3}$ cluster with the 3b structure and the $\mathrm{Au_7}$ cluster with the 7b structure, the first HOMO in the open-shell displayed in Fig. [3.2] is treated as fully occupied, while the other HOMO is treated as fully unoccupied. Our scheme for open-shell molecules is also used in the GW calculation of

[2]We use a smearing parameter of 0.00001 Ry. By using the no semicore norm-conserving pseudopotential, we find that the HOMO is $\sim 91.2\%$ occupied and the LUMO is $\sim 8.8\%$ occupied, with an energy difference between them as small as 0.6 meV. By using the semicore norm-conserving pseudopotential, we find that the HOMO is $\sim 93.8\%$ occupied and the LUMO is $\sim 6.2\%$ occupied, with an energy difference between them as small as 0.8 meV.

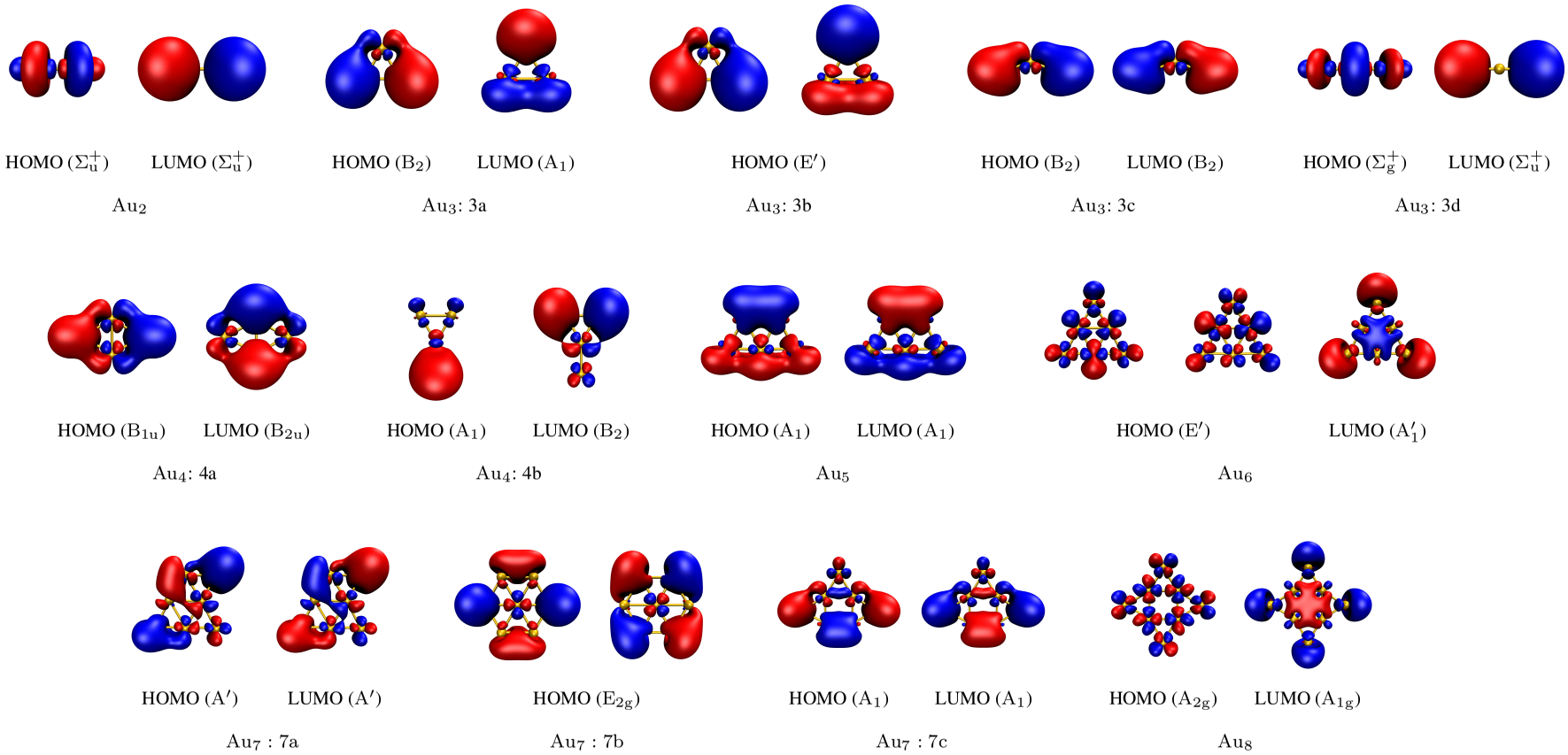

Figure 3.2: HOMO(s) and LUMO for different structures of Au_N ($N = 2 - 8$). Red and blue colors indicate the two opposite signs of molecular orbitals, respectively[a]. The corresponding irreducible representations are given in the parentheses.

[a]Due to time-reversal invariance of the Kohn-Sham Hamiltonians under consideration, all the Kohn-Sham orbitals resulting from our DFT calculations are real. This makes it possible to keep the signs of the molecular orbitals.

Table 3.2: Vertical ionization potentials for different structures of $\mathrm{Au_N}$ ($\mathrm{N} = 1 - 8$), calculated from: DFT-LDA with Au semicore states in valance (LDA), GW without Au semicore states in valence ($\mathrm{GW_{nsc}}$), GW without Au semicore states in valence and with the exchange correction to the self-energy ($\mathrm{GW_{sc}^{X}}$), GW without Au semicore states in valence and with both the exchange and the correlation corrections to the self-energy ($\mathrm{GW_{sc}^{XC}}$,), GW with Au semicore states in valence ($\mathrm{GW_{sc}}$), and $\Delta\mathrm{SCF}$ with Au semicore states in valence ($\Delta\mathrm{SCF}$). The calculated results are compared with the experimental values. All energies are in eV.

Cluster	LDA	$\mathrm{GW_{nsc}}$	$\mathrm{GW_{sc}^{X}}$	$\mathrm{GW_{sc}^{XC}}$	$\mathrm{GW_{sc}}$	$\Delta\mathrm{SCF}$	Expt [19]
1	6.31	8.79	9.66	9.58	9.76	9.89	9.23
2	6.52	7.78	9.86	9.66	9.77	9.90	9.50
3a	4.92	6.88	7.37	7.24	7.50	7.42	7.50
3b	4.91	6.88	7.13	7.00	7.26	7.36	
3c	6.29	7.33	8.72	8.51	8.72	8.77	
3d	6.39	7.10	8.68	8.59	8.97	9.12	
4a	5.86	6.85	8.48	8.17	8.30	8.27	8.60
4b	6.08	6.67	8.41	8.47	8.60	8.65	
5	5.62	6.89	7.63	7.44	7.63	7.82	8.00
6	6.04	6.59	8.98	8.42	8.64	8.34	8.80
7a	5.44	6.48	7.38	7.13	7.52	7.41	7.80
7b	4.96	6.74	6.77	6.62	6.92	6.88	
7c	5.73	6.14	7.63	7.42	7.64	7.66	
8	5.88	5.97	8.65	8.15	8.37	7.93	8.65

the Au_3 cluster with the 3d structure, with the HOMO treated as fully occupied while the LUMO treated as fully unoccupied. In the cases of the Au atom, the Au_2, Au_5, Au_6 and Au_8 clusters, where we find only one low energy structure at the theoretical level, the IPs calculated at the GW semicore and ΔSCF levels are in good agreement with experiment. In the cases of the Au_3, Au_4 and Au_7 clusters, where we find more than one low energy structures, the IPs calculated at the GW semicore and ΔSCF levels for the lowest energy structure at each cluster size also agree well with experiment. In fact, for the lowest energy structure at each cluster size, we find that the IP calculated at the GW semicore level agrees better with experiment than that calculated at the ΔSCF level, except for Au_5, for which the IP calculated at the GW semicore level is 0.19 eV further from experiment than that calculated at the ΔSCF level. The good agreement between the GW semicore results and the experimental values indicates that the IPs of neutral gold clusters can be calculated accurately at the GW semicore level. As mentioned before, since the IPs calculated at the ΔSCF level are usually pretty accurate for finite systems, they can be used as a first reference when the experimental values or more accurate quantum chemistry results are not available. The good agreement between the IP calculated at the GW semicore level and that calculated at the ΔSCF level for each considered structure further demonstrates the good accuracy of the GW semicore results. Furthermore, for all the structures considered, the IPs calculated at the GW semicore level are often severely underestimated by the DFT-LDA and GW no semicore calculations, but are generally well reproduced by the GW no semicore +X and GW no semicore +XC calculations, thus proving the good quality of the simplified scheme that we use to account for the semicore effects.

When compared with the experimental values, the IPs calculated at the GW semicore level (also those calculated at the GW no semicore+X, GW no semicore +XC and ΔSCF levels) can help to identify the structures of gold clusters appearing in experiment. Since the IPs calculated at the GW semicore level for the 3c and 3d structures, being 8.72 eV and 8.97 eV respectively, are much larger than the experimental value of 7.50 eV for Au_3, the structure appearing in experiment can not be the 3c or 3d structure. For Au_4, since the IPs calculated at the GW semicore level for the 4a and 4b structures, being 8.30 eV and 8.60 eV respectively, are close to each other and both agree with the experimental value of 8.60 eV, we can not tell which structure is the one appearing in experiment by only comparing the calculated IPs with experiment. The same thing happens to Au_7, for which close IP values in agreement with experiment are found at the GW semicore level for the 7a and 7c structures. In the cases of the Au_5, Au_6 and Au_8 clusters, where only one low energy structure is found at each cluster size, the good agreement between the IPs calculated at the GW semicore level and the experiment values suggests that the structures found are very likely to be the ones appearing in experiment.

Since there may be energy level crossings after applying the GW quasiparticle energy corrections to the LDA energy levels, the GW HOMO state is not necessarily the LDA HOMO state[3]. We

[3]LDA HOMO and GW HOMO in the sense of considering both spin channels.

find two cases where energy level crossing occurs to the GW semicore HOMO state: for Au_2, the GW semicore HOMO state corresponds to the LDA HOMO-2 state, with a crossing energy (the difference between the GW quasiparticle energy correction for the GW HOMO state and that for the LDA HOMO state) of 0.61 eV; for the Au_3 cluster with the 3d structure, the GW semicore HOMO state corresponds to the LDA HOMO-2 state of the majority spin channel, with a crossing energy of 1.71 eV. The Au_8 cluster is the only case where the GW no semicore +X, GW no semicore +XC and GW semicore HOMO states do not correspond to the same state. In this case, the GW no semicore +XC and GW semicore HOMO states indeed correspond to the LDA HOMO state, but the GW no semicore +X HOMO state corresponds to the LDA HOMO-4 state[4], with a crossing energy of 0.86 eV. However, between the LDA HOMO-4 state and the LDA HOMO state, there is only a 0.14 eV difference in the calculated GW no semicore+X energies. More energy level crossings for the GW HOMO state are found at the GW no semicore level. The crossing energy for the GW HOMO state can be as large as ~ 2 eV.

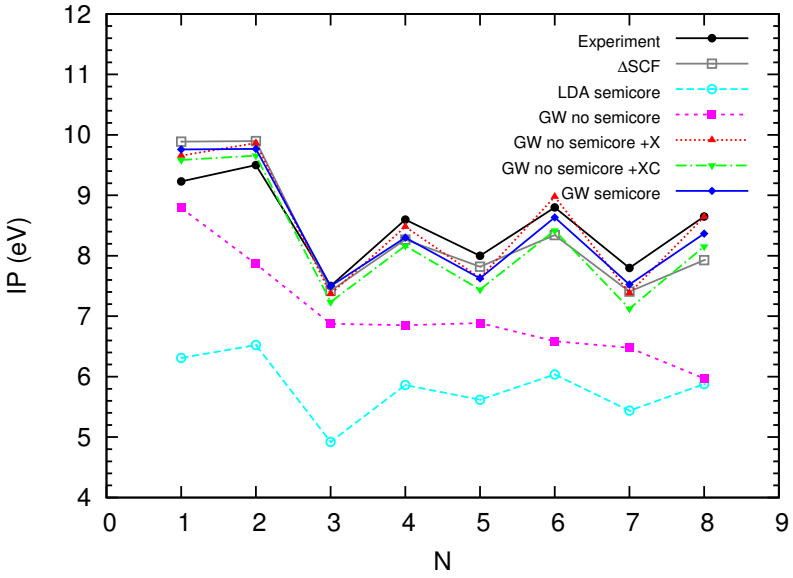

Figure 3.3: Vertical ionization potentials for the lowest energy structure at each cluster size of Au_N ($N = 1 - 8$), calculated from: DFT-LDA with Au semicore states in valance (LDA semicore), GW without Au semicore states in valence (GW no semicore), GW without Au semicore states in valence and with the exchange correction to the self-energy (GW no semicore +X), GW without Au semicore states in valence and with both the exchange and the correlation corrections to the self-energy (GW no semicore +XC), GW with Au semicore states in valence (GW semicore), and ΔSCF with Au semicore states in valence (ΔSCF). The calculated results are compared with the experimental values (Experiment).

In Fig. [3.3], we plot the IPs calculated at different levels of theory for the lowest energy structure at each cluster size, and compare them with experiment. Again, we see that while the DFT-LDA and

[4]Note that there is two-fold degeneracy in the LDA HOMO-1 states.

GW no semicore calculations often severely underestimate the experimental IPs, the GW semicore and $\Delta\mathrm{SCF}$ calculations give results that are in good agreement with experiment, with the GW semicore results generally agreeing better with the experimental values than the $\Delta\mathrm{SCF}$ results; by using our simplified scheme to account for the semicore effects, the GW semicore results are well reproduced by the GW no semciore +X and GW no semicore +XC calculations, with the GW no semicore +XC curve being almost a small constant shift down of the GW semicore one. Even-odd oscillations are found for all the IP curves except for the GW no semicore one, with the IPs of the clusters with an even number of atoms larger than that of its odd-numbered neighbors. This oscillatory behavior can be explained by the electron spin-pairing effect: an electron in a spin-paired orbital (an orbital occupied/unoccupied by two electrons with different spins) feels a stronger effective core potential, due to the fact that the electron screening is weaker for electrons in the same orbital than inner-shell electrons. Since the orbitals of even-numbered neutral gold clusters are paired in spin, while those of odd-numbered ones are not, it is more difficult to remove an electron from an even-numbered neutral gold cluster, indicating that they are more stable than neighboring odd-numbered ones. The GW no semicore curve does not show any obvious oscillatory behavior. This is because on the one hand, the IPs calculated at the GW no semicore level are not the correct GW IPs; on the other hand, the GW no semicore HOMO state often does not correspond to the GW semicore one, which should be the correct HOMO state at the GW level.

In Fig. [3.4], we display the exchange term of the self-energy for the state that corresponds to the GW semicore HOMO state, calculated at different levels of GW theory, for the lowest energy structure at each cluster size. The exchange term at the GW no semicore +X or GW no semicore +XC level is the same as that at the GW semicore level, thus is not plotted separately. Compared with the GW semicore calculations, the GW no semicore calculations severely underestimate the exchange contribution to the self-energy, due to the neglect of the semicore effects. The only exception is in the case of the Au atom, where good agreement is found between the GW no semicore and GW semicore results. This is due to the fact that the LDA HOMO state to which the GW quasiparticle energy correction is applied has almost no contribution from the Au 5d states, thus its exchange term is not affected much by the presence or not of the Au semicore 5s and 5p states in the valence. Even-odd oscillations are also found for the exchange term of the self-energy, with the values for even-numbered clusters smaller than those for neighboring odd-numbered ones. This is because the electrons in a spin-paired orbital feel a stronger effective core potential, so that their orbitals are more localized compared with those in non spin-paired cases. As a result, the overlaps of the orbitals of even-numbered clusters are larger than those of odd-numbered ones, leading to a smaller value of the exchange term. In the size range $\mathrm{N} = 1 - 8$, both the magnitudes and the oscillation amplitudes of the exchange have the tendency of increasing with the cluster size.

In Fig. [3.5], we display the correlation term of the self-energy for the state that corresponds to the GW semicore HOMO state, calculated at different levels of GW theory, for the lowest energy

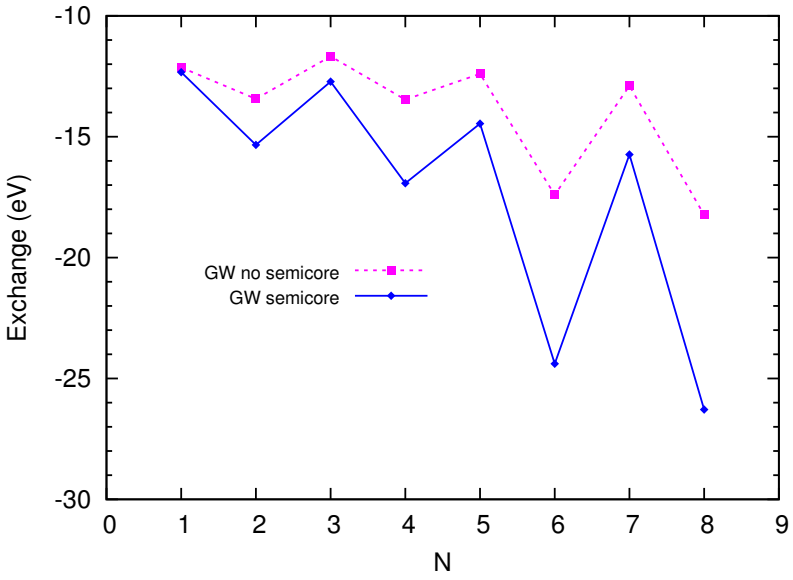

Figure 3.4: Dependence of the exchange term of the self-energy as a function of the cluster size N, calculated from GW without Au semicore states in valence (GW no semicore), and GW with Au semicore states in valence (GW semicore), for the lowest energy structure at each cluster size of Au_N ($N = 1 - 8$). All calculated energies correspond to the HOMO levels of the GW semicore calculations.

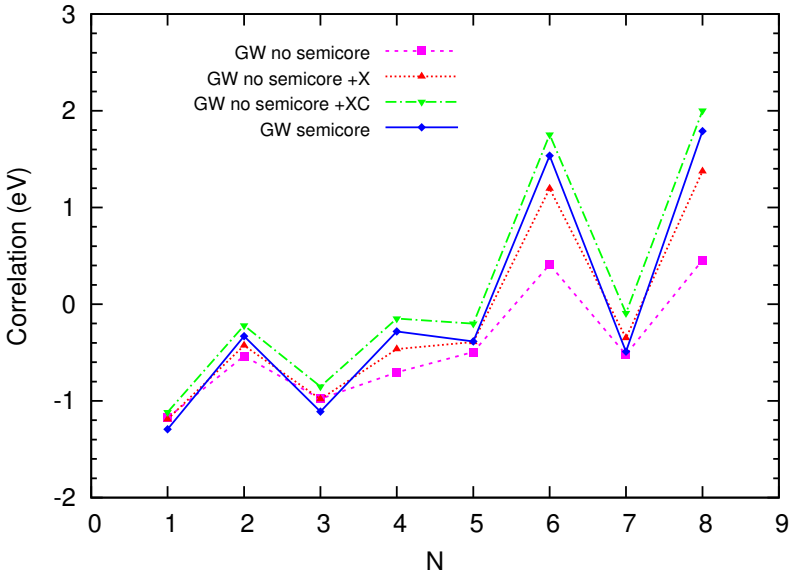

Figure 3.5: Dependence of the correlation term of the self-energy as a function of the cluster size N, calculated from GW without Au semicore states in valence (GW no semicore), GW without Au semicore states in valence and with the exchange correction to the self-energy (GW no semicore +X), GW without Au semicore states in valence and with both the exchange and the correlation corrections to the self-energy (GW no semicore +XC), and GW with Au semicore states in valence (GW semicore), for the lowest energy structure at each cluster size of Au_N ($N = 1 - 8$). All calculated energies correspond to the HOMO levels of the GW semicore calculations.

structure at each cluster size. In contrast to the behavior of the exchange term, the correlation term calculated at the GW no semicore level agrees much better with that calculated at the GW semicore level. This is as expected, since the semicore effects influence mainly to the exchange term and should not affect much the correlation one. With our simplified scheme to account for the semicore effects, the GW no semicore +X and GW no semicore +XC calculations reproduce well the correlation term calculated at the GW semicore level. In addition, the GW no semicore +XC curve is almost a small constant shift up of the GW semicore one. Even-odd oscillations are found again, for the correlation term of the self-energy. Differently from the exchange term, the correlation term oscillates in an opposite direction, with the value for an even-numbered cluster in most cases larger than those of neighboring odd-numbered ones. In the size range $\mathrm{N} = 1 - 8$, similarly to the case of the exchange, both the magnitudes and the oscillation amplitudes of the correlation have the tendency of increasing with the cluster size.

3.2.4 Electron Affinities

In Table. [3.3], we compare the (vertical) EAs of $\mathrm{Au_N}$ ($\mathrm{N} = 1 - 8$) calculated at different levels of theory. For the Au atom, the calculated EAs are also compared with experiment, while for the other clusters, no experimental EA values are available for comparison. For the EA of the Au atom, the experimental value of 2.31 eV is best reproduced by the $\Delta\mathrm{SCF}$ result of 2.63 eV, and reasonably well reproduced by the different GW ones, but is severely overestimated by the LDA one of 5.77 eV. For each multi-atomic structure, DFT-LDA also overestimates the EA calculated from $\Delta\mathrm{SCF}$, which is supposed to be a good first reference value. The EAs calculated at different levels of GW theory generally agree well with each other. This is because the empty states responsible for the EAs have very little, if any, Au 5d character, so that the corresponding quasiparticle energies are hardly affected by any semicore effects. However, compared with the $\Delta\mathrm{SCF}$ results, the calculated EAs are systematically larger at the different levels of GW theory. This is to be expected, since at the DFT level, the low-lying empty states for small neutral gold clusters are weakly bounded, thus are usually not good starting points in GW calculations for the evaluation of the corresponding quasiparticle energies, including the calculation of the EAs. Therefore, for the GW calculations of small neutral gold clusters, we do not expect a quality for the EAs as good as that for the IPs. We think that the quality may be improved if some degree of self-consistency is added in the GW calculations.

There are also a few cases where energy level crossing occurs to the GW LUMO state, but the crossing energy (in this sense the difference between the GW quasiparticle energy correction for the GW LUMO state and that for the LDA LUMO state) is in a much smaller scale than that for the GW HOMO state, and in any case is smaller than 0.4 eV. At all four levels of GW theory, the GW HOMO states always correspond to the same state. The only exception is for the $\mathrm{Au_3}$ cluster with the 3b structure, where although the GW no semicore HOMO sate corresponds to the LDA HOMO state in the open-shell that is treated as fully occupied in the GW calculation, the GW no semicore+X, GW

Table 3.3: Vertical electron affinities for different structures of $\mathrm{Au_N}$ ($\mathrm{N} = 1 - 8$), calculated from: DFT-LDA with Au semicore states in valance (LDA), GW without Au semicore states in valence ($\mathrm{GW_{nsc}}$), GW without Au semicore states in valence and with the exchange correction to the self-energy ($\mathrm{GW_{sc}^{X}}$), GW without Au semicore states in valence and with both the exchange and the correlation corrections to the self-energy ($\mathrm{GW_{sc}^{XC}}$), GW with Au semicore states in valence ($\mathrm{GW_{sc}}$), and $\Delta\mathrm{SCF}$ with Au semicore states in valence ($\Delta\mathrm{SCF}$). The calculated electron affinities for the Au atom are also compared with experiment. All energies are in eV.

Cluster	LDA	$\mathrm{GW_{nsc}}$	$\mathrm{GW_{sc}^{X}}$	$\mathrm{GW_{sc}^{XC}}$	$\mathrm{GW_{sc}}$	$\Delta\mathrm{SCF}$	Expt [120]
1	5.77	3.24	2.92	2.88	2.78	2.63	2.31
2	4.59	2.75	2.51	2.42	2.70	2.08	
3a	4.88	2.93	2.88	2.75	2.95	2.34	
3b	4.91	3.17	3.13	3.01	3.21	2.36	
3c	6.01	3.81	4.45	4.21	4.39	3.57	
3d	6.39	4.69	4.57	4.48	4.58	4.00	
4a	4.88	2.96	3.11	2.96	3.23	2.68	
4b	4.95	3.26	3.38	3.24	3.47	2.82	
5	5.37	3.57	3.98	3.77	3.88	3.29	
6	4.08	2.85	2.81	2.67	2.94	2.28	
7a	5.25	3.58	4.17	3.91	3.81	3.38	
7b	4.96	3.49	3.54	3.39	3.61	2.99	
7c	5.56	4.04	4.28	4.10	4.03	3.68	
8	4.69	3.34	3.41	3.25	3.47	2.99	

no semicore+XC and GW semicore HOMO states all correspond to one of the two-fold degenerate LDA LUMO states of the minority spin channel[5].

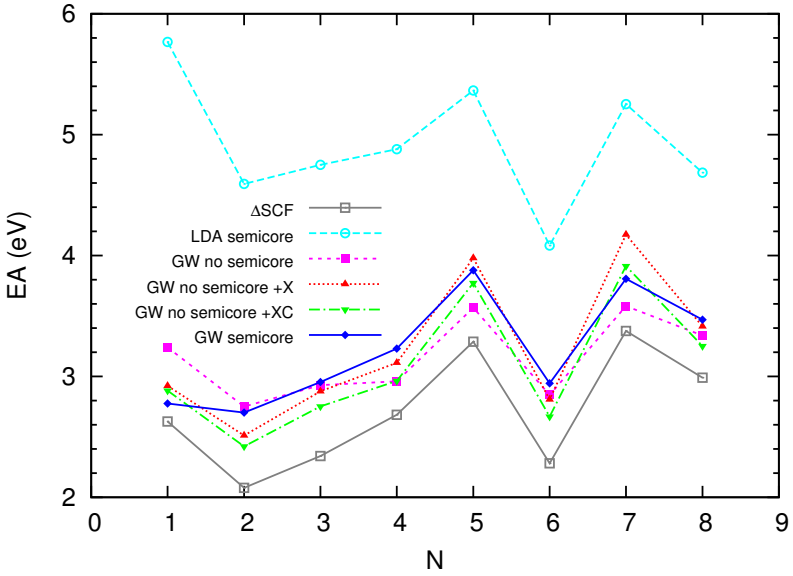

Figure 3.6: Vertical electron affinities for the lowest energy structure at each cluster size of Au_N ($N = 1 - 8$), calculated from: DFT-LDA with Au semicore states in valance (LDA semicore), GW without Au semicore states in valence (GW no semicore), GW without Au semicore states in valence and with the exchange correction to the self-energy (GW no semicore +X), GW without Au semicore states in valence and with both the exchange and the correlation corrections to the self-energy (GW no semicore +XC), GW with Au semicore states in valence (GW semicore), and ΔSCF with Au semicore states in valence (ΔSCF).

In Fig. [3.6], we compare the EAs calculated at different levels of theory for the lowest energy structure at each cluster size. Again, we find that the ΔSCF results are severely overestimated by the LDA ones; the EAs calculated at different levels of GW theory agree well with each other, but systematically overestimate those calculated from ΔSCF. There are even-odd oscillations in the size range $N = 1 - 3$ and $N = 5 - 8$ for all the EA curves, with the direction of the oscillations opposite with respect to that for the IPs in Fig. [3.3]. The oscillations indicate that odd-numbered neutral gold clusters are more willing to accept one more electron, so as to become more stable by making its orbitals paired in spin. The oscillation amplitudes of the calculated EAs are smaller than those of the calculated IPs in Fig. [3.3]. The magnitudes of the calculated EAs have the tendency of increasing with the cluster size.

In Fig. [3.7], we display the exchange term of the self-energy for the state that corresponds to the GW semicore LUMO state, calculated at different levels of GW theory, for the lowest energy structure at each cluster size. For the exchange term, the differences between the GW no semicore and GW semicore curves are much smaller than those in Fig. [3.4], due to the fact that the semicore

[5]The two-fold degeneracy in the energy levels is broke by our compromised GW scheme for open-shell molecules.

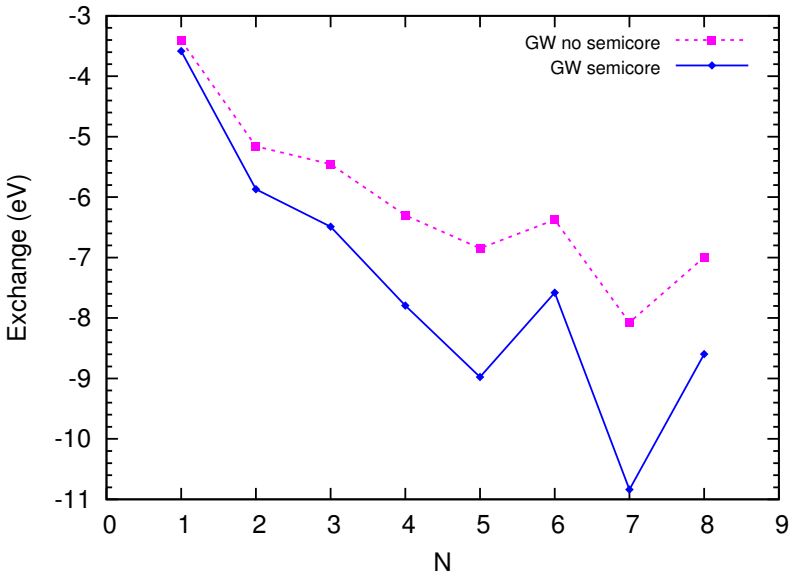

Figure 3.7: Dependence of the exchange term of the self-energy as a function of the cluster size N, calculated from GW without Au semicore states in valence (GW no semicore), and GW with Au semicore states in valence (GW semicore), for the lowest energy structure at each cluster size of Au_N ($N = 1 - 8$). All calculated energies correspond to the LUMO levels of the GW semicore calculations.

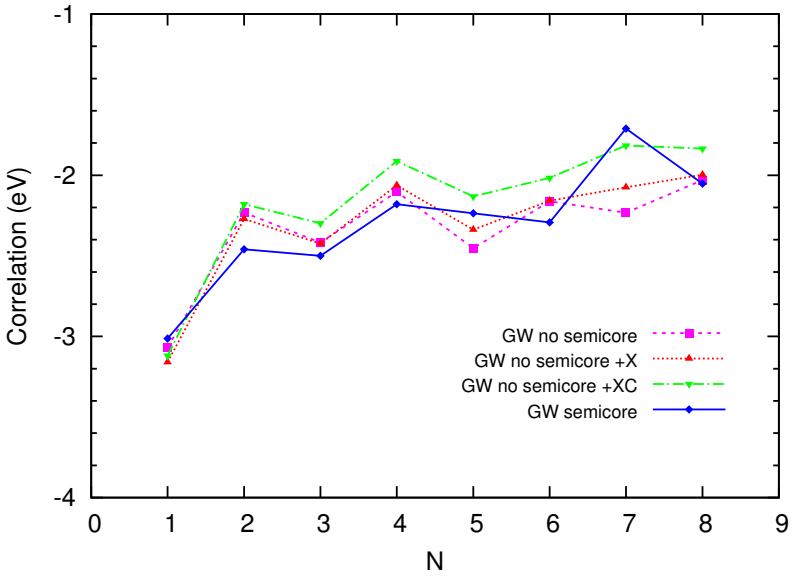

Figure 3.8: Dependence of the correlation term of the self-energy as a function of the cluster size N, calculated from GW without Au semicore states in valence (GW no semicore), GW without Au semicore states in valence and with the exchange correction to the self-energy (GW no semicore +X), GW without Au semicore states in valence and with both the exchange and the correlation corrections to the self-energy (GW no semicore +XC), and GW with Au semicore states in valence (GW semicore), for the lowest energy structure at each cluster size of Au_N ($N = 1 - 8$). All calculated energies correspond to the LUMO levels of the GW semicore calculations.

effects do not affect that much the exchange energies for empty states. Even-odd oscillations due to the electron spin-paring effect exist for both curves in the size range $\mathrm{N} = 4 - 8$. The oscillation direction is opposite with respect to those in Fig. [3.4], and the oscillation amplitudes are correspondingly smaller. Both the magnitudes and the oscillation amplitudes of the exchange have the tendency of increasing with the cluster size.

In Fig. [3.8], we display the correlation term of the self-energy for the state that corresponds to the GW semicore LUMO state, calculated at different levels of GW theory, for the lowest energy structure at each cluster size. Good agreement is found between the results calculated at different levels of GW theory, due to the fact that the semicore effects do not influence much the correlation term of the self-energy. Some even-odd oscillations exist for all the four curves, with the oscillation amplitudes smaller than those in Fig. [3.5]. The magnitudes of the correlation have the tendency of decreasing as the cluster size increases.

3.2.5 Electronic Densities of States

In Figs. [3.9]-[3.22], we display the electronic density of states (DOS) calculated at the LDA level or the GW semicore level, for each considered structure of $\mathrm{Au_N}$ ($\mathrm{N} = 1 - 8$). The corresponding projected density of states (PDOS) from the Au 5d, 6s or 6p states is also plotted. In Appendix A, we also present the DOS spectrum and the corresponding PDOS spectra calculated at the GW no semicore level and those calculated by using our simplified scheme to account for the effects of the Au semicore 5s and 5p states, and compare them with those calculated at the LDA and GW semicore levels. We do not compare the calculated DOS spectra with experiment, since it is difficult to perform photoemission experiments for neutral gold clusters and the corresponding experimental spectra are unavailable at this moment.

For each structure, the LDA DOS spectrum is in general quit different from the GW semicore one, particularly concerning the peak positions. However, there are some similarities between the shape of the DOS spectrum at the LDA level and that at the GW semicore level, often in the lowest and highest energy valence parts and the lowest energy conduction part. Most major differences are usually present in the middle energy parts of the valence DOS spectra. It can be seen that DFT-LDA calculations can provide some useful information about the quasiparticle spectra, especially considering the spectrum shapes, but they are evidently incapable of predicting the absolute peak positions, for which GW calculations would be needed. We see that for $\mathrm{Au_3}$, $\mathrm{Au_4}$ and $\mathrm{Au_7}$, although the calculated total energies are close between the different structures at the same cluster size, the calculated DOS spectra always display major differences in peak numbers, shapes or positions. The different characters in the GW DOS spectra can help to identify the ground-state structures once the corresponding experimental photoemission spectra become available.

For each structure, the HOMO-LUMO gap is small at the LDA level, but is opened largely at the GW semicore level. At the LDA level, the calculated HOMO-LUMO gap for an odd-numbered

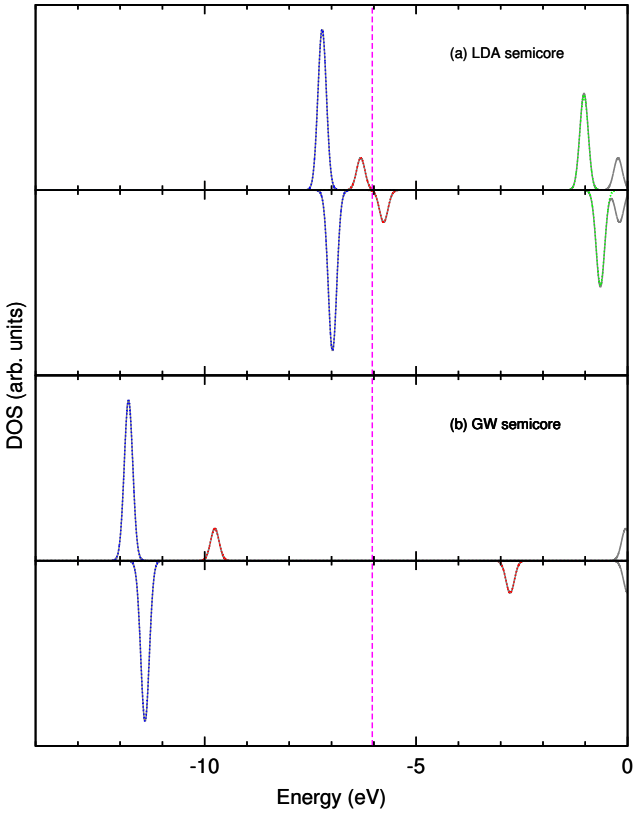

Figure 3.9: Electronic densities of states for the Au atom, calculated from: (a) DFT-LDA with Au semicore states in valence (upper half of the figure), (b) GW with Au semicore states in valence (lower half of the figure). In subfigure (a) or (b), the upper/lower half is for the majority/minority spin channel. For each spin channel, the projected density of states from the Au 5d (blue), 6s (red) or 6p (green) states is plotted together with the total density of states (gray). The dashed magenta line represents the Fermi level for the LDA semicore calculation. A Gaussian broadening of 0.1 eV has been used.

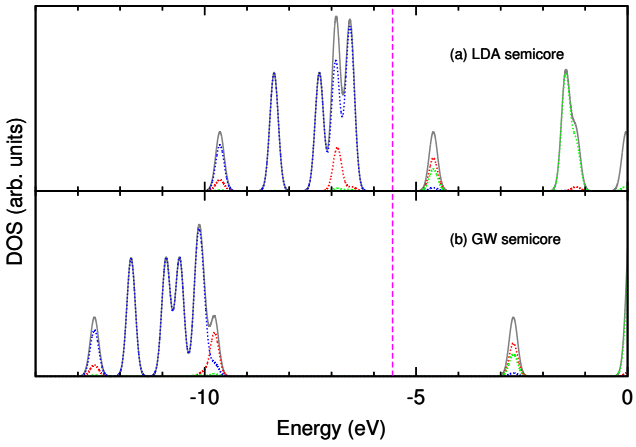

Figure 3.10: Electronic densities of states for Au_2, calculated from: (a) DFT-LDA with Au semicore states in valence, (b) GW with Au semicore states in valence. In each subfigure, the projected density of states from the Au 5d (blue), 6s (red) or 6p (green) states is plotted together with the total density of states (gray). The dashed magenta line represents the Fermi level for the LDA semicore calculation. A Gaussian broadening of 0.1 eV has been used.

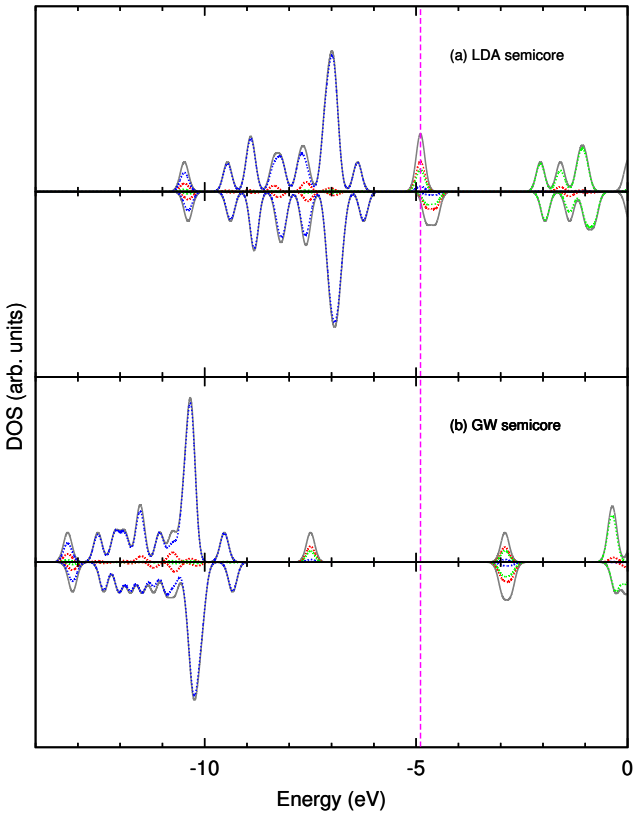

Figure 3.11: Electronic densities of states for the 3a structure of Au_3. The different lines in this figure have the same meaning as those in Fig. [3.9].

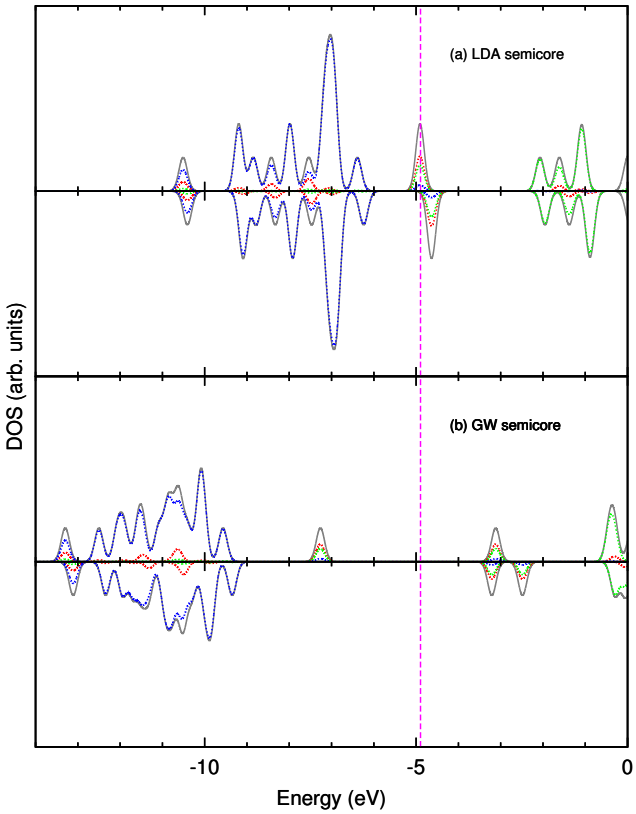

Figure 3.12: Electronic densities of states for the 3b structure of Au_3. The different lines in this figure have the same meaning as those in Fig. [3.9].

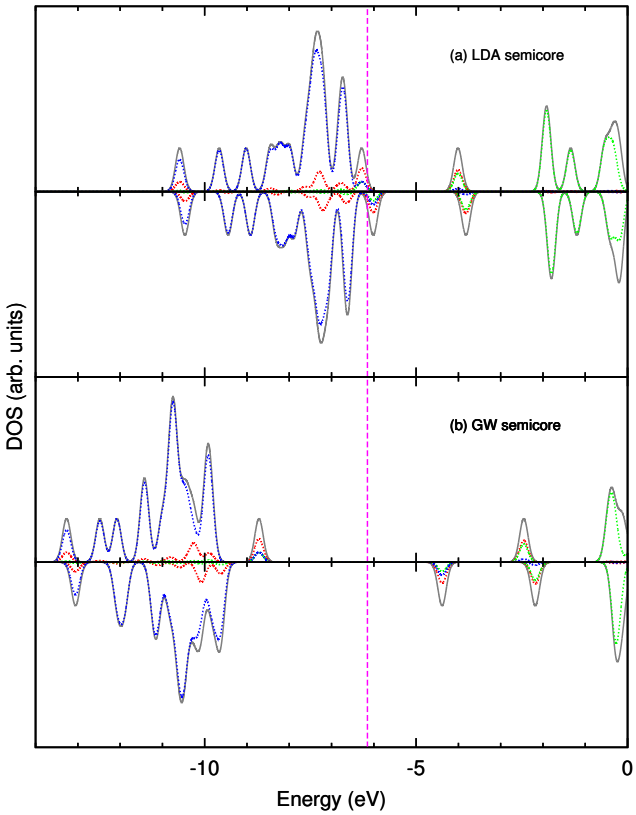

Figure 3.13: Electronic densities of states for the 3c structure of Au_3. The different lines in this figure have the same meaning as those in Fig. [3.9].

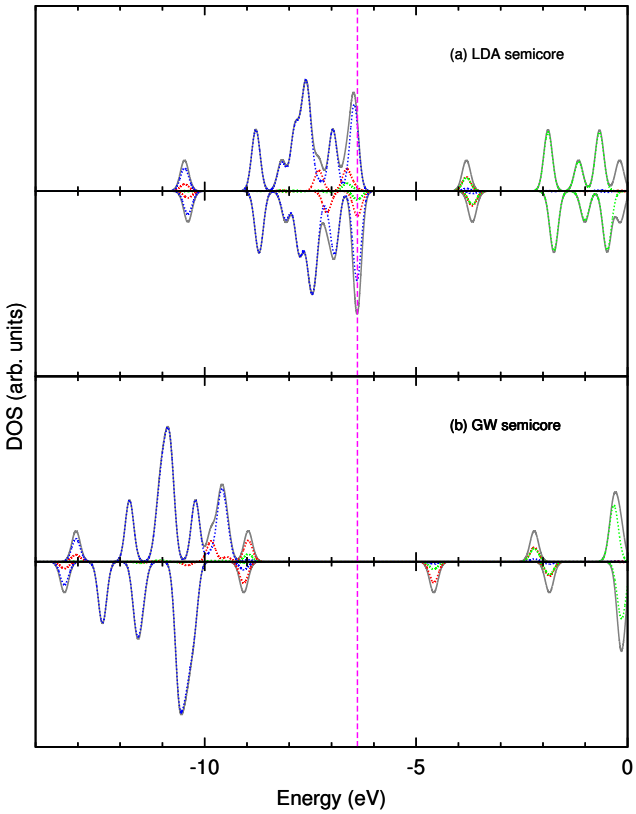

Figure 3.14: Electronic densities of states for the 3d structure of Au_3. The different lines in this figure have the same meaning as those in Fig. [3.9].

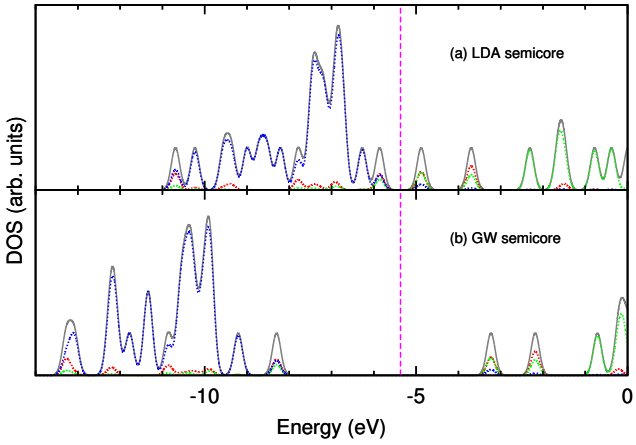

Figure 3.15: Electronic densities of states for the 4a structure of Au_4. The different lines in this figure have the same meaning as those in Fig. [3.10].

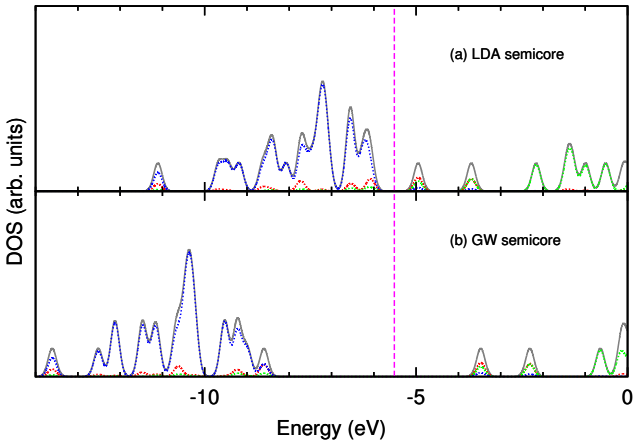

Figure 3.16: Electronic densities of states for the 4b structure of Au_4. The different lines in this figure have the same meaning as those in Fig. [3.10].

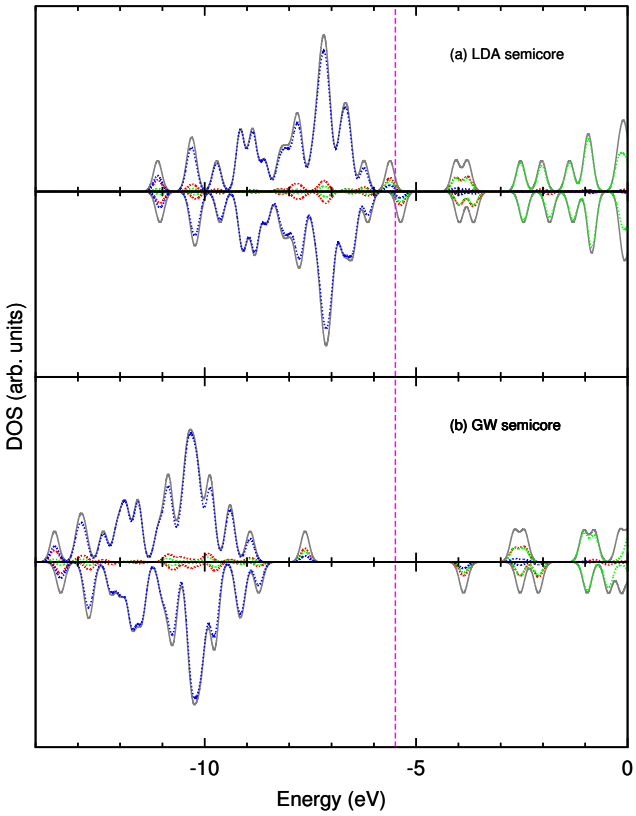

Figure 3.17: Electronic densities of states for Au_5. The different lines in this figure have the same meaning as those in Fig. [3.9].

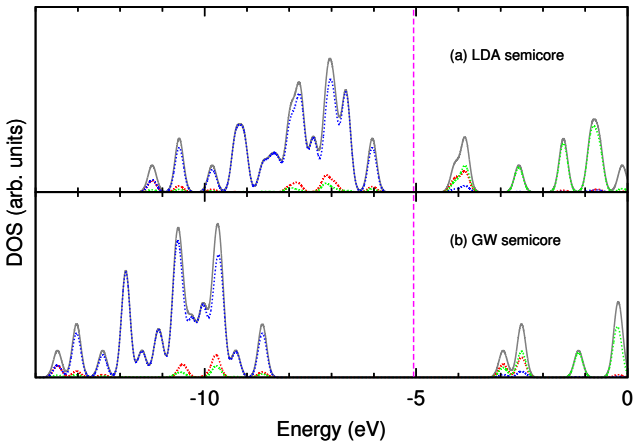

Figure 3.18: Electronic densities of states for Au_6. The different lines in this figure have the same meaning as those in Fig. [3.10].

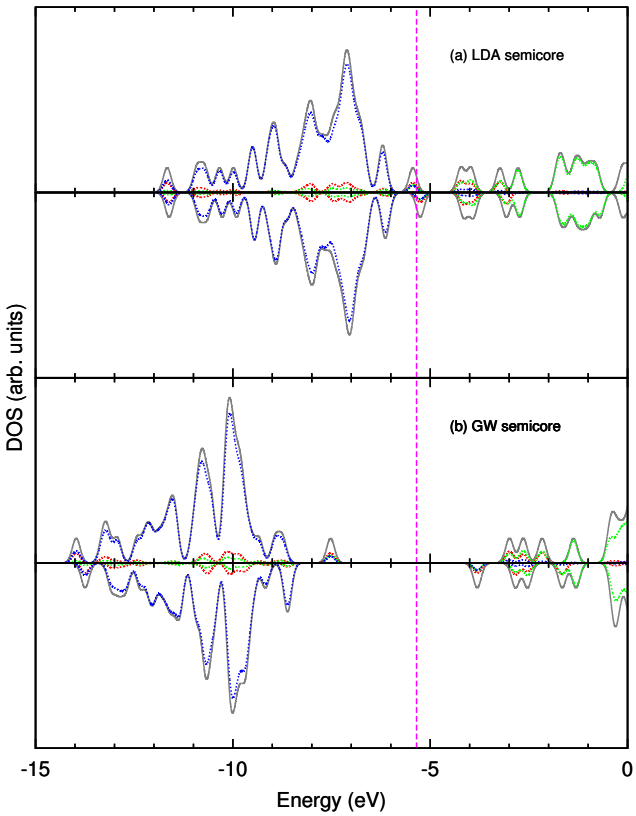

Figure 3.19: Electronic densities of states for the 7a structure of Au_7. The different lines in this figure have the same meaning as those in Fig. [3.9].

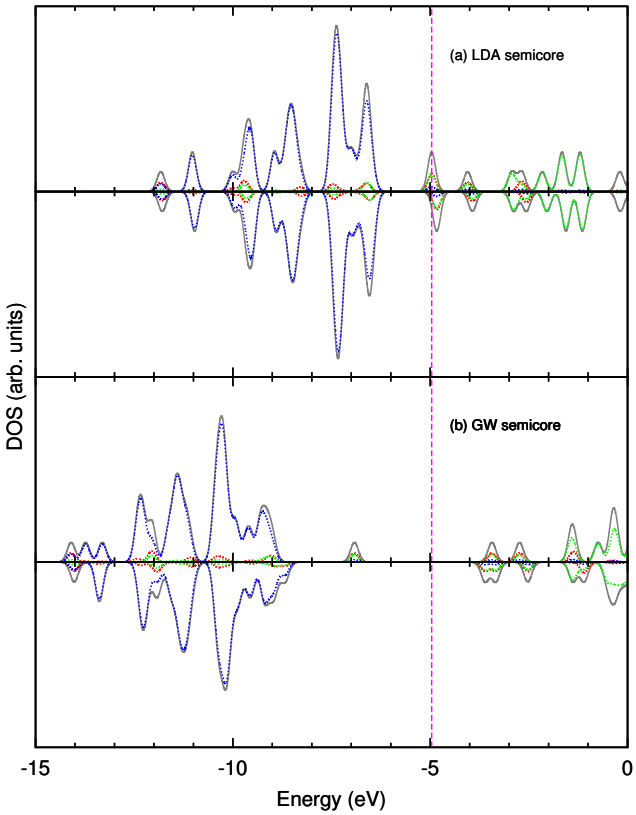

Figure 3.20: Electronic densities of states for the 7b structure of Au_7. The different lines in this figure have the same meaning as those in Fig. [3.9].

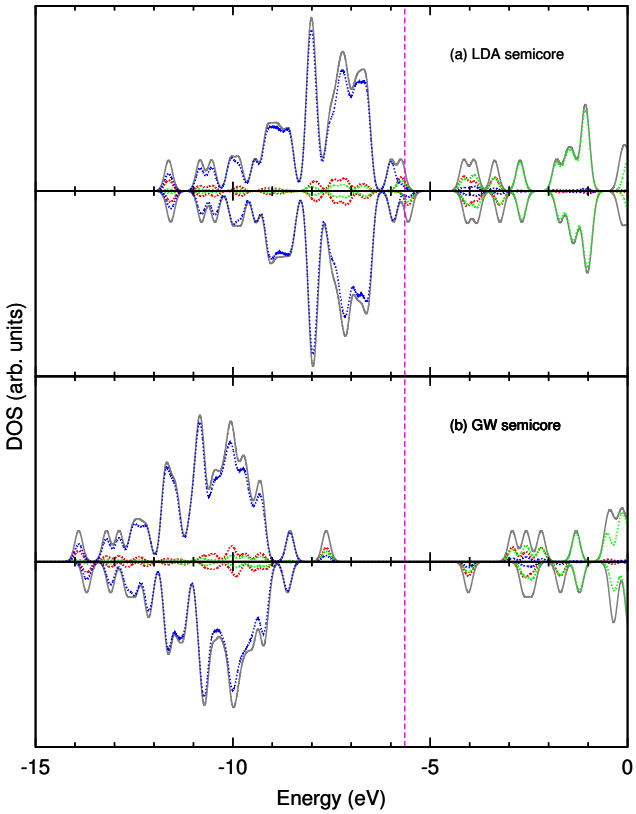

Figure 3.21: Electronic densities of states for the 7c structure of Au_7. The different lines in this figure have the same meaning as those in Fig. [3.9].

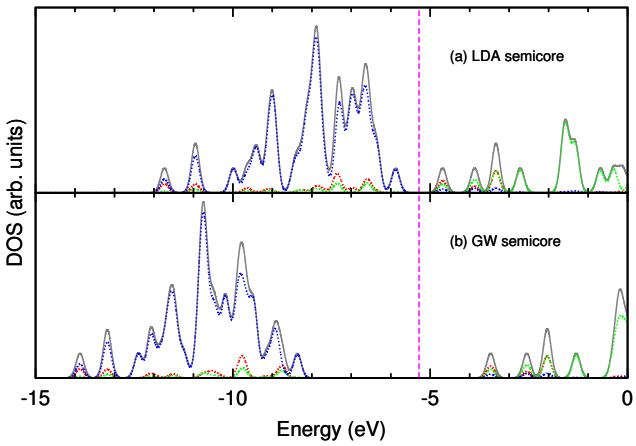

Figure 3.22: Electronic densities of states for Au_8. The different lines in this figure have the same meaning as those in Fig. [3.10].

cluster is in general much smaller than that for an even-numbered one. In a few cases, the LDA HOMO-LUMO gap is very small or even zero. In particular, it is zero for the 3b structure of Au_3 and the 7b structure of Au_7, is only 0.04 eV for the 3a structure of Au_3, and is within 1 meV (thus is almost zero) for the 3d structure of Au_3. The HOMO-LUMO gap does not show in the DOS spectrum when it is smaller than the Gaussian broadening used to smear the calculated spectrum.

For an odd-numbered cluster, at the LDA level, the shape of the DOS spectrum for the majority spin channel is almost the same as that for the minority spin channel, with the DOS spectrum for the majority spin channel displaced a little bit to the lower energy direction. The same thing happens at the GW semicore level, but there is the difference that the HOMO peak, which is in the majority spin channel, is well separated from the LUMO peak (for the 3a structure of Au_3, the peak that contains the LUMO), which is in the minority spin channel. At the GW semicore level, the only exception is for the 3d structure of Au_3, where the shape of the valence DOS spectrum for the majority spin channel in $\sim [-11.5, -9.3]$ eV differs significantly from that for the minority spin channel in $\sim [-12, -10]$ eV, and the HOMO peak is in the majority spin channel while the LUMO peak is in the minority spin channel. In this case, by using our GW scheme for open-shell molecules to treat the fractionally occupied HOMO and LUMO, which are more localized compared with the fractionally occupied HOMOs for the 3b structure of Au_3 and the 7b structure of Au_7, the change in the electronic configuration breaks partly the similarities in the shapes of the DOS spectra between the two spin channels.

Inspection of the PDOS spectra indicates a strong Au 5d character for the valence states, thus confirming the importance of a proper account of the Au semicore 5s and 5p contributions to the electron self-energy operator. The strong s-d hybridization found for each considered structure of Au_N ($N = 2 - 8$) has been attributed to the strong relativistic effects in gold, and is believed to be responsible for the enhanced stabilities in planar structures of small gold clusters [37, 38]. For each structure, both the HOMO and LUMO peaks (or the peaks that contain the HOMO or the LUMO) have strong or non-negligible contributions from the Au 6s states. In particular, the HOMO and

LUMO peaks for the Au atom are formed solely by the Au 6s states. The only exceptions are for the highest-lying valence peak for Au_2 at the LDA level, the HOMO peaks for Au_6 and Au_8 at both the LDA and GW semicore levels. In these cases the peaks are mainly of 5d character and have very little contribution (in the cases of Au_2 and Au_6) or almost no contribution (in the case of Au_8) from the Au 6s states. In the case of Au_2, after applying the GW quasiparticle energy corrections, the LDA HOMO state and the two-fold degenerate LDA HOMO-1 states that give rise to the highest-lying valence peak at the LDA level do not contribute any more to the highest-lying valence peak at the GW semicore level (the GW semicore HOMO peak). At the GW semicore level, the HOMO peak is given by the LDA HOMO-2 state, which is mainly of 6s character. The energy crossing for the GW HOMO state here is due to the strong 5d character, which makes the LDA HOMO state and the LDA HOMO-1 states more sensitive to the GW quasiparticle energy corrections, so that their energies become lower than that of the neighboring LDA HOMO-2 state which has strong 6s character.

3.3 Electronic Properties of Au_{20} and Au_{32}

As mentioned before in this thesis, due to the strong relativistic effects in gold, small gold clusters favor planar structures even at relatively large cluster sizes. An extension to the tendency of small gold clusters to display planar structures is that larger gold clusters can have interesting quasi two-dimensional structures. For example, a hollow tetrahedral structure was found as the lowest energy structure for the neutral and anionic Au_{20} clusters [32]. The correctness of this finding has been confirmed by combined theoretical and experimental investigations [23, 32]. Another example is that DFT studies predicted that the lowest energy structure for the neutral and anionic Au_{32} clusters is an icosahedral cage [33, 34, 121]. Unlike other cagelike structures that have been reported, this structure is free-standing and does not contain any carbon atom. In addition, the neutral cagelike Au_{32} cluster can incorporate up to 3 gold atoms inside without being strongly deformed. However, it was found that this structure is not the most stable one observed for the anionic Au_{32} cluster in the photoemission experiment, due to the contribution from the vibrational entropy to the structural stability [121].

The common characteristics of the tetrahedral Au_{20} cluster and the cagelike Au_{32} cluster in the neutral or anionic state are that they all possess highly symmetric structures and are highly stable at least at the DFT level. Due to their high structural symmetry and high stability, they may have novel physical and chemical properties, which may lead to a wide range of potential applications in areas such as nanotechnology, catalysis, biology, medicine, and so on [6–17]. The understanding of their electronic properties is therefore particularly important for future applications.

In this section, we study the electronic properties of the tetrahedral Au_{20} cluster and the cagelike Au_{32} cluster in the neutral state. We have seen that the consideration of the Au semicore 5s and 5p

states is necessary for the accurate simulation of the quasiparticle spectra of gold clusters. However, the explicit inclusion of the semicore states in the valence requires more computational effort and is prohibitive for the relatively large Au_{20} and Au_{32} clusters. In this work, with our simplified GW scheme to account for the semicore effects, we are able to calculate the quasiparticle spectra for Au_{20} and Au_{32} by using moderate computational efforts without compromising much the computational accuracy.

3.3.1 Equilibrium Geometries

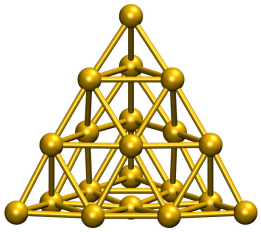

Figure 3.23: Equilibrium geometry for the tetrahedral Au_{20} cluster.

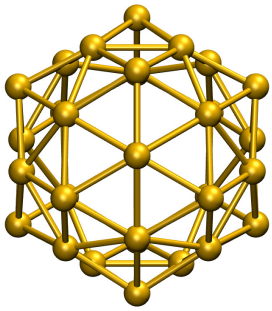

Figure 3.24: Equilibrium geometry for the cagelike Au_{32} cluster.

In Fig. [3.23] and Fig. [3.24], we display the equilibrium geometries optimized with DFT-LDA by using the Au.pz-d-rrkjus.UPF pseudopotential from the QE distribution, for the tetrahedral Au_{20} cluster and the cagelike Au_{32} cluster, respectively.

The tetrahedral Au_{20} cluster has T_d symmetry, with each of its face being an almost planar Au_{10} cluster with D_{3h} symmetry. Since this cluster has only surface atoms, it is actually a quasi two-dimensional cluster. There are three symmetry-independent sites on this cluster, 4 three-coordinated sites at the apexes (apex sites), 12 six-coordinated sites along the edges (edge sites), and 4 nine-coordinated sites at the centers of the faces (face sites). There are five different types of bonds, whose lengths are: 2.61 Å for a bond connecting two neighboring edge sites along the same edge, 2.63 Å for a bond connecting an apex site and its nearest neighboring edge sites, 2.73 Å for a bond

connecting a face site and its nearest neighboring edge sites, 2.84 Å for a bond connecting two nearest neighboring edge sites along different edges, and 3.01 Å for a bond connecting two face sites.

The cagelike icosahedral Au_{32} cluster has the same symmetry as C_{60} fullerene, i.e., the I_{h} symmetry. Its structure can be obtained by capping one atom on each pentagon of a dodecahedron. Since all the atoms lie on the surface of the cage without even a single one lying inside, this cluster is also a quasi two-dimensional cluster. There are two symmetry-independent sites on this cluster, 12 five-coordinated sites and 20 six-coordinated sites, and two different types of bonds, whose lengths are: 2.67 Å for the five-coordinated sites, and 2.74 Å for the six-coordinated sites.

3.3.2 Molecular Orbitals

In Fig. [3.25] and Fig. [3.26], we display the HOMOs and LUMOs calculated from DFT-LDA, for the tetrahedral Au_{20} cluster and the cagelike Au_{32} cluster. Due to the T_{d} symmetry of the structure, the Au_{20} cluster has fully-occupied two-fold degenerate HOMOs belonging to the irreducible representation E, and fully-unoccupied three-fold degenerate LUMOs belonging to the irreducible representation T_2. Due to the I_{h} symmetry of the structure, the Au_{32} cluster has fully-occupied four-fold degenerate HOMOs belonging to the irreducible representation G_{u}, and fully-unoccupied four-fold degenerate LUMOs belonging to the irreducible representation G_{g}. For Au_{20}, besides two-fold and three-fold degenerate states, there are also non-degenerate states. And for Au_{32}, besides four-fold degenerate states, there are also non-degenerate, three-fold degenerate and five-fold degenerate states.

3.3.3 Ionization Potentials and Electron Affinities

In Table. [3.4], we report the (vertical) IPs, the (vertical) EAs, and their differences calculated at different levels of theory, for the tetrahedral Au_{20} cluster and the cagelike Au_{32} cluster. The calculated IPs for Au_{20} are compared with experiment.

Similar patterns as in the cases of small gold clusters are found. For Au_{20}, the IPs calculated at the GW no semicore +X and GW no semicore +XC levels both agree well with the experimental value. For both clusters, the IPs calculated at the GW no semicore +X and GW no semicore +XC levels agree well with each other and both reproduce well the $\Delta\mathrm{SCF}$ results used as a reference, while those calculated at the LDA and GW no semicore levels severely underestimate the $\Delta\mathrm{SCF}$ results. As to the calculated EAs, we find again severe overestimation at the LDA level compared with the $\Delta\mathrm{SCF}$ results used as a first reference. In contrast to the cases of small gold clusters, the EAs calculated at the $\Delta\mathrm{SCF}$ level are well reproduced at all three levels of GW theory. The better agreement between the GW results and the $\Delta\mathrm{SCF}$ ones for Au_{20} and Au_{32} as compared with those for small neutral gold clusters is not surprising, since for larger gold clusters, such as Au_{20} and

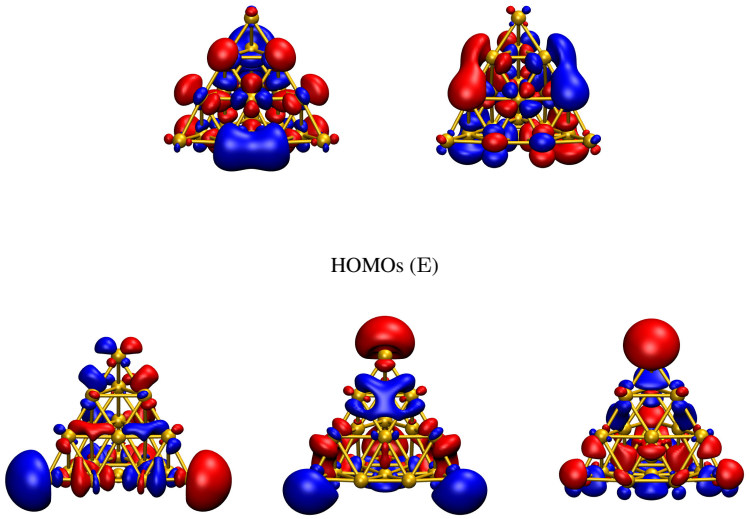

HOMOs (E)

LUMOs (T_2)

Figure 3.25: Fully-occupied degenerate HOMOs and fully-unoccupied degenerate LUMOs for the tetrahedral Au_{20} cluster. The corresponding irreducible representations are given in the parentheses.

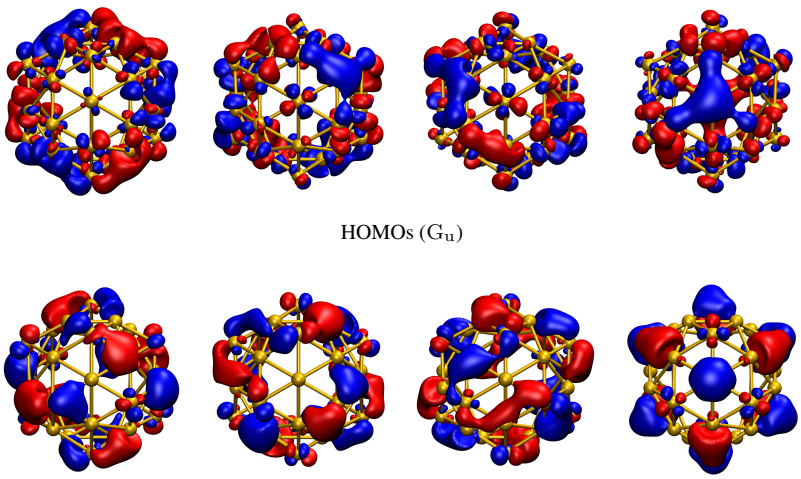

HOMOs (G_u)

LUMOs (G_g)

Figure 3.26: Fully-occupied degenerate HOMOs and fully-unoccupied degenerate LUMOs for the cagelike Au_{32} cluster. The corresponding irreducible representations are given in the parentheses.

Table 3.4: Vertical ionization potentials, vertical electron affinities, and their differences, for the tetrahedral Au_{20} cluster and the cagelike Au_{32} cluster, calculated from: DFT-LDA with Au semicore states in valance (LDA), GW without Au semicore states in valence (GW_{nsc}), GW without Au semicore states in valence and with the exchange correction to the self-energy (GW_{sc}^{X}), GW without Au semicore states in valence and with both the exchange and the correlation corrections to the self-energy (GW_{sc}^{XC}), and ΔSCF with Au semicore states in valence (ΔSCF). The calculated ionization potentials for Au_{20} are compared with experiment. All energies are in eV.

Cluster	Energy	LDA	GW_{nsc}	GW_{sc}^{X}	GW_{sc}^{XC}	ΔSCF	Expt [19]
Au_{20}	IP	5.98	6.08	7.92	7.51	7.48	7.82
	EA	4.25	3.01	3.16	2.98	2.88	
	IP-EA	1.73	3.07	4.76	4.53	4.60	
Au_{32}	IP	6.11	5.56	7.56	7.18	7.42	
	EA	4.58	3.52	3.53	3.30	3.31	
	IP-EA	1.53	2.04	4.03	3.88	4.11	

Au_{32}, the low-lying empty states are not that weakly bounded, thus can possibly be good starting points for the GW calculations of the corresponding quasiparticle energies.

Energy level crossings are also found for the GW HOMO and LUMO states of Au_{20} and Au_{32}: for Au_{20}, the GW no semicore HOMO states correspond to the three-fold degenerate LDA HOMO-2 states[6], with a crossing energy of 0.78 eV; for Au_{32}, the GW no semicore HOMO states correspond to the three-fold degenerate LDA HOMO-1 states, with a crossing energy of 0.94 eV, and the GW no semicore +X LUMO states correspond to the five-fold degenerate LDA LUMO+1 states, with a small crossing energy of 0.38 eV.

For each cluster, the HOMO-LUMO gap, which is calculated as the difference between the IP and the EA, is severely underestimated at the LDA and GW no semicore levels compared with the ΔSCF result used as a first reference. The GW no semicore +X and GW no semicore +XC calculations open the LDA and GW no semicore HOMO-LUMO gaps and give results that are both in good agreement with the ΔSCF one. It is worth noticing that the HOMO-LUMO gaps calculated at the GW no semicore +X, GW no semicore +XC and ΔSCF levels are very large and much larger than that calculated at the LDA level, further supporting that both clusters are highly stable.

3.3.4 Electronic Densities of States

In Fig. [3.27] and Fig. [3.28], we display the DOS calculated at different levels of theory for the tetrahedral Au_{20} cluster and the cagelike Au_{32} cluster, respectively. The corresponding PDOS from the Au 5d, 6s or 6p states is also plotted.

[6]Note that the LDA HOMO-1 states are three-fold degenerate.

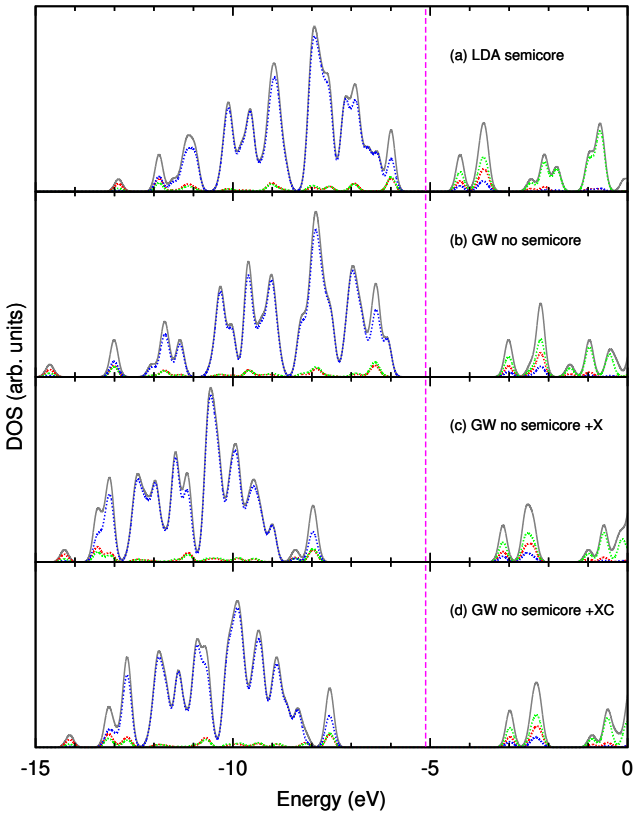

Figure 3.27: Electronic densities of states for the tetrahedral Au_{20} cluster, calculated from: (a) DFT-LDA with Au semicore states in valence, (b) GW without Au semicore states in valence, (c) GW without Au semicore states in valence and with the exchange correction to the self-energy, (d) GW without Au semicore states in valence and with both the exchange and the correlation corrections to the self-energy. In each subfigure, the projected density of states from the Au 5d (blue), 6s (red) or 6p (green) states is plotted together with the total density of states (gray). The dashed magenta line represents the Fermi level for the LDA semicore calculation. A Gaussian broadening of 0.1 eV has been used.

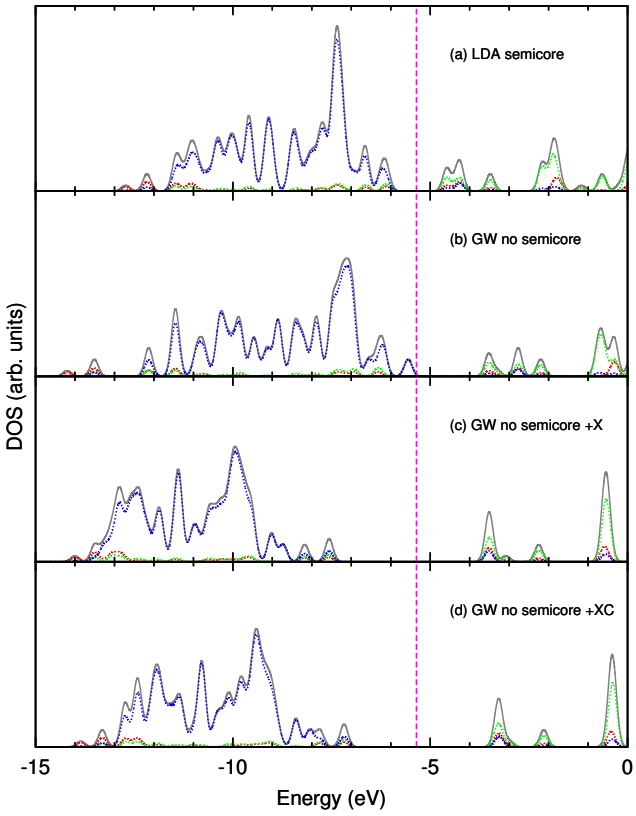

Figure 3.28: Electronic densities of states for the cagelike Au_{32} cluster. The different lines in this figure have the same meaning as those in Fig. [3.27].

Similar patterns as in the cases of small gold clusters are found. For each cluster, the LDA and GW no semicore DOS spectra are in general quit different from the GW no semicore +X and GW no semicore +XC ones, particularly concerning the peak positions. The GW no semicore +X and GW no semicore +XC calculations do not only produce DOS spectra that are in good agreement with each other, especially in the conduction parts, but also open the HOMO-LUMO gap compared with the DFT-LDA and GW no semicore calculations. Note that the GW no semicore +XC DOS spectrum is the best quasiparticle spectrum we have for each cluster. We do not compare the calculated DOS spectra with experiment, since the corresponding experimental photoemission spectra are unfortunately not available at this moment. From the PDOS spectra, we see that there is large contribution from the Au 5d states to the valence part of each DOS spectrum, but not to the conduction part. This indicates why the valence part of the GW DOS spectrum depends sensitively on the Au semicore 5s and 5p states, but the conduction part does not. In addition, strong s-d hybridization, which comes from the strong relativistic effects responsible for the stability of these two quasi two-dimensional clusters, is observed in the valence part of each DOS spectrum.

For Au_{20}, although the peak positions of the DOS spectrum at the LDA level do not agree with those at the GW no semicore +XC level (the level which gives the best theoretical quasiparticle spectrum here), there are some similarities in the shapes of the DOS spectra. The shapes are close between the valence DOS spectrum at the LDA level in $\sim [-13.2, -8.4]\ \mathrm{eV}$ and that at the GW no semicore +XC level in $\sim [-14.4, -10.4]\ \mathrm{eV}$, between the highest-lying valence DOS peak at the LDA level and that at the GW no semicore +XC level, and between the first four low-lying conduction DOS peaks at the LDA level and those at the GW no semicore +XC level. Similarities are also present in the shapes of the corresponding PDOS spectra. Moreover, the highest-lying valence DOS peak at the LDA level have non-negligible contributions from the Au 6s and 6p states similar to that at the GW no semicore +XC level, and the same thing happens to the first two low-lying conduction DOS peaks at the LDA and GW no semicore +XC levels. Major differences in the shapes are found between the DOS valence spectrum at the LDA level in $\sim [-8.4, -6.2]\ \mathrm{eV}$ and that at the GW no semicore +XC level in $\sim [-10.4, -7.8]\ \mathrm{eV}$.

For Au_{32}, the shapes are similar between the first four low-lying valence DOS peaks at the LDA level and those at the GW no semicore +XC level, with similarities also found for the corresponding PDOS spectra. The highest-lying valence DOS peak at the LDA level is larger than that at the GW no semicore +XC level, but they both possess similar non-negligible 6s and 6p character. The conduction DOS spectrum at the LDA level is similar to that at the GW no semicore +XC level, but the first two low-lying conduction DOS peaks merge into one peak at the GW no semicore +XC level at $\sim -3.3\ \mathrm{eV}$, and the fourth and the fifth low-lying conduction DOS peaks at the LDA level merge into one peak at the GW no semicore +XC level at $\sim -0.5\ \mathrm{eV}$. Moreover, the first two low-lying conduction DOS peaks at the LDA level and the lowest-lying conduction DOS peak at the GW no semicore +XC level all have non-negligible contributions from the Au 5d and 6s states. Major

differences in the shapes exist between the rest of the valence DOS spectrum at the LDA level and that at the GW no semicore +XC level.

From the DOS spectra for Au_{20} and Au_{32}, we see that DFT-LDA can give some useful information about the shapes of the lowest and the highest energy parts of the valence quasiparticle spectra, but not those of the parts with energies in between, where for both clusters the GW calculations are needed. In addition, some information about the shapes of the low-energy parts of the conduction quasiparticle spectra can be obtained from DFT-LDA. However, for both clusters, DFT-LDA is not good in predicting the absolute peak positions. In this sense, GW calculations are needed for good descriptions of the quasiparticle spectra of Au_{20} and Au_{32}.

Conclusions and Outlook

In this work, we used the GW method to study the electronic properties of small neutral gold clusters $\mathrm{Au_N}$ ($\mathrm{N} = 1 - 8$), and two larger neutral gold clusters, the tetrahedral $\mathrm{Au_{20}}$ cluster and the cagelike $\mathrm{Au_{32}}$ cluster. At the DFT-LDA level, all the very low energy structures we considered for small neutral gold clusters were found to be planar, while the $\mathrm{Au_{20}}$ and $\mathrm{Au_{32}}$ clusters under investigation both have quasi two-dimensional structures.

For the GW calculations of gold clusters, we found that the explicit inclusion of the Au semicore 5s and 5p states in the valence manifold is essential to achieve a satisfactory accuracy in the calculated quasiparticle spectrum. Based on this observation, we used a simplified approach to account for the effects of the Au semicore 5s and 5p states without including them fully in the GW calculations, and demonstrated that it works well for small neutral gold clusters. Since this simplified approach can reduce a lot the computational cost without compromising much the accuracy of the calculated quasiparticle spectrum, we used it to study two larger neutral gold clusters, the tetrahedral $\mathrm{Au_{20}}$ cluster and the cagelike $\mathrm{Au_{32}}$ cluster, which could not be tackled easily by using more traditional GW implementation, and predicted accurately the IPs and the EAs. We addressed the problem of molecular open-shells in GW calculations by devising a compromised scheme. This compromised GW scheme was shown to work well for two open-shell molecules, the neutral equilateral $\mathrm{Au_3}$ cluster and the neutral hexagonal $\mathrm{Au_7}$ cluster, also for the neutral linear $\mathrm{Au_3}$ cluster, for which the fractional occupancies in the almost degenerate HOMO and LUMO are not due to the structural symmetry, but result from the smearing technique used to converge the DFT calculation.

By comparing the calculated DFT-LDA DOS spectra with the corresponding GW ones, we found that DFT calculations can provide some useful information about the quasiparticle spectra of neutral gold clusters, especially concerning the shapes in the lowest-energy and highest-energy valence parts and the lowest-energy conduction part. However, they were found to be incapable of describing the absolute peak positions, for which GW calculations would be needed. For $\mathrm{Au_3}$, $\mathrm{Au_4}$ and $\mathrm{Au_7}$, we saw that although the calculated total energies are close between the different structures at the same cluster size, the calculated DOS spectra are quite different, indicating the strong dependence of the spectra on the geometry of the structure.

Future work can proceed in several possible directions. In the first place, since in our GW scheme

for open-shell molecules, the way of choosing integer occupancies for the degenerate HOMOs is not unique[7], it is necessary to check how the different possibilities would influence the calculated quasiparticle energy levels. There is also the possibility to construct a new set of orthonormal orbitals in the subspace formed by the degenerate HOMOs, and choose to use integer occupancies in GW calculations for these new orbitals. It should be interesting to see how the results would be. Secondly, it is straightforward to study the quasiparticle spectra of three-dimensional neutral gold clusters. Inspection of the differences between the quasiparticle spectra of two-dimensional (including quasi two-dimensional) and three-dimensional clusters can help us understand better the relation between structure and electron dynamics. Thirdly, since photoemission spectra are available for a wide size range of charged gold clusters, it would be valuable to investigate the quasiparticle spectra of charged gold clusters, so as to make direct comparisons between theory and experiment. There should be no essential difficulties to do so, but one needs to pay particular attention to the spurious Coulomb interactions between the supercell and its images due to the non-zero net charge, which can influence largely the calculated DFT energy levels and orbitals, thus also the calculated GW quasiparticle energies. This problem can be dealt with by using the Martyna-Tuckerman approach [114], which was also used in our $\Delta\mathrm{SCF}$ calculations of gold clusters. Finally, since the optical excitation energies of a neutral molecule can in principle be obtained from the difference between different conduction quasiparticle energies of the same molecule in a positively charged state, or the difference between different valence quasiparticle energies of the same molecule in a negatively charged state, it is important to gain insight into whether the optical excitation energies can be obtained accurately from GW calculations. A lot of effort may be needed in this direction, and it is possible that the level of self-consistency and the vertex corrections have to be considered for GW calculations.

[7] Two ways in the case of the equilateral Au_3 cluster or the hexagonal Au_7 cluster that we considered in this work, since one can choose to occupy either of the two degenerate HOMOs in the GW calculation.

Appendix A

Electronic Densities of States for Small Gold Clusters $\mathrm{Au_N}$ ($\mathrm{N} = 1 - 8$)

In Figs. [A.1]-[A.23], we display the electronic density of states calculated at different levels of theory for small neutral gold clusters $\mathrm{Au_N}$ ($\mathrm{N} = 1 - 8$). The corresponding projected density of states from the Au 5d, 6s or 6p states is also plotted.

For each structure, the GW semicore DOS spectrum is the best theoretical quasiparticle spectrum that we have. Since the LDA and GW no semicore DOS spectra are always quite different from the corresponding GW semicore one, particularly concerning the peak positions, it can be concluded that DFT-LDA and GW no semicore calculations can not provide good descriptions of the quasiparticle spectra of neutral gold clusters. In contrast, the GW semicore DOS spectrum is well reproduced by our simplified scheme to account for the effects of the Au semicore 5s and 5p states. By using our simplified scheme, with a sole exchange correction to the self-energy on top of the GW no semicore results, there is a large improvement in the shapes and positions of the DOS peaks. With also the addition of a correlation correction, the agreement with the GW semicore DOS spectrum is even better. Such good agreement is found for each considered structure, and is found not only in non spin-polarized calculations, but also in spin-polarized ones for each of the two spin channels, thus demonstrating the correctness of this scheme. Our simplified scheme also works well in conjunction with our scheme for the treatment of molecular open-shells. Moreover, the GW no semicore +X, GW no semicore +XC and GW semicore calculations open the quasiparticle gap that is severely underestimated at the LDA level. Note that with our simplified scheme, while the accuracy of the calculated spectra is not compromised much, the computational cost compared with the GW semicore calculations is significantly reduced.

From spin-polarized calculations of odd-numbered clusters, at a same level of theory, similarities in the shapes and positions of the DOS peaks can always be found for the two different spin channels. From the PDOS spectra, it can be seen that at any theoretical level the Au 5d states always contribute

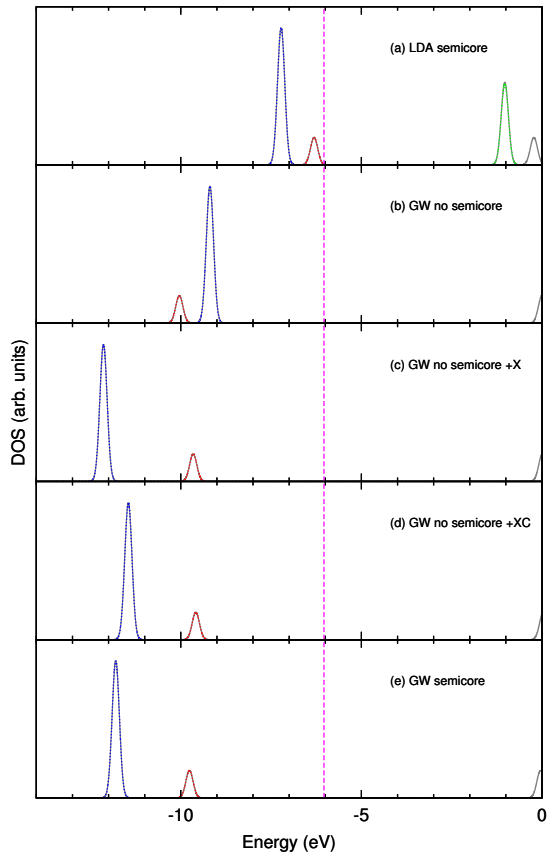

Figure A.1: Electronic densities of states for the majority spin channel of the Au atom, calculated from: (a) DFT-LDA with Au semicore states in valence, (b) GW without Au semicore states in valence, (c) GW without Au semicore states in valence and with the exchange correction to the self-energy, (d) GW without Au semicore states in valence and with both the exchange and the correlation corrections to the self-energy, (e) GW with Au semicore states in valence. In each subfigure, the projected density of states from the Au 5d (blue), 6s (red) or 6p (green) states is plotted together with the total density of states (gray). The dashed magenta line represents the Fermi level for the LDA semicore calculation. A Gaussian broadening of 0.1 eV has been used.

a lot to the valence part of the DOS spectrum, but very little or almost nothing to the conduction part. As a consequence, the valence part of the GW DOS spectrum depends sensitively on the Au semicore 5s and 5p states, while the conduction part does not. Strong s-d hybridization is found for all the considered structures of Au_N ($N = 2 - 8$), and comes from the strong relativistic effects in gold which have been assumed to have large contributions to the tendency of small gold clusters to favor planar structures [37, 38].

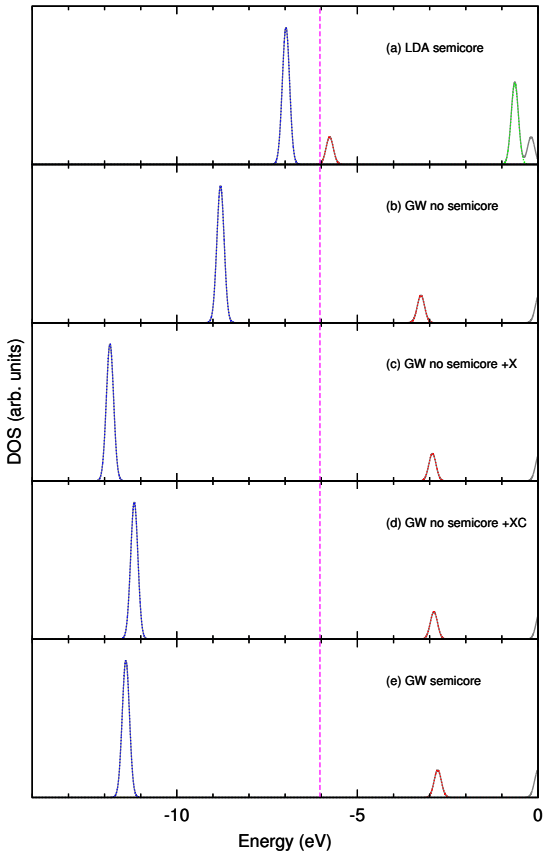

Figure A.2: Electronic densities of states for the minority spin channel of the Au atom. The different lines in this figure have the same meaning as those in Fig. [A.1].

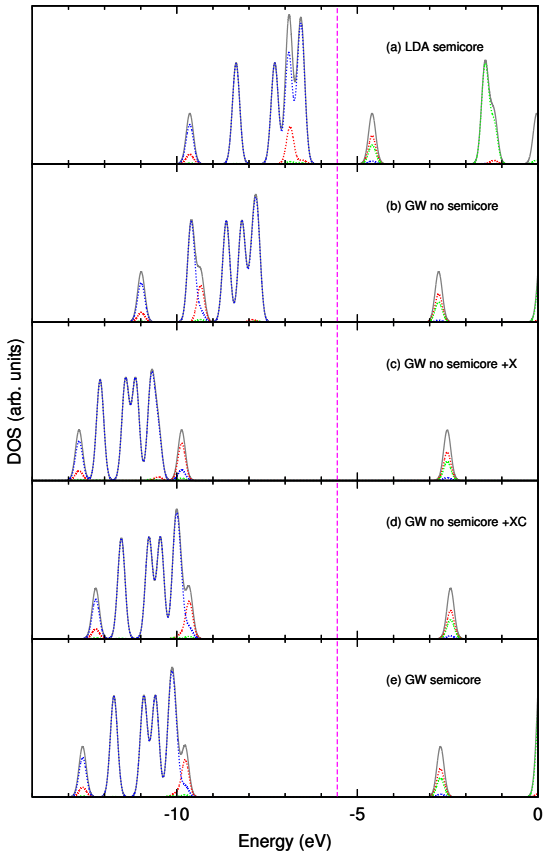

Figure A.3: Electronic densities of states for Au_2. The different lines in this figure have the same meaning as those in Fig. [A.1].

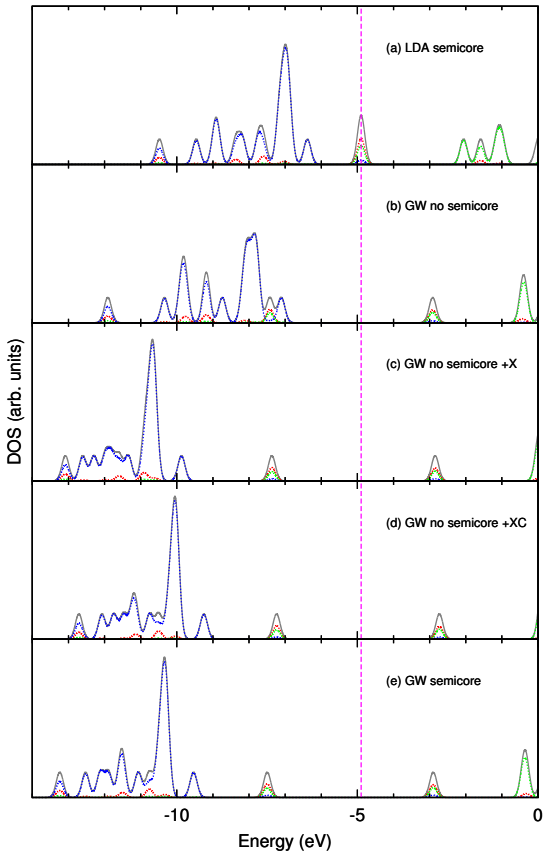

Figure A.4: Electronic densities of states for the majority spin channel of the 3a structure of Au_3. The different lines in this figure have the same meaning as those in Fig. [A.1].

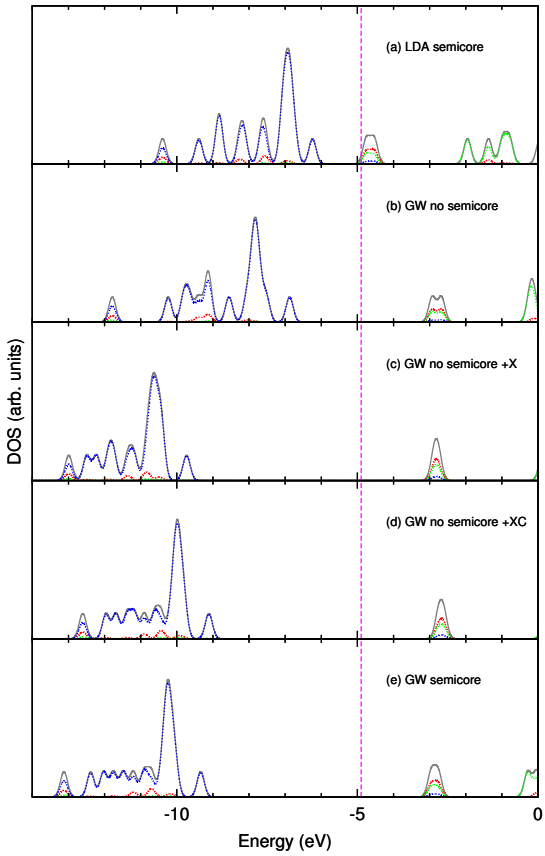

Figure A.5: Electronic densities of states for the minority spin channel of the 3a structure of Au_3. The different lines in this figure have the same meaning as those in Fig. [A.1].

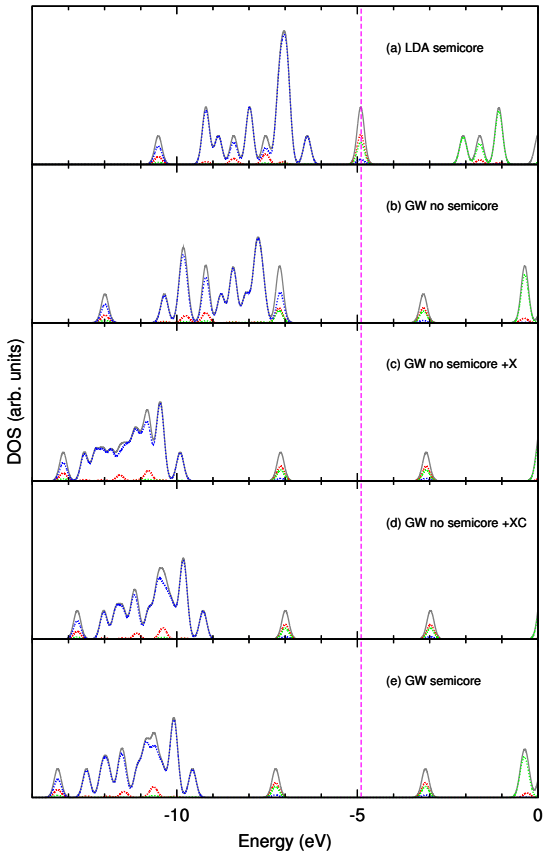

Figure A.6: Electronic densities of states for the majority spin channel of the 3b structure of Au_3. The different lines in this figure have the same meaning as those in Fig. [A.1].

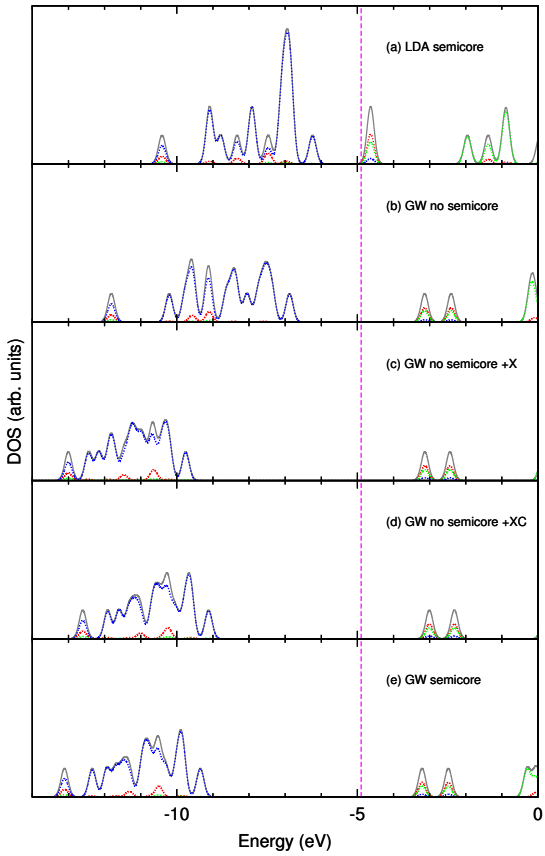

Figure A.7: Electronic densities of states for the minority spin channel of the 3b structure of Au_3. The different lines in this figure have the same meaning as those in Fig. [A.1].

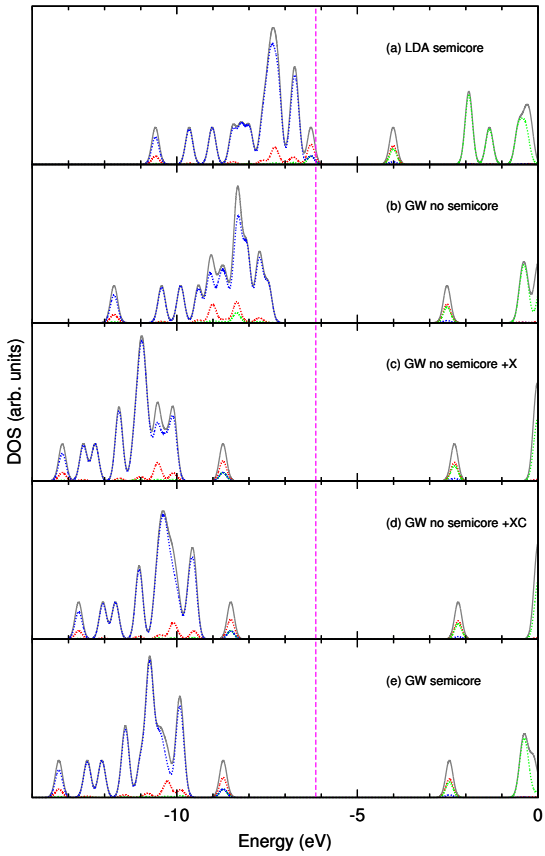

Figure A.8: Electronic densities of states for the majority spin channel of the 3c structure of Au_3. The different lines in this figure have the same meaning as those in Fig. [A.1].

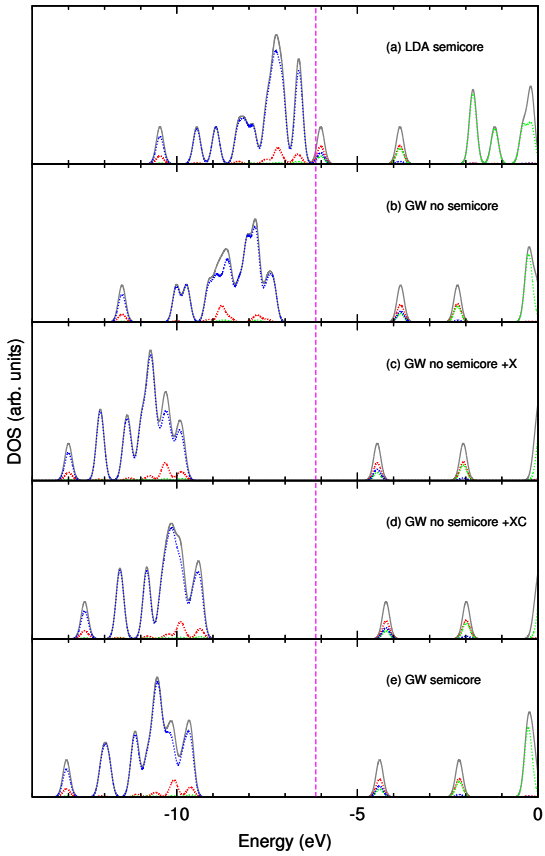

Figure A.9: Electronic densities of states for the minority spin channel of the 3c structure of Au_3. The different lines in this figure have the same meaning as those in Fig. [A.1].

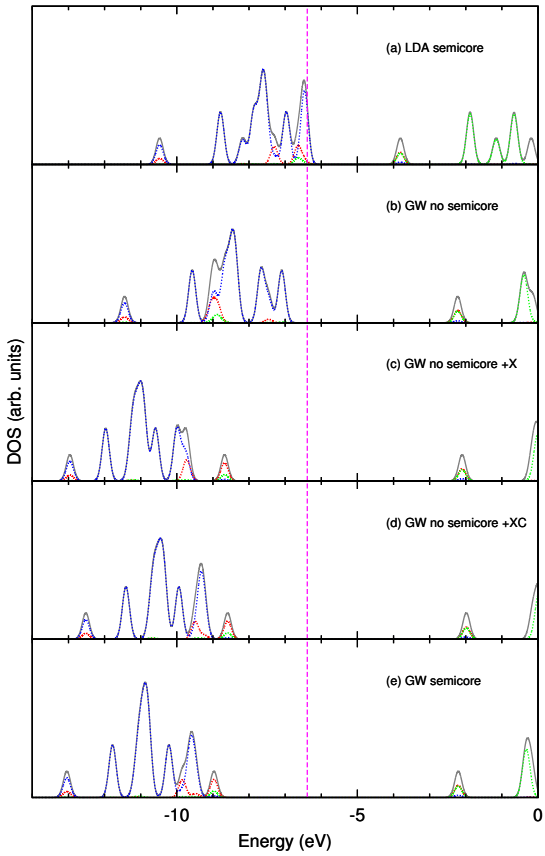

Figure A.10: Electronic densities of states for the majority spin channel of the 3d structure of Au_3. The different lines in this figure have the same meaning as those in Fig. [A.1].

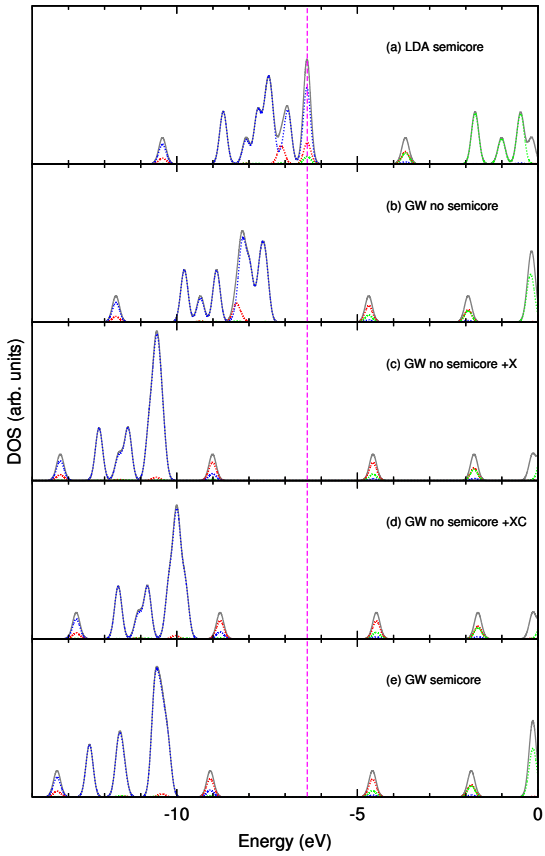

Figure A.11: Electronic densities of states for the minority spin channel of the 3d structure of Au_3. The different lines in this figure have the same meaning as those in Fig. [A.1].

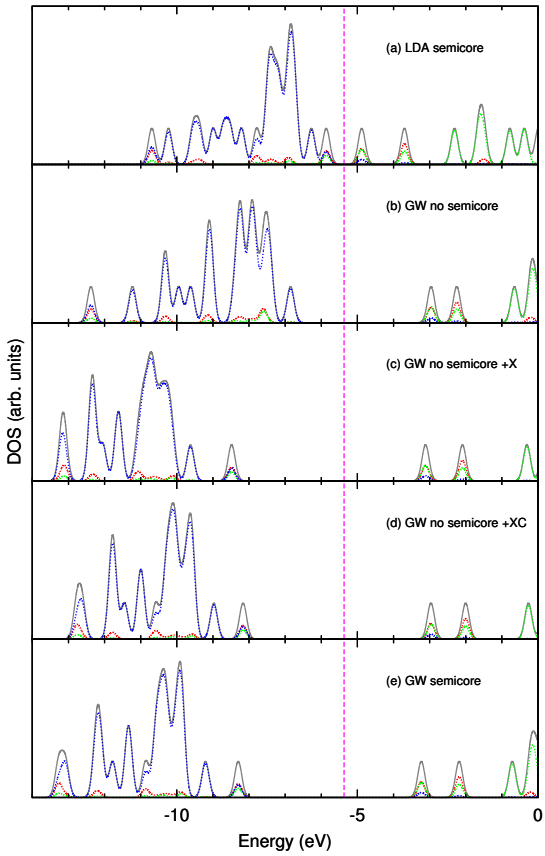

Figure A.12: Electronic densities of states for the 4a structure of Au_4. The different lines in this figure have the same meaning as those in Fig. [A.1].

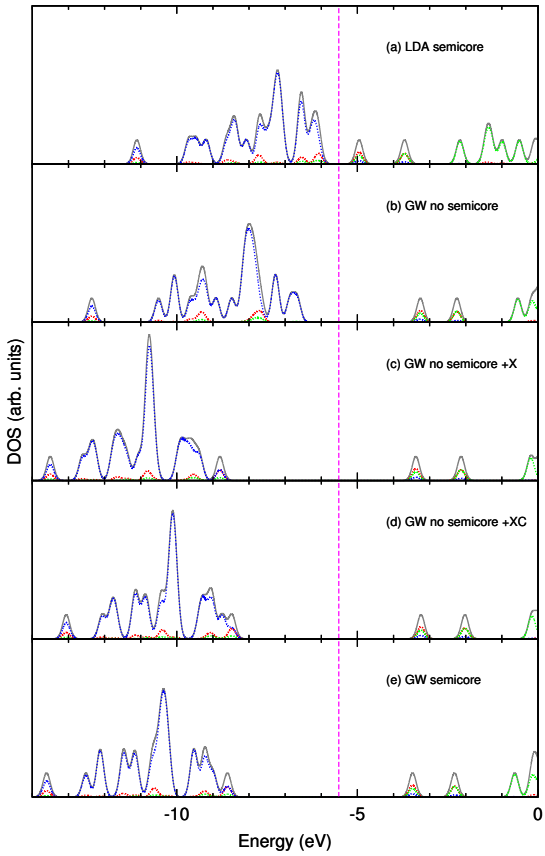

Figure A.13: Electronic densities of states for the 4b structure of Au_4. The different lines in this figure have the same meaning as those in Fig. [A.1].

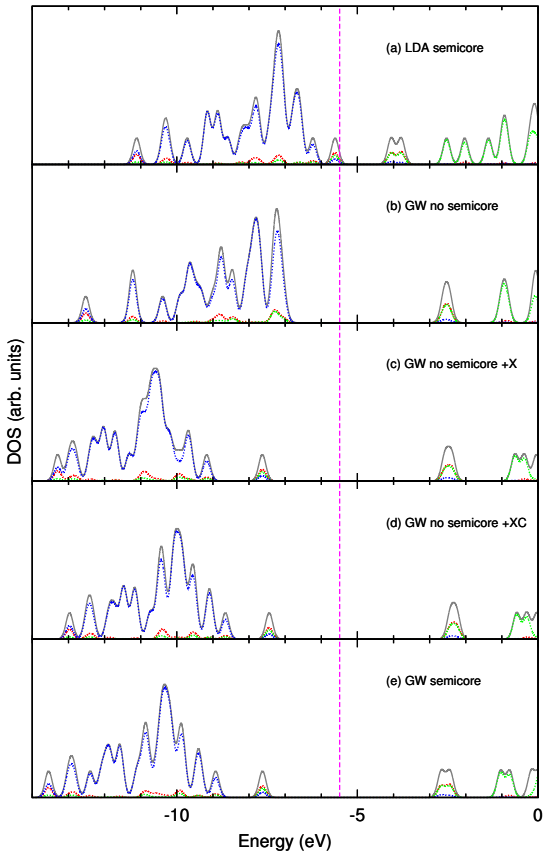

Figure A.14: Electronic densities of states for the majority spin channel of Au_5. The different lines in this figure have the same meaning as those in Fig. [A.1].

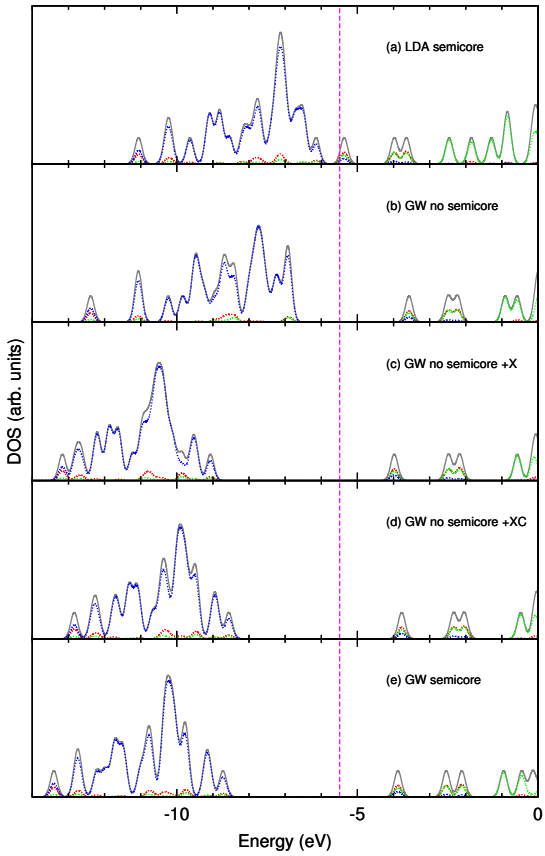

Figure A.15: Electronic densities of states for the minority spin channel of Au_5. The different lines in this figure have the same meaning as those in Fig. [A.1].

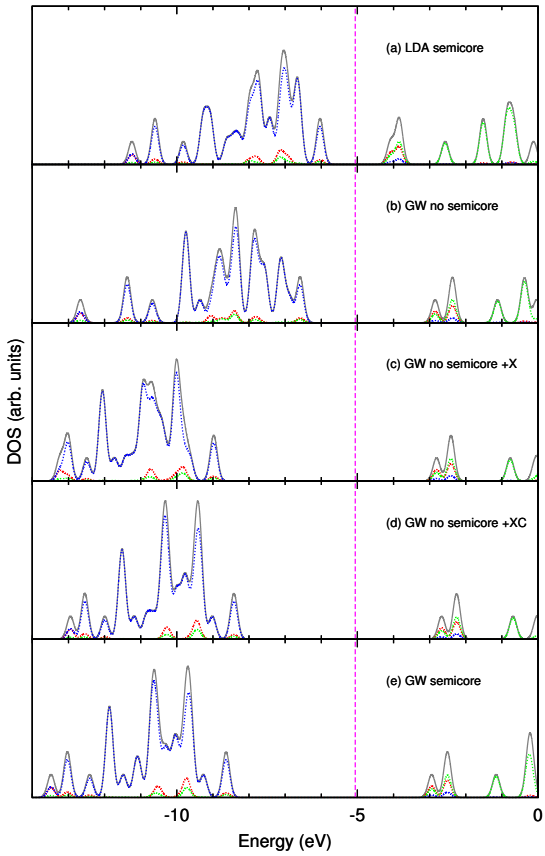

Figure A.16: Electronic densities of states for Au_6. The different lines in this figure have the same meaning as those in Fig. [A.1].

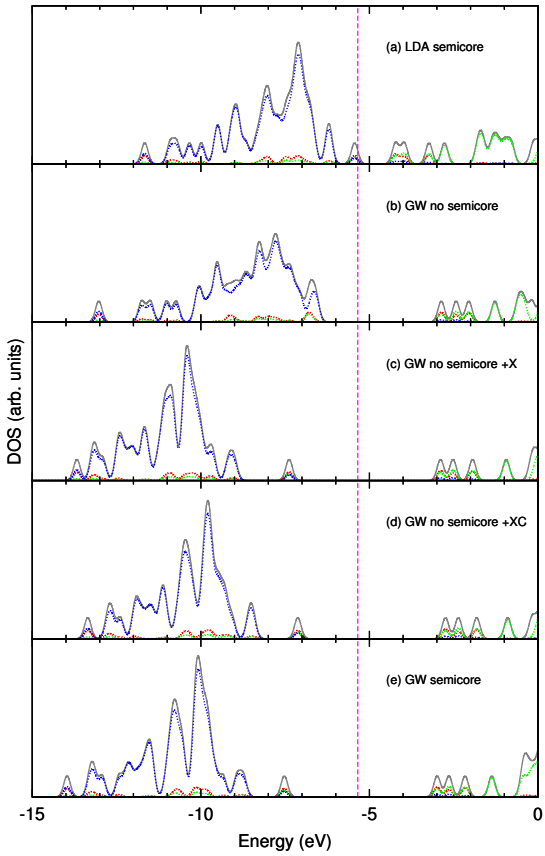

Figure A.17: Electronic densities of states for the majority spin channel of the 7a structure of Au_7. The different lines in this figure have the same meaning as those in Fig. [A.1].

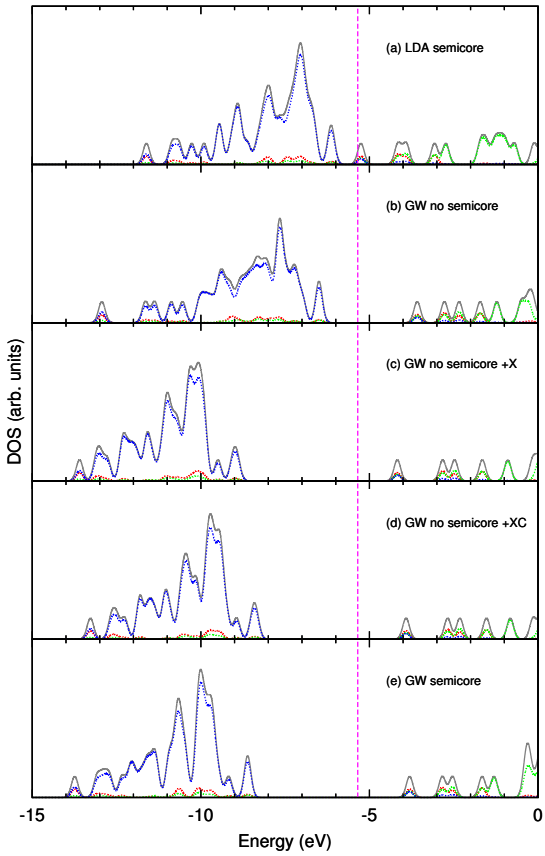

Figure A.18: Electronic densities of states for the minority spin channel of the 7a structure of Au_7. The different lines in this figure have the same meaning as those in Fig. [A.1].

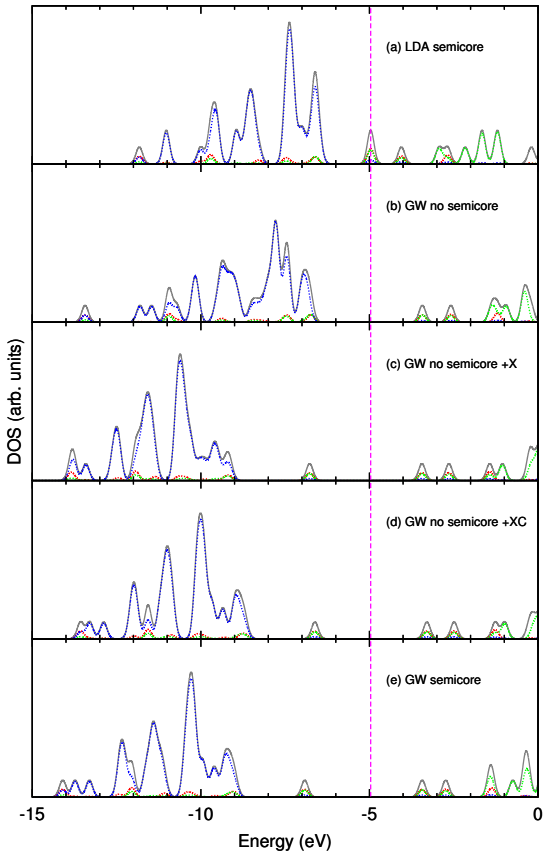

Figure A.19: Electronic densities of states for the majority spin channel of the 7b structure of Au_7. The different lines in this figure have the same meaning as those in Fig. [A.1].

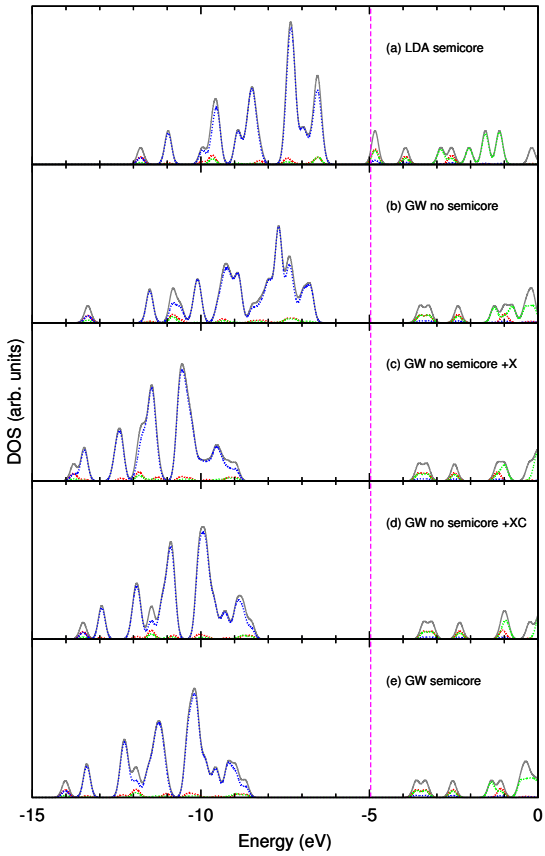

Figure A.20: Electronic densities of states for the minority spin channel of the 7b structure of Au_7. The different lines in this figure have the same meaning as those in Fig. [A.1].

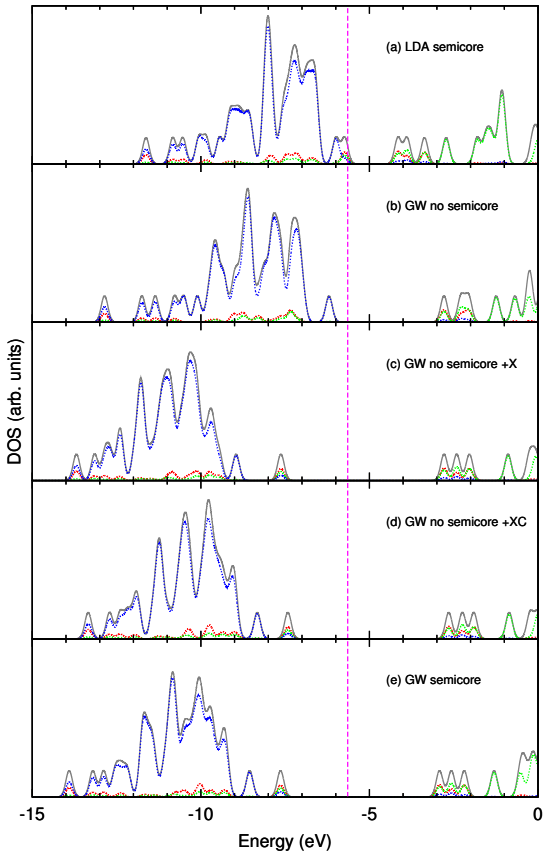

Figure A.21: Electronic densities of states for the majority spin channel of the 7c structure of Au_7. The different lines in this figure have the same meaning as those in Fig. [A.1].

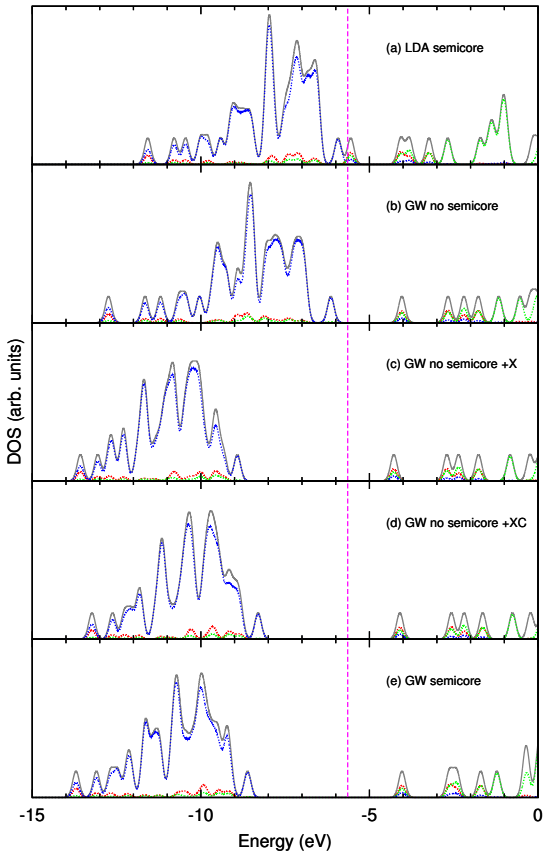

Figure A.22: Electronic densities of states for the minority spin channel of the 7c structure of Au_7. The different lines in this figure have the same meaning as those in Fig. [A.1].

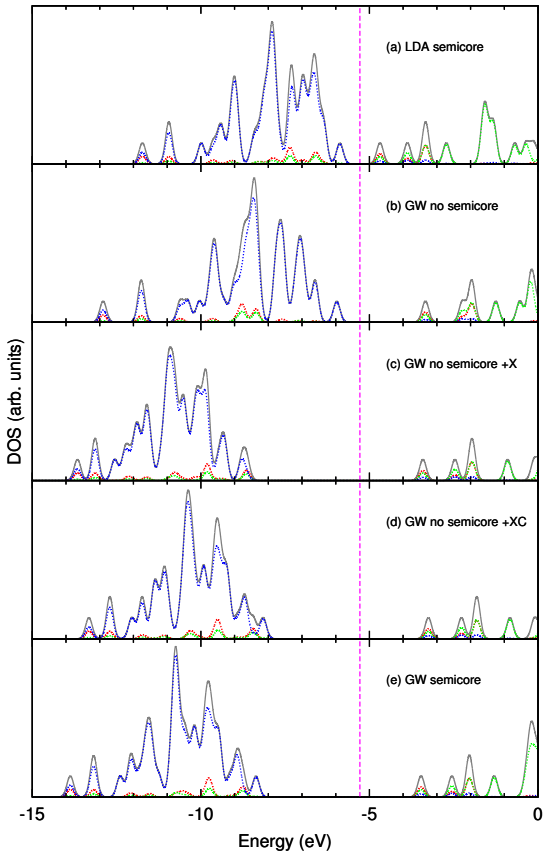

Figure A.23: Electronic densities of states for Au_8. The different lines in this figure have the same meaning as those in Fig. [A.1].

Bibliography

[1] M. C. Gimeno, in *Modern Supramolecular Gold Chemistry: Gold-Metal Interactions and Applications*, edited by A. Laguna (Wiley-VCH Verlag GmbH & Co. KGaA, Weinheim, 2009), pp. 1–63.

[2] M. A. Hayat, ed., *Colloidal Gold: Principles, Methods, and Applications* (Academic Press, New York, 1989).

[3] T. Ellis, Gold Bull. **37**, 66 (2004).

[4] B. Hammer and J. K. Norskov, Nature **376**, 238 (1995).

[5] M. Haruta, T. Kobayashi, H. Sano, and N. Yamada, Chem. Lett. **16**, 405 (1987).

[6] C. L. Cleveland, U. Landman, T. G. Schaaff, M. N. Shafigullin, P. W. Stephens, and R. L. Whetten, Phys. Rev. Lett. **79**, 1873 (1997).

[7] Y. Kondo and K. Takayanagi, Science **289**, 606 (2000).

[8] H. B. Weber, J. Reichert, F. Weigend, R. Ochs, D. Beckmann, M. Mayor, R. Ahlrichs, and H. v. Löhneysen, Chem. Phys. **281**, 113 (2002).

[9] P. Schwerdtfeger, Angew. Chem. Int. Ed. **42**, 1892 (2003).

[10] M.-C. Daniel and D. Astruc, Chem. Rev. **104**, 293 (2004).

[11] A. S. K. Hashmi and G. J. Hutchings, Angew. Chem. Int. Ed. **45**, 7896 (2006).

[12] T. Ishida and M. Haruta, Angew. Chem. Int. Ed. **46**, 7154 (2007).

[13] M. Walter, J. Akola, O. Lopez-Acevedo, P. D. Jadzinsky, G. Calero, C. J. Ackerson, R. L. Whetten, H. Grönbeck, and H. Häkkinen, Proc. Natl. Acad. Sci. USA **105**, 9157 (2008).

[14] R. Sardar, A. M. Funston, P. Mulvaney, and R. W. Murray, Langmuir **25**, 13840 (2009).

[15] M. Homberger and U. Simon, Phil. Trans. R. Soc. A **368**, 1405 (2010).

[16] D. Giljohann, D. Seferos, W. Daniel, M. Massich, P. Patel, and C. Mirkin, Angew. Chem. Int. Ed. **49**, 3280 (2010).

[17] W. Cai, T. Gao, H. Hong, and J. Sun, Nanotechnol. Sci. Appl. **1**, 17 (2010).

[18] W. A. de Heer, Rev. Mod. Phys. **65**, 611 (1993).

[19] C. Jackschath, I. Rabin, and W. Schulze, Ber. Bunsenges. Phys. Chem. **96**, 1200 (1992).

[20] C. Lemire, R. Meyer, S. Shaikhutdinov, and H.-J. Freund, Angew. Chem. Int. Ed. **43**, 118 (2004).

[21] S. Gilb, P. Weis, F. Furche, R. Ahlrichs, and M. M. Kappes, J. Chem. Phys. **116**, 4094 (2002).

[22] F. Furche, R. Ahlrichs, P. Weis, C. Jacob, S. Gilb, T. Bierweiler, and M. M. Kappes, J. Chem. Phys. **117**, 6982 (2002).

[23] P. Gruene, D. M. Rayner, B. Redlich, A. F. G. van der Meer, J. T. Lyon, G. Meijer, and A. Fielicke, Science **321**, 674 (2008).

[24] H. Häkkinen, B. Yoon, U. Landman, X. Li, H.-J. Zhai, and L.-S. Wang, J. Phys. Chem. A **107**, 6168 (2003).

[25] E. M. Fernández, J. M. Soler, I. L. Garzón, and L. C. Balbás, Phys. Rev. B **70**, 165403 (2004).

[26] A. V. Walker, J. Chem. Phys. **122**, 094310 (2005).

[27] W. Fa, C. Luo, and J. Dong, Phys. Rev. B **72**, 205428 (2005).

[28] L. Xiao, B. Tollberg, X. Hu, and L. Wang, J. Chem. Phys. **124**, 114309 (2006).

[29] X.-B. Li, H.-Y. Wang, X.-D. Yang, Z.-H. Zhu, and Y.-J. Tang, J. Chem. Phys. **126**, 084505 (2007).

[30] A. Deka and R. C. Deka, J. Mol. Struct. THEOCHEM **870**, 83 (2008).

[31] B. Assadollahzadeh and P. Schwerdtfeger, J. Chem. Phys. **131**, 064306 (2009).

[32] J. Li, X. Li, H.-J. Zhai, and L.-S. Wang, Science **299**, 864 (2003).

[33] M. P. Johansson, D. Sundholm, and J. Vaara, Angew. Chem. Int. Ed. **43**, 2678 (2004).

[34] X. Gu, M. Ji, S. H. Wei, and X. G. Gong, Phys. Rev. B **70**, 205401 (2004).

[35] S. Bulusu, X. Li, L.-S. Wang, and X. C. Zeng, Proc. Natl. Acad. Sci. USA **103**, 8326 (2006).

[36] B. Yoon, P. Koskinen, B. Huber, O. Kostko, B. von Issendorff, H. Häkkinen, M. Moseler, and U. Landman, ChemPhysChem **8**, 157 (2007).

[37] H. Häkkinen, M. Moseler, and U. Landman, Phys. Rev. Lett. **89**, 033401 (2002).

[38] P. Pyykkö, Angew. Chem. Int. Ed. **41**, 3573 (2002).

[39] P. Hohenberg and W. Kohn, Phys. Rev. **136**, B864 (1964).

[40] W. Kohn and L. J. Sham, Phys. Rev. **140**, A1133 (1965).

[41] L. Hedin and S. Lundqvist, Solid State Phys. **23**, 1 (1970).

[42] A. L. Fetter and J. D. Walecka, *Quantum Theory of Many-Particle Systems* (Dover, New York, 2003).

[43] G. D. Mahan, *Many-Particle Physics* (Plenum, New York, 2000).

[44] L. Hedin, Phys. Rev. **139**, A796 (1965).

[45] P. Giannozzi *et al.*, J. Phys.: Cond. Matt. **21**, 395502 (2009);
URL: `http://www.quantum-espresso.org`.

[46] URL : `http://gww.qe-forge.org`.

[47] P. Umari, G. Stenuit, and S. Baroni, Phys. Rev. B **79**, 201104 (2009).

[48] P. Umari, G. Stenuit, and S. Baroni, Phys. Rev. B **81**, 115104 (2010).

[49] P. Umari and S. Fabris, J. Chem. Phys. **136**, 174310 (2012).

[50] M. Born and R. Oppenheimer, Ann. Physik **389**, 457 (1927).

[51] M. Levy, Proc. Natl. Acad. Sci. USA **76**, 6062 (1979).

[52] E. H. Lieb, Int. J. Quantum Chem. **24**, 243 (1983).

[53] P. A. M. Dirac, Proc. Cambridge Phil. Roy. Soc. **26**, 376 (1930).

[54] D. M. Ceperley and B. J. Alder, Phys. Rev. Lett. **45**, 566 (1980).

[55] O. Gunnarsson and B. I. Lundqvist, Phys. Rev. B **13**, 4274 (1976).

[56] R. O. Jones and O. Gunnarsson, Rev. Mod. Phys. **61**, 689 (1989).

[57] J. P. Perdew and Y. Wang, Phys. Rev. B **45**, 13244 (1992).

[58] P. Ziesche, S. Kurth, and J. P. Perdew, Comput. Mater. Sci. **11**, 122 (1998).

[59] O. Gunnarsson, M. Jonson, and B. I. Lundqvist, Phys. Rev. B **20**, 3136 (1979).

[60] Y.-H. Kim, I.-H. Lee, S. Nagaraja, J.-P. Leburton, R. Q. Hood, and R. M. Martin, Phys. Rev. B **61**, 5202 (2000).

[61] J. D. Talman and W. F. Shadwick, Phys. Rev. A **14**, 36 (1976).

[62] A. Svane and O. Gunnarsson, Phys. Rev. B **37**, 9919 (1988).

[63] V. I. Anisimov, F. Aryasetiawan, and A. I. Lichtenstein, J. Phy.: Cond. Matt. **9**, 767 (1997).

[64] A. Görling, Phys. Rev. B **53**, 7024 (1996).

[65] A. Gorling and M. Levy, J. Chem. Phys. **106**, 2675 (1997).

[66] A. D. Becke, J. Chem. Phys. **98**, 5648 (1993).

[67] U. v. Barth and L. Hedin, J. Phys. C: Solid State Phys. **5**, 1629 (1972).

[68] G. B. Bachelet, D. R. Hamann, and M. Schlüter, Phys. Rev. B **26**, 4199 (1982).

[69] D. R. Hamann, M. Schlüter, and C. Chiang, Phys. Rev. Lett. **43**, 1494 (1979).

[70] L. Kleinman and D. M. Bylander, Phys. Rev. Lett. **48**, 1425 (1982).

[71] D. Vanderbilt, Phys. Rev. B **41**, 7892 (1990).

[72] K. Laasonen, A. Pasquarello, R. Car, C. Lee, and D. Vanderbilt, Phys. Rev. B **47**, 10142 (1993).

[73] G. Onida, L. Reining, and A. Rubio, Rev. Mod. Phys. **74**, 601 (2002).

[74] M. van Schilfgaarde, T. Kotani, and S. Faleev, Phys. Rev. Lett. **96**, 226402 (2006).

[75] M. Levy, J. P. Perdew, and V. Sahni, Phys. Rev. A **30**, 2745 (1984).

[76] F. Aryasetiawan and O. Gunnarsson, Rep. Prog. Phys. **61**, 237 (1998).

[77] W. G. Aulbur, L. Jönsson, and J. W. Wilkins, Solid State Phys. **54**, 1 (1999).

[78] L. A. Curtiss, P. C. Redfern, K. Raghavachari, and J. A. Pople, J. Chem. Phys. **109**, 42 (1998).

[79] J. Schwinger, Proc. Natl. Acad. Sci. USA **37**, 452 (1951).

[80] P. C. Martin and J. Schwinger, Phys. Rev. **115**, 1342 (1959).

[81] L. Hedin, J. Phys.: Cond. Matt. **11**, (1999).

[82] L. Hedin and B. I. Lundqvist, J. Phys. C: Solid State Phys. **4**, 2064 (1971).

[83] M. S. Hybertsen and S. G. Louie, Phys. Rev. Lett. **55**, 1418 (1985).

[84] P. Duffy, D. P. Chong, M. E. Casida, and D. R. Salahub, Phys. Rev. A **50**, 4707 (1994).

[85] X. Blase, C. Attaccalite, and V. Olevano, Phys. Rev. B **83**, 115103 (2011).

[86] C. Faber, C. Attaccalite, V. Olevano, E. Runge, and X. Blase, Phys. Rev. B **83**, 115123 (2011).

[87] C. Verdozzi, R. W. Godby, and S. Holloway, Phys. Rev. Lett. **74**, 2327 (1995).

[88] T. J. Pollehn, A. Schindlmayr, and R. W. Godby, J. Phys.: Cond. Matt. **10**, 1273 (1998).

[89] A. Schindlmayr and R. W. Godby, Phys. Rev. Lett. **80**, 1702 (1998).

[90] A. Schindlmayr, T. J. Pollehn, and R. W. Godby, Phys. Rev. B **58**, 12684 (1998).

[91] B. Holm and U. von Barth, Phys. Rev. B **57**, 2108 (1998).

[92] B. Holm and F. Aryasetiawan, Phys. Rev. B **62**, 4858 (2000).

[93] P. García-González and R. W. Godby, Phys. Rev. B **63**, 075112 (2001).

[94] F. Bechstedt, M. Fiedler, C. Kress, and R. Del Sole, Phys. Rev. B **49**, 7357 (1994).

[95] F. Aryasetiawan, L. Hedin, and K. Karlsson, Phys. Rev. Lett. **77**, 2268 (1996).

[96] B. Lundqvist, Phys. Kondens. Mater. **6**, 193 (1967).

[97] B. Lundqvist, Phys. Kondens. Mater. **6**, 206 (1967).

[98] M. S. Hybertsen and S. G. Louie, Phys. Rev. B **34**, 5390 (1986).

[99] H. N. Rojas, R. W. Godby, and R. J. Needs, Phys. Rev. Lett. **74**, 1827 (1995).

[100] M. M. Rieger, L. Steinbeck, I. D. White, H. N. Rojas, and R. W. Godby, Comput. Phys. Commun. **117**, 211 (1999).

[101] F. Giustino, M. L. Cohen, and S. G. Louie, Phys. Rev. B **81**, 115105 (2010).

[102] A. Fleszar and W. Hanke, Phys. Rev. B **56**, 10228 (1997).

[103] H. F. Wilson, F. m. ç. Gygi, and G. Galli, Phys. Rev. B **78**, 113303 (2008).

[104] F. Bruneval and X. Gonze, Phys. Rev. B **78**, 085125 (2008).

[105] J. A. Berger, L. Reining, and F. Sottile, Phys. Rev. B **82**, 041103 (2010).

[106] S. Baroni, R. Gebauer, O. B. Malcioğlu, Y. Saad, P. Umari, and J. Xian, J. Phys.: Cond. Matt. **22**, 074204 (2010).

[107] V. Feyer, O. Plekan, R. Richter, M. Coreno, and K. C. Prince, Chem. Phys. **358**, 33 (2009).

[108] Y. Saad, *Iterative Methods for Sparse Linear Systems* (Society for Industrial and Applied Mathematics, Philadelphia, 2003).

[109] M. Rohlfing, P. Krüger, and J. Pollmann, Phys. Rev. Lett. **75**, 3489 (1995).

[110] M. Rohlfing, P. Krüger, and J. Pollmann, Phys. Rev. B **57**, 6485 (1998).

[111] W. Luo, S. Ismail-Beigi, M. L. Cohen, and S. G. Louie, Phys. Rev. B **66**, 195215 (2002).

[112] T. Miyake, P. Zhang, M. L. Cohen, and S. G. Louie, Phys. Rev. B **74**, 245213 (2006).

[113] H. Dixit, R. Saniz, D. Lamoen, and B. Partoens, J. Phys.: Cond. Matt. **22**, 125505 (2010).

[114] G. J. Martyna and M. E. Tuckerman, J. Chem. Phys. **110**, 2810 (1999).

[115] H. A. Jahn and E. Teller, Proc. R. Soc. London, Ser. A **161**, 220 (1937).

[116] A. Khein, D. J. Singh, and C. J. Umrigar, Phys. Rev. B **51**, 4105 (1995).

[117] J. P. Perdew and A. Zunger, Phys. Rev. B **23**, 5048 (1981).

[118] A. M. Rappe, K. M. Rabe, E. Kaxiras, and J. D. Joannopoulos, Phys. Rev. B **41**, 1227 (1990).

[119] N. Troullier and J. L. Martins, Phys. Rev. B **43**, 1993 (1991).

[120] X. Wu, Z. Qin, H. Xie, R. Cong, X. Wu, Z. Tang, and H. Fan, J. Phys. Chem. A **114**, 12839 (2010).

[121] M. Ji, X. Gu, X. Li, X. Gong, J. Li, and L.-S. Wang, Angew. Chem. Int. Ed. **44**, 7119 (2005).

Acknowledgement

At this point, I would like to express my gratitude to all the people who have helped and supported me in innumerable ways during the past four years of my PhD study at SISSA. Foremost, I'm deeply indebted to my supervisors Prof. Stefano Baroni and Prof. Paolo Umari. Their professional guidance, wide knowledge, innovative ideas, great patience and continuous encouragement have been invaluable to me. Without them this work could not possibly be finished.

Special thanks to Prof. Andrea Dal Corso, for the important help with the generation of pseudopotentials, and also to Dr. Geoffrey Stenuit, for helping me in various aspects during the early time of this work. I'm also grateful to the help from Dr. Layla Martin-Samos.

Sincere thanks to the people who lectured me at SISSA, in particular Prof. Erio Tosatti, Prof. Sandro Sorella, Prof. Stefano de Gironcoli, Prof. Michele Fabrizio, Prof. Cristian Micheletti, Dr. Federico Becca and Dr. Alessandro Laio.

Many thanks to my friends and colleges Dr. Xiaoliang Hu, Dr. Changru Ma, Dr. Hongyi Xie, Dr. Tao Sun, Dr. Ngoc Linh Nguyen, Dr. Mauro Iazzi, Dr. Pierpaolo Baruselli, Dr. Xiaohua Zhang, Xiaochuan Ge, Ye Luo, and Wenjun Hu..., for all the interesting discussions with them, as well as the happy times we shared together.

I would like to thank all the people in SISSA, especially those in the Condensed Matter Theory Sector, for creating an excellent scientific environment.

I thank all my other friends at Trieste, for making my life here more colorful.

Last but not least, I would like to thank my family, for the endless support throughout my life, which makes me the person who I am today.